10-5-2017

Characterization of Powder Metallurgy Lightweight Alloys

Douglas B. Boudreau
University of Windsor

Recommended Citation

Boudreau, Douglas B., "Characterization of Powder Metallurgy Lightweight Alloys" (2017). *Electronic Theses and Dissertations*. 7239.
https://scholar.uwindsor.ca/etd/7239

Characterization of Powder Metallurgy Lightweight Alloys

By

Douglas B. Boudreau

A Thesis

Submitted to Faculty of Graduate Studies through the

Department of Mechanical, Automotive and Materials Engineering in

Partial Fulfillment of the Requirements for the

Degree of Master of Applied Science at the

University of Windsor

Windsor, Ontario, Canada

2017

Characterization of Powder Metallurgy Lightweight Alloys

By

Douglas B. Boudreau

APPROVED BY:

D. S. K. Ting
Department of Mechanical, Automotive and Materials Engineering

---

A. T. Alpas
Department of Mechanical, Automotive and Materials Engineering

---

A. Edrisy, Advisor
Department of Mechanical, Automotive and Materials Engineering

September 25, 2017

Declaration of Co-Authorship

I hereby declare that this thesis incorporates material, which is an outcome of a joint venture between Fiat Chrysler Automotive and the University of Windsor's department of mechanical, automotive and materials engineering, under the supervision of Dr. A. Edrisy. Fiat Chrysler Automotive provided technical knowledge in the research project. In all cases, the key ideas, primary contributions, experimental designs, data analysis, interpretation and writing were performed by the author.

I am aware of the University of Windsor Senate Policy on Authorship and I certify that I have properly acknowledged the contribution of the other researchers to my thesis, and have obtained written permission from each of the co-author(s) to include the above material(s) in my thesis.

I certify that, with the above qualification, this thesis, and the research to which it refers is the product of my own work.

I certify that, to the best of my knowledge, my thesis does not infringe upon anyone's copyright nor violate any proprietary rights and that any ideas, techniques, quotations, or any other material from the work of other people included in my thesis, published or otherwise, are fully acknowledged in accordance with the standard referencing practices. Furthermore, to the extent that I have included copyrighted material that surpasses the bounds of fair dealing within the meaning of the Canada Copyright Act, I certify that I have obtained a written permission from the copyright owner(s) to include such material(s) in my thesis.

I declare that this is a true copy of my thesis, including any final revisions, as approved by my thesis committee and the Graduate Studies office, and that this thesis has not been submitted for a higher degree to any other University or Institution.

Abstract

Over the past few decades, the automotive industry has seen a steady increase in the amount of powder metallurgy products that have been included in modern vehicles. The majority of the parts were cold press and sintered products that allowed for a high production volume and low cost option. In more recent years, the powder metallurgy parts have seen service as structural parts mainly consisting of steel base products. The mechanical and dynamic properties of four lightweight materials produced by powder metallurgy and additive manufactured are tested to determine if they are suitable to be used in a structural part within an internal combustion engine. The research concluded that an additive manufactured titanium material was the only tested material that met or exceeded the current requirements for strength to be a suitable material. The selected material showed low porosity that resulted in suitable fatigue and mechanical properties for a possible substation of the reference material.

Acknowledgements

First, I would like to thank my advisor Dr. A. Edrisy for her supervision throughout the entirety of this project and for her consistent guidance through this endeavor. Additionally, Dr. O.A Gali and Dr. K. Farokzhadeh. for assisting in the evaluation process of this research as well as beneficial feedback throughout the entirety of this endeavor. Ben Slattery from FCA for valuable technical insight regarding research materials.

I would also like to thank my committee members Dr. A. Alpas and Dr. D. Ting for being committed to attending my presentations and reviewing my thesis. Additionally, their beneficial input directly correlates to the caliber of work completed during my graduate studies.

Gratitude is also expressed Fiat Chrysler Automobiles and the employees for essential feedback as well as providing funding and materials required for the bulk of this research.

Table of Contents

List of Figures

List of Tables

Nomenclature

List of Abbreviations

AM	Additive manufacturing
ASM	American Society for Metals
ASTM	American Society for Testing Materials
EDM	Electronic Discharge Machining
EDS	Energy Dispersive X-ray Spectroscopy
FEG	Field Emission Gun
FIB	Focused Ion Beam
ICP-OES	Inductively Coupled Plasma Optical Emission Spectroscopy
MPIF	Metal Powder Industries Federation
PM	Powder Metallurgy
PTA	Plasma Transferred Arc
SAED	Selected Area Electron Diffraction
SEM	Scanning electron microscope
SFF	Solid Freeform Fabrication
TEM	Transmission Electron
XRD	X-ray diffraction

List of Symbols

$\mathrm{dA_s}$	Change in free surface area of a particle
$\mathrm{dA_b}$	Change in area of grain boundary
$\mathrm{\gamma_s}$	Surface area energy of a particle
$\mathrm{\gamma_b}$	Surface area energy of grain boundary
n	Coordination number of pores
n_c	Critical coordination number of pores
φ_e	Contact angle of adjacent pores
ρ	Density
$\frac{da}{dN}$	Crack propagation rate
ΔK	Cyclic stress intensity factor
λ	Wavelength
d_{hkl}	Interplanar spacing
a_o	Lattice parameter
P_w	Density of water
$\sigma_{A,50}$	Mean alternating stress
σ_{a0}	Minimum alternating stress
d	Fatigue test increment step
σ_a	Applied Stress at reduced section of a fatigue sample

Chapter 1: Introduction

1.1 Background and Motivation

The powder metallurgy (PM) industry has seen a steady rise in the adoption of PM products and applications within a number of industries, there are two principal reasons for using powder metallurgy products, cost savings compared to alternative processes and their unique characteristics highlighted in this report. Iron based structural components comprise the bulk of the mechanical parts that are produced by the powder metallurgy process, however, there is an increase in the production of other metals including low density materials such as aluminum, titanium, copper and bronze. When compared to traditional fabrication processes e.g., casting, the PM process has an advantage over the dimensional precision but the driving force behind using the PM route is cost savings. Upon the optimization of the PM process it is now possible to produce parts with equal or superior properties to those made from the traditional methods. The powder metallurgy route offers unique characteristics to manufactured parts including the ability to control the degree of porosity, the ability to alloy metals and composites that would be insoluble in liquid state, refractory materials with very high melting points, such as tungsten, molybdenum and niobium. Friction materials can be formed by dispersing non-metallic materials in a metallic matrix, wear resistant hard metals can be formed by the inclusion carbides or diamond grit. Refractory materials are very difficult to produce by traditional melting usually resulting in the material being brittle in the cast state[1]-[2].

1.2 Objectives

This research is conducted to find a possible replacement material based on lightweight powder metallurgy techniques to be used in an internal combustion engine part that undergoes a cyclical stress state.

1.3 Organization of Thesis

This thesis is organized into six chapters, including chapter one that introduces the background and motivation for the research as well as the scope of the thesis. Chapter two consists of the relevant literature that was studied to prepare a suitable experimental plan and to build an understanding of the findings from the experimental data. Chapter three contains the detailed experimental procedures that were followed during the research process. Chapter four comprises the experimental results from the research project. Chapter five provides a discussion on the findings of the research and chapter six summarizes the conclusions of the research as well as future recommendations.

Chapter 2: Literature Survey

2.1 Introduction

Lightweight material substitution has become common practice to lower the overall mass within the internal combustion engine. The following study looks at the physical properties of four proposed materials as potential substitutes for the current powder metallurgy steel component of an internal combustion engine. Four lightweight powder metallurgy materials were provided for material property testing, two aluminum alloys and two titanium alloys. A ferrous copper powder metallurgy steel was also provided for comparison as the reference material currently used in production. The aluminum alloys are proprietary blends provided by separate powder metallurgy manufactures both employing a press and sinter technique. The titanium samples were provided by a titanium powder producer using a press and sinter technique; the other titanium sample is manufactured using a plasma transferred arc solid free form fabrication method using a novel manufacturing method.

Analysis of the microstructure is done to characterize the grain structure and pore arrangement within the test materials. Products produced through powder metallurgy techniques that are limited to cold press and sinter process will form pores or vacant pockets within the product due to numerous causes, including but not limited to, powder lubricant burn-out, sinter neck formation and packing efficiency of the powder compact. Since a void is unable to carry a load or respond to stress, the structure and number of pores within powder metallurgy part has a defining influence on the mechanical and dynamic properties. Pores structures will act as an internal stress concentrator and an initiation point for crack growth. Porosity within the sample will also accelerate internal crack growth and lower the fracture toughness of material [1].

2.1.1 Powder Metallurgy Fundamentals

Powder metallurgy begins with the formation of powders, a collection of particles, of a certain element. Powder characterization is an important factor in the initial stages of the PM process. Powders are characterized by numerous attributes including but not limited to; particle size, distribution, agglomeration, surface area, packing factor and composition. The particle size is difficult to measure due to the variance in the shape of the particle and defining a standard to classify different powders by a comparative size is used. Particles can be spherical, flake, platelet, rod, and irregular shaped all having a different characteristic measurement. Equivalent spherical diameters are used as the characteristic measurement to classify particles size, techniques to measure these are the defined in ASTM B330 [3]. Once the characteristic measurement is found a statistical approach is then used to classify the powder typically based on a log-normal distribution of particle size, ensuring the measured sample is representative. Packing density affects the flow rate of the powder that determines the speed of production, compression pressure and die sizing for the operation [1].

Powder production methods are dependent on numerous factors; cost, reactions and desired characteristics. The techniques are based on mechanical milling, chemical reaction, electrolytic deposition, liquid atomization and vapor deposition. These methods depend on the desired powder as well as the initial composition all of the methods attempt to create a surface area within the powders to facilitate bonding of the compact. The powder is then mixed at desired elemental ratios for the resulting alloy, and a polymer based binder is added to aid in the flowability of the powder in the forming process. The formulated powder is compacted to bring the powder particles in close proximity to encourage bonding, the compacted mass of powders is referred to as a green compact. Pressure based densification where the powder is subjected to high pressures through compaction or a hybrid densification, where high pressure and temperature is employed to densify the powder. Sinter based densification is also used where the powder is shaped then subjected to high temperatures to promote bonding and formation of the matrix. In pressure based densification the green body is then subjected to sintering after compaction in a separate step [1]-[2].

The fabrication of PM based parts can be accomplished through the various process on both the powder preparation as well as the method used to solidify the powders. The compaction and sintering of the parts can be achieved through simultaneous actions or a series of steps as Wang et al. stated, the method of fabrication can have an impact on the properties of the part [6]. The compaction of powder can be done through die compaction where the die is filled with powder, and a tool is pressed into the die with a large force, this can be done through several dies and punches on the same part and is referred to as cold isostatic pressing. Another approach is to warm the die before pressing as German et al. has shown to promote densification as most materials soften at elevated temperatures. Hot isostatic pressing is a method to reach full densification of the part through the single step of compaction pressure and elevated temperature, this is typically used on non-complex parts. Powder injection molding is another method for forming a green body that employs the use of a low viscosity polymer binder to form a slurry with the powder and is then injected into a mold similar to the process of plastic injection molding, once the part is removed and sintered the polymer is typically burnt off, and the sintering promotes bonding [1], [4].

2.1.2 Solid State Sintering

Densification occurs when the mass transport is driven by the associated free energy of the individual powder particles leading to powder compact of coalesced particles. This process is classified as sintering, where the space between contact points of the particles is filled due to the difference in curvature of the void space. The sintering process will be halted when the following thermodynamic relation is satisfied

$$-\frac{dA_s}{dA_b} = \frac{\gamma_b}{\gamma_s} \tag{1}$$

here dA_s the change in free surface area of the particle is, dA_b is the change in area of the grain boundary, γ_b and γ_s are the energy associated with grain boundaries and particle surface area, respectively [5]. The pore structure of a compact can be modelled as a network of particles and irregular polyhedral in contact. The irregular polyhedral are models of pores within the structure and a coordination number is assigned that defines the number of particles that border the pore. As sintering is taking place the volume associated with the pores is decreasing and will reach an equilibrium size. Pores with a coordination number less than or equal to the critical coordination number n_c will disappear. The critical coordination number has a positive relation with $\frac{\gamma_b}{\gamma_s}$ and outlines the volume change linked to sintering, however, full densification cannot be achieved with sintering. Sintering is not the only dynamic process that is occurring during densification of the compact, grain coarsening is also taking place as mass transport is a beneficial mechanic for smaller grains to converge to a single larger grain until the change in energy is no longer advantageous. When smaller particles merge to form a larger particle, this has a negative effect on the coordination number and can restart or aid the sintering process.

Two complimentary regimes are present in the densification of powder compacts as stated above, sintering and grain coarsening, as sintering occurs the pore volume is decreasing allowing smaller grains to contact each other and merge to form a larger grain. The coarsening of the grain structure does not lead to any further volume reductions as the volume of the smaller grain decreases at the same rate the larger grains grow by assimilating them. This process can be visualized in Figure 1 by the reduction of contact angles by the sintering; the contact angle is related to the relative energies by the following relationship.

$$2\cos\varphi_e/2 = \frac{\gamma_b}{\gamma_s} \tag{2}$$

In Figure 1c as the sintering process or coarsening allows the particles to contact with a smaller contact angle than that of equilibrium, the coarsening mechanic forms a new metastable configuration of Figure 1d.

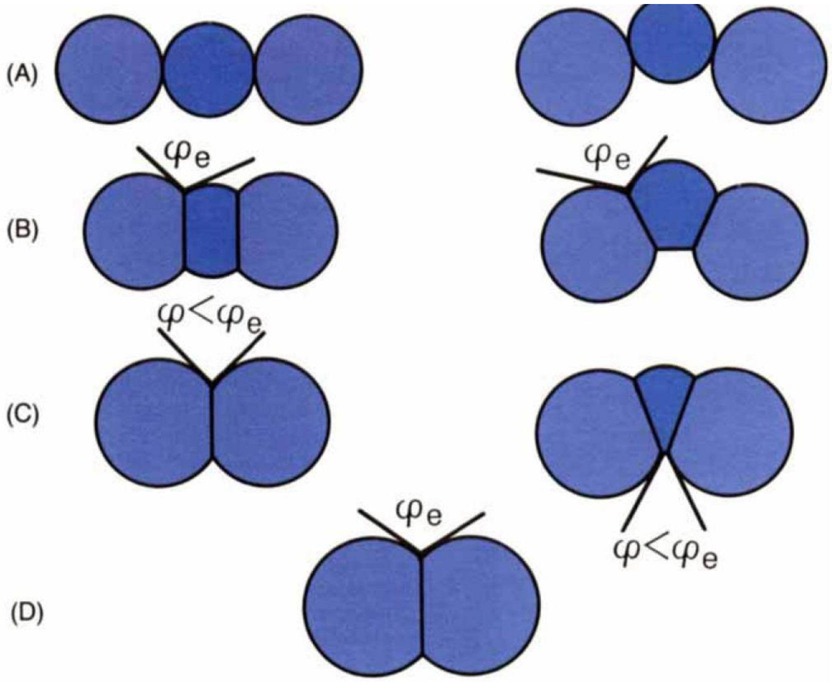

Figure 1 Grain growth kinetics showed along two separate routes (left) sintering (right) coarsening [5].

Sintering conducted under pressure also leads to a volume reduction allowing for new particle contacts without the aid of coarsening. With the coordination number being of high importance to densification it would be beneficial to produce a powder compact with all pores having an ordered structure leading $n \leq n_c$. Testing done on such a system has led to crack like voids appearing after heat treatments and some investigators are looking into powder compact systems with a high packing density and disordered arrangement minimizing the volume of pores that do not disappear. As the quality of powders is increased the ability to achieve the desired distributions can be achieved and the powder compacts can limit the amount of pores formed that have an $n > n_c$ [5]–[7].

2.1.3 Liquid Phase Sintering

Sintering is also aided by an additive phase in powder form with the primary powder that has a lower melting point than the major components. During the sintering process, the secondary phase will become liquid and encapsulate the powder particles and will redistribute itself within the voids and gaps of the particles while wetting the surfaces. The driving force behind the liquid phase rearrangement is capillary action that lead to an appreciable amount of shrinkage compared to the green compact. The liquid phase and solid phase interactions depend on the specific system and are generally a combination of solid solubility and diffusivity of the components. As the process continues matter can be transported from surfaces of smaller particles that have high chemical potential to the lower chemical potential surfaces of the larger particles by diffusion through the liquid phase and densifying the structure. The process is modelled in terms of a shrinkage vs time schematic in Figure 2, showing a rapid degree of shrinkage in the initial stage of liquidation of the secondary phase.

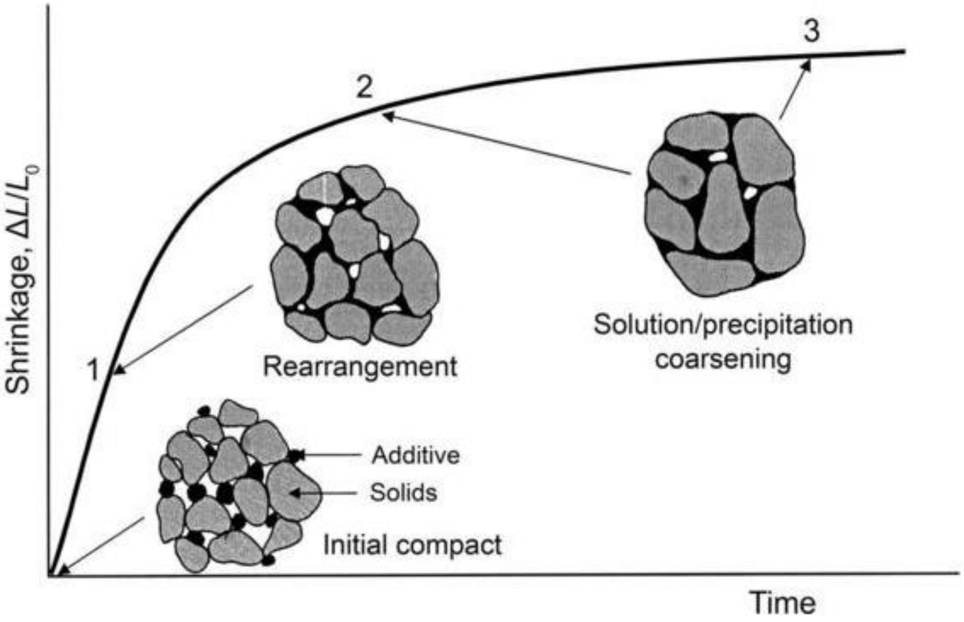

Figure 2 Densification schematic of liquid phase sintering process [8]

The structure of liquid phase sintered materials differs from that of solid phase sintered materials by the presence of a two-phase structure and distinctively rounded and smooth grain structures. The solid state sintered materials has a more natural structure dependant upon the characterization of the initial powders, in low volume fraction liquid phase sintered systems the morphology of the grains structure does not attain a smooth structure [8]–[10].

2.1.2 Characterization Techniques for Evaluation of Powder Metallurgy Components

Characterizing the powder metallurgy part consists of testing and classification of numerous properties of the powder metallurgy produced the part, these test and results are typically the same encountered elsewhere in materials engineering. There are several properties that are of interest based, however based on the proposed purpose of the manufactured the research will be limited to those properties. Microstructural features determine many of the properties of interest, grain size, pore size, distribution of both pores and grains within the compact. A sample of the sintered compact is polished and etched to reveal microstructure features under optical microscopy as well as electron microscopy. The polishing and etching of a porous compact provides significant challenges as the surface preparation can affect the microstructure, with high degree of porosity can be significant. Measurements of grain size and pore size, as well as phases present within the sample and can provide information about properties of the sample, a large degree of porosity can lead to low hardness measurements as the applied energy is used to decrease the volume. Grain size and grain orientation can control the propagation of cracks and fissures within the structure [1]-[2], [11].

A key factor in PM parts is the porosity of the product, achieving the desired density or inversely the porosity is the focus in determining the production process and powder characteristics. Porosity can be determined through a variety of methods such as Archimedes principle, ultrasonic wave velocity as well as electron microscopy image analysis. The density of a PM part is often denoted as apparent density due to the inability to accurately measure the density without a certain amount of uncertainty in any method. If the pore structure shows interconnectivity between the interior pores and the exterior of the sample, the liquid used will penetrate the sample and distort the actual value, if the structure is closed then trapped gasses could provide buoyancy of the sample. Image analysis is typically done on a two-dimensional representation of the microstructure and at a representative plane, therefore the pore images can be skewed depending on the orientation. The accepted method is outlined in the standard MPIF 42 for apparent density and MPIF 57 defines the testing for porosity [11]. Hardness is measured on the same scales as conventional materials using the Rockwell or Vickers scale depending on the testing apparatus. The hardness of PM products is typically referred to as apparent hardness due to the influence of porosity on the test results, a high degree of porosity could lead to a lower hardness value due to the energy dissipation in collapsing pores, MPIF 43 is the standard for hardness testing of powder metallurgy samples [1]-[2], [11].

Tensile and compressive strengths are evaluated in a similar fashion as conventional material with standards outlining the procedures according to the Metal Powders Industries Federation, MPIF 10 and MPIF 61, respectively. It is not uncommon to experience higher compressive strengths than tensile in porous materials due to the fracture mechanics of voids present in the sample that do not hinder the compression strengths. Dynamic testing of PM materials is also similar to conventional materials, fatigue testing using a rotating beam fatigue test machine is typical within the industry and is outlined MPIF standard 56. As Grayson et al. determined the porosity of the samples have a detrimental effect on the fatigue strength of the material where a decrease of 50% from conventional material was not uncommon in the test results. Due to crack propagation under dynamic loading powder metallurgy parts with a high degree of porosity are highly susceptible to fatigue failure [1], [11]-[12]

2.1.4 Powder Metallurgy of Steel Alloys

The state of the art with regards to lightweight materials produced through powder metallurgy and particulate manufacturing are presented in the following sections with an emphasis on titanium and aluminum alloys. With the purpose of determining relative strength and characteristics of lightweight, low-density materials a suitable benchmark will be used to compare the materials. A PM produced component consisting of FC-0205 iron based alloy will be used as the material standard for this application. Maruci et al. investigated the effects of sinter-hardening steel alloys of different densities [13]. Their findings are presented in Figure 3 shows a decrease in strength with a decreasing in density.

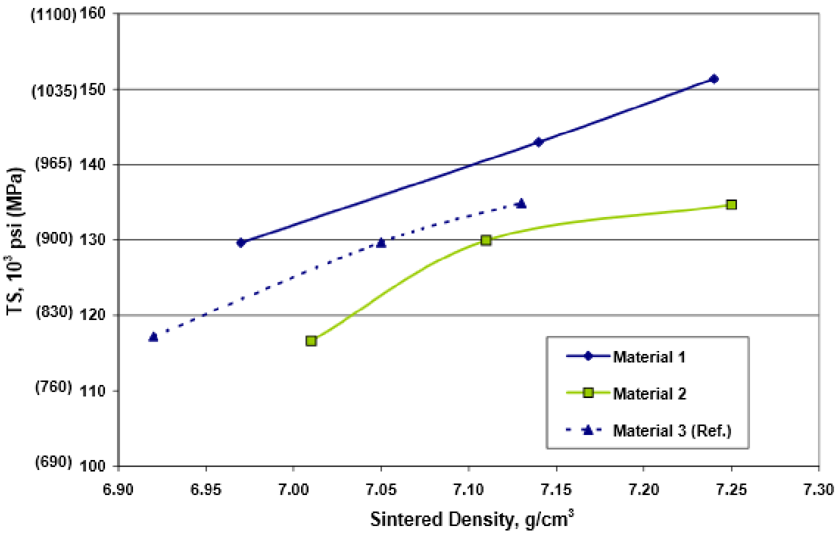

Figure 3: Tensile strength of sintered-hardened steel alloys [14]

The material specification for this material is based on the MPIF 35 standard denoting that it is a ferrous steel with copper as the main alloying element, the numerical values indicate a nominal combined carbon percentage of 0.5% and 1.75% Copper [12]. Iron-copper-carbon materials such as the FC-0205 are used extensively in the powder metallurgy industry in North America. The reason for the widespread adoption of this material as indicated by Murphy et al. is the beneficial properties due to liquid phase sintering process. The increase in sintering of the matrix iron from the liquid phase melting of the copper in sub-optimal conditions improved the properties of this alloy, the carbon diffuses and forms pearlite, and the copper strengthens the ferrite matrix. The effect of the change in sintering times on the density, chemical composition and distribution of the alloying elements as well as the microstructure have been investigated for this particular iron-copper PM alloy by Murphy et al [15]. As can be noted that there are numerous contributing factors that effect the strength and behavior of the sintered alloys [12], [14], [16].

2.1.5 Powder Metallurgy of Titanium Alloys and Composites

The use of titanium alloys in powder metallurgy has been steadily increasing due to the viability and cost reduction of producing near net shape parts with limited post processing; this has led them to be a focus of worldwide research and development. The mechanical properties of titanium Ti-6Al-4V as with other PM alloys depends on the porosity, microstructure and oxygen content within the post sintered and pre-sintered alloy, the oxygen content is specific to titanium. The mechanical properties of Titanium (Ti) are evaluated from two standpoints, dynamic properties and static properties the static properties of titanium. The collected data shows an improving trend toward minimizing the difference in ductility between wrought Ti and PM Ti. It was also found that the effect of porosity has a greater impact on the decrease in dynamic properties of PM titanium, the fatigue strength of PM titanium was comparable to that of ingot manufactured titanium only when a fully densified PM titanium was tested due to the dependency of surface voids on the fatigue strength [14]-[16] .

Liu et al. investigated the effects of alloying elements, thermo-mechanical treatment and particulate reinforcement on the microstructure and mechanical properties of PM titanium alloys. Their findings indicated that particulate reinforcement should contribute to promote bonding during sintering, improvements in mechanical properties or both. They also concluded that alloying elements that enhanced secondary bonding during sintering led to an increase in ductility of the PM Ti alloy [18].

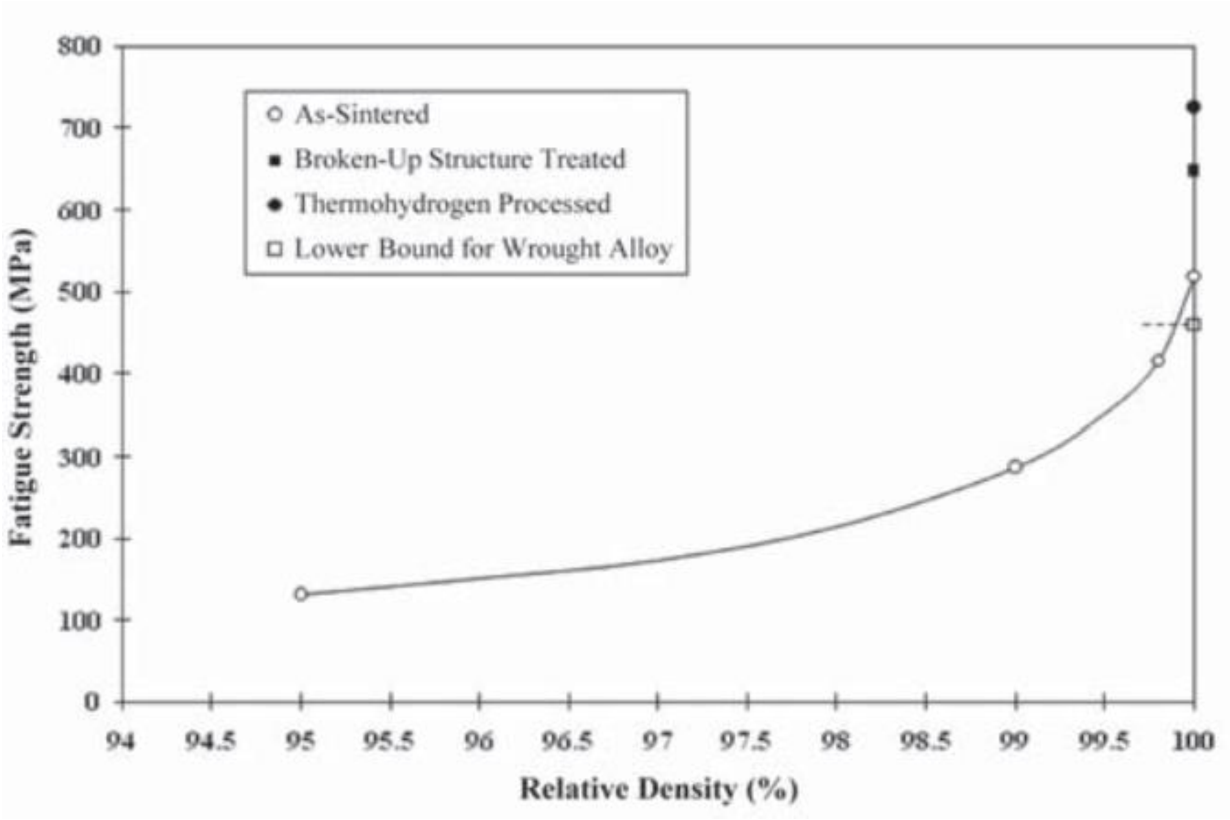

Figure 4 Fatigue Strength vs Sintered Density Ti-6Al-4V [4]

Wang et al. defined a controlled oxygen content is vital in improving the ductility of PM titanium, an oxygen content below 0.3% w/o is required to avoid a decrease in ductility. Microstructure refinement is beneficial to both the dynamic and static properties of PM titanium;

this can be achieved by optimizing the sintering process as well as post-sintering heat treatments this can be seen in Figure 5 below [4].

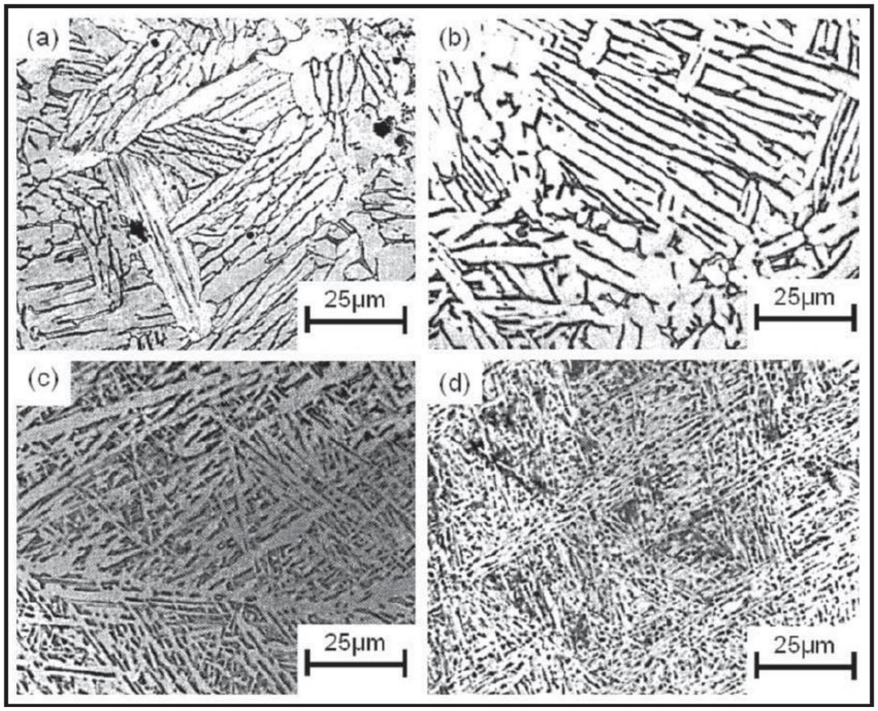

Figure 5 Repetitive microstructures of Ti-6Al-4V produced by different processes. (a) as sintered, (b) as HiPed, (c) BUS treatment, (d) THP treatment. Optical micrographs. [4]

2.1.6 Powder Metallurgy of Aluminum Alloys and Composites

The applications for aluminum in powder metallurgy are typically driven by aerospace applications with an emphasis on full density composites as structural members. The powder metal alloy is typically based on the 2000 and 6000 series aluminum alloys and contains copper, magnesium and/or silicon. Due to the large amounts of alloys that can be formulated within these series there is a focus within the published journals to the development and formulation of the representative powders which is outside the scope of this review. There have been studies showing both the improvement and degradation of mechanical properties when comparing powdered metallurgy to ingot manufacturing methods, however, it should be noted that these results are based on experimental alloys and the commercialized applications of these alloys have led to diminished properties as found by Pickens [19]. The powdered form of aluminum tends to absorb moisture from the surrounding environment. Moisture within the aluminum powder interferes with the sintering process and is one of the challenges to large scale production of PM aluminum components. The need for a de-gassing and consolidation stage proposes a barrier to large scale production [13]-[14],.

Table 1 Compositions and properties of selected commercial, wrought, cast and PM Aluminum alloys [21].

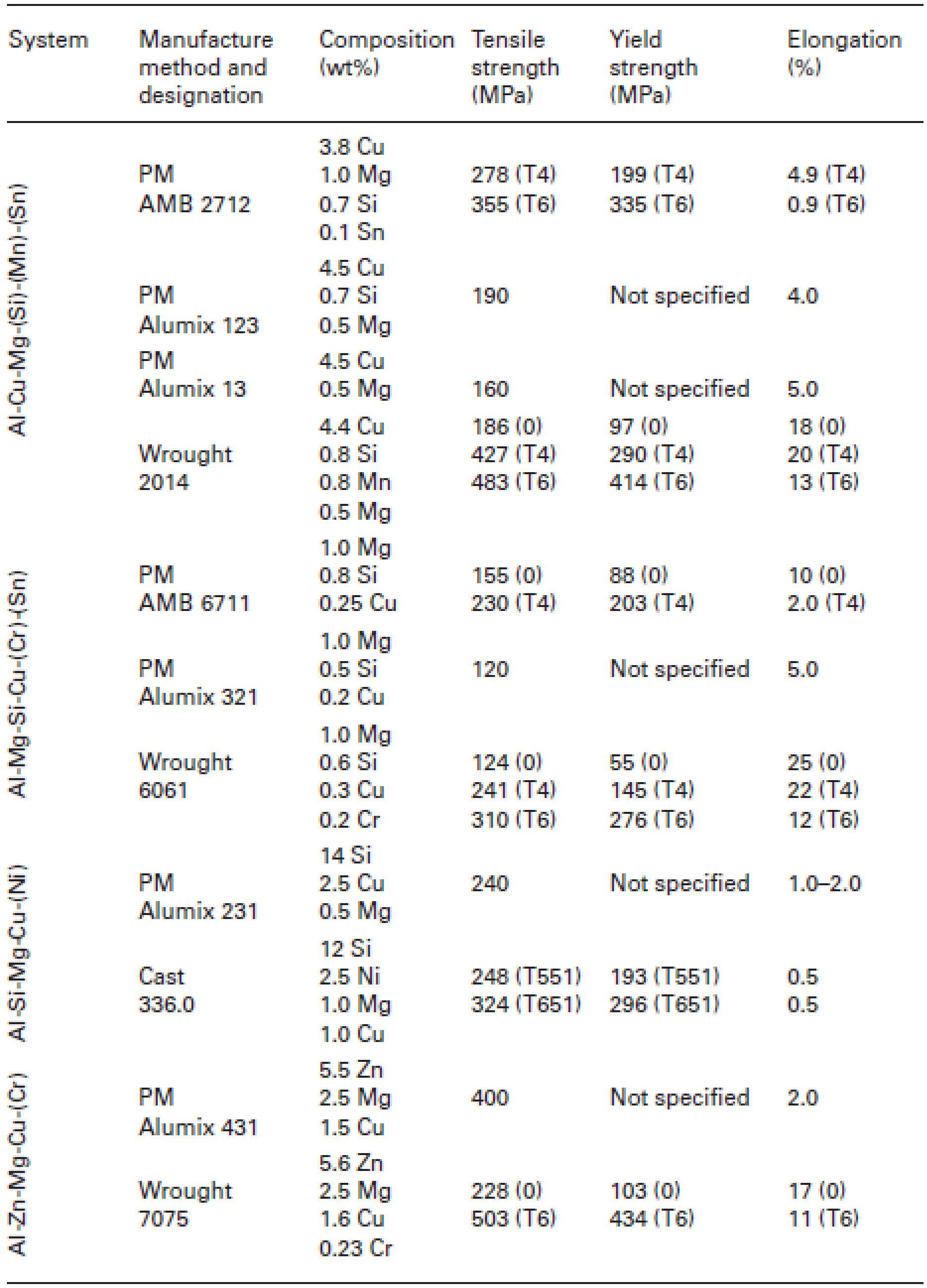

System	Manufacture method and designation	Composition (wt%)	Tensile strength (MPa)	Yield strength (MPa)	Elongation (%)
Al-Cu-Mg-(Si)-(Mn)-(Sn)	PM AMB 2712	3.8 Cu 1.0 Mg 0.7 Si 0.1 Sn	278 (T4) 355 (T6)	199 (T4) 335 (T6)	4.9 (T4) 0.9 (T6)
	PM Alumix 123	4.5 Cu 0.7 Si 0.5 Mg	190	Not specified	4.0
	PM Alumix 13	4.5 Cu 0.5 Mg	160	Not specified	5.0
	Wrought 2014	4.4 Cu 0.8 Si 0.8 Mn 0.5 Mg	186 (0) 427 (T4) 483 (T6)	97 (0) 290 (T4) 414 (T6)	18 (0) 20 (T4) 13 (T6)
Al-Mg-Si-Cu-(Cr)-(Sn)	PM AMB 6711	1.0 Mg 0.8 Si 0.25 Cu	155 (0) 230 (T4)	88 (0) 203 (T4)	10 (0) 2.0 (T4)
	PM Alumix 321	1.0 Mg 0.5 Si 0.2 Cu	120	Not specified	5.0
	Wrought 6061	1.0 Mg 0.6 Si 0.3 Cu 0.2 Cr	124 (0) 241 (T4) 310 (T6)	55 (0) 145 (T4) 276 (T6)	25 (0) 22 (T4) 12 (T6)
Al-Si-Mg-Cu-(Ni)	PM Alumix 231	14 Si 2.5 Cu 0.5 Mg	240	Not specified	1.0–2.0
	Cast 336.0	12 Si 2.5 Ni 1.0 Mg 1.0 Cu	248 (T551) 324 (T651)	193 (T551) 296 (T651)	0.5 0.5
Al-Zn-Mg-Cu-(Cr)	PM Alumix 431	5.5 Zn 2.5 Mg 1.5 Cu	400	Not specified	2.0
	Wrought 7075	5.6 Zn 2.5 Mg 1.6 Cu 0.23 Cr	228 (0) 503 (T6)	103 (0) 434 (T6)	17 (0) 11 (T6)

PM aluminum components are restrained to low-stress applications where cost reductions can be realized through the tight dimensional tolerances available through powder metallurgy. The mechanical properties of existing PM alloys do not meet the requirements for an expansion of their use, with increasing research into improving the stiffness and tensile strength for aluminum PM alloys new applications could arise. The experimental results reported by Pickens show an improvement in corrosion resistant within the PM alloy due to the formulation of oxides within the green state before sintering. Due to the limitations of aluminum powder metallurgy in high-stress environments the amount of experimental fatigue data is limited as stated by Grayson et al. As a result of the inclusion of pores, the fatigue of a sintered aluminum alloy can differ substantially, less than half of the equivalent wrought alloy. The ability to manufacture powders approaching the desired grain size of the matrix allows for a specific control of properties, strengthening mechanism and cooling rates that are not available through traditional ingot manufacturing make aluminum powder metallurgy the desired research path.[12], [20], [22]–[24].

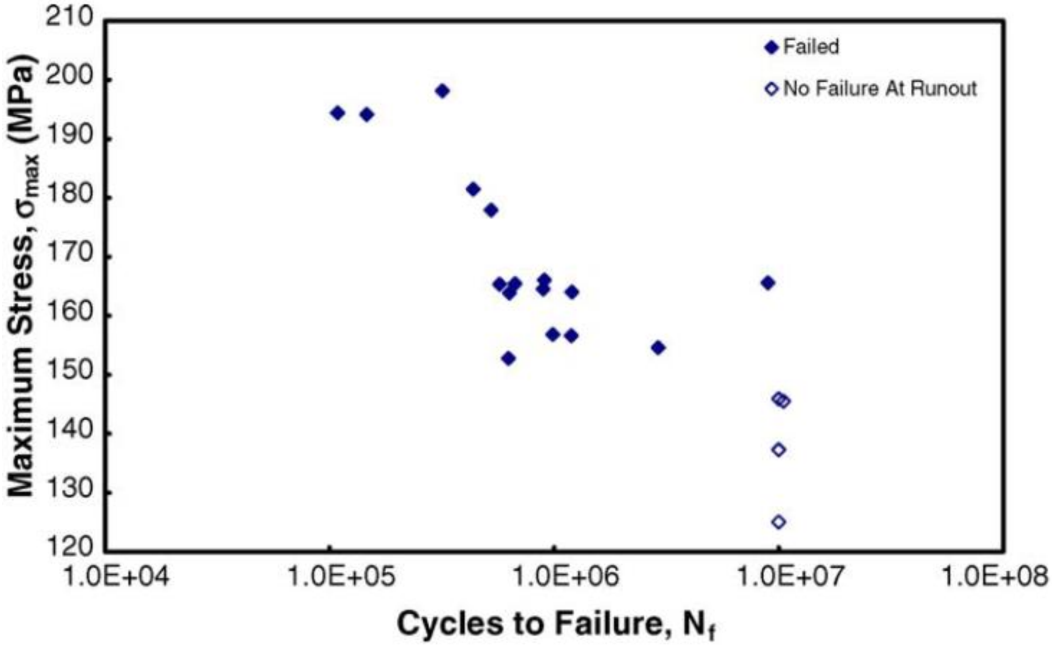

Figure 6 S-N Curve for AMB 2712 pressed at 200MPa and sintered for 30 min at 600°C, R=0.1 [12].

2.1.7 Additive Manufacturing with Powder Material

Additive manufacturing is a process that forms objects from a layer by layer application of material, this is different from subtractive manufacturing where the material is removed from an oversized material until the desired shape is met. This process is commonly known as 3D printing in the consumer markets and is widely adapted for use with polymers. Additive manufacturing using metals as the bulk material with numerous different methods for the production used to deliver the bulk material to the build layer. In a powder bed system, the powder is deposited upon a bed and a laser or electron beam is focused to the specific area that is to be sintered, another layer of powder is deposited by screening a layer of powder over the build area then the process is repeated [23]–[25].

Powder feed systems deliver powder to the laser or electron beam through a delivery system, and the monolayer of powder is sintered, the process builds upon itself. Systems can utilize a stationary workpiece and movable deposition head or vice versa, this ability achieves higher build volumes and can build upon previously manufactured components. Wire feed systems are similar in operation to powder feed systems with only the state of the material before deposition is different. Powder and wire feed methods are capable of larger build volumes then the powder bed methods, the specifics are dependent on the system manufactures. Since powder bed methods have to contain a large volume of powder that needs to cover the entirety of the working platform, the dimensions become cost prohibitive to build large parts [23], [26]-[27].

Due to a repetitive heating and cooling phases, zones may be subjected to several cycles of liquid phase to solid phase transformation. It is considered that AM manufacturing is a rapid solidification process. Depending upon the directionality of heat flow within the part columnar microstructures have been observed, other researchers have developed a solidification map as a function of cooling rate and solidification rate. Rapid solidification can reduce elemental partitioning and extend solid solubility resulting in a metastable phase formation. Controlling the directionality of heat extraction may affect the directionality of grain growth, as well the thermal cycling has shown microstructural banding. This process has developed the opportunity for porosities to form within the microstructures as well a lack of fusion between layers. Due to the cyclic thermal history, a complex relation is seen during the formation of the microstructure. Mechanical properties have been found to be anisotropic with regards to the formation direction, usually perpendicular to the build bed. Although with slower build volumes and control of the cooling rates it is possible to achieve mechanical properties close to that of conventionally produced materials. Dynamic properties are dependent on the degree of micro-porosity and surface finish, with proper post processing it is possible to achieve similar dynamic properties of conventional alloys. ASTM and SAE have begun to develop a standardizing system, however, since the industry is still in its infancy it has been indicated that an attempt to apply a standard at this point may do more harm to the industry. There are significant cost and time barriers to developing a comprehensive database that encompasses the industry with no guarantee that the data will remain consistent for the foreseeable future [23], [25]–[30].

2.1.3 Applications of Powder Metallurgy Components

Most of the PM self-lubricating bearings are manufactured using an iron based alloy with a controlled level of porosity to obtain an acceptable level of strength. The porosity level within the PM parts has a direct link to the strength of the material as demonstrated in Figure 7, due to the inclusion of voids within the microstructure introduced in the compaction and sintering process. Due to the inverse relationship between porosity and the strength of the material, a balance must be met where an acceptable level of fluid flow is achieved at a certain porosity and the part is able to withstand the applied stress. The benefits of substituting a low-density material instead of an iron based material produced by the powder metallurgy process can be realized as long as the same components can withstand the same state of stress. In this situation there are limitations on the dimension of the substituted materials as the benefit of decreasing the rotating mass should not be offset by increasing the overall moment of inertia [1]- [2] .

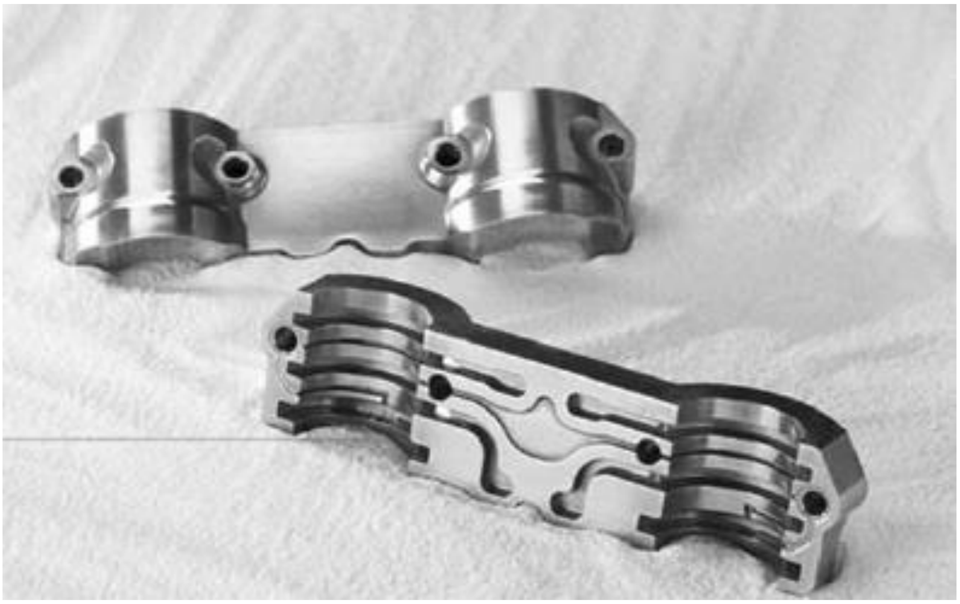

Figure 7 PM aluminum automotive components (automotive cam cap) [24]

Structural automotive components manufactured using PM techniques have seen a large uptake over past decades due to the cost efficiency, high volume capabilities and limited post-processing needed for PM parts. Many engine components are fabricated using PM such as connecting rods, drive pulleys and timing devices. The adoption of PM based structural parts has also been adopted in the motorcycle, small engine, lawnmower and metal cutting tool industries, the bulk of this production is ferrous alloy based. In the case of metal cutting industry the unique ability to incorporate high hardness materials in a ductile matrix is achievable through a PM process. Aside from structural or fully dense products the application of porosity controlled products consists of corrosion resistant materials with a degree of porosity for filtering. Design and production of wear resistant materials using biocompatible metals and stable oxides within the medical device and implant field where surface porosity can aid in tissue attachment [1]-[2].

Other properties that make PM produced parts desirable in other industries include electrical and electronic applications such as high-temperature lighting components, capacitors fabricated from refractory metals and oxide ceramics. Friction materials can be formed and manufactured for the use in clutches and brake components for the aerospace industry that alloy for greater energy dissipation with lower wear rates than conventional friction materials. Titanium and stainless steels are used in the powder metallurgy process to produce corrosion resistant materials such as orthodontic braces, watch parts as well as aerospace applications. Aerospace applications have driven the development of low-density materials used in PM applications like aluminum, titanium and beryllium to fabricate materials with high specific strengths. Composite materials such as aluminum and silicon carbide is a popular composite fabricated by powder metallurgy; the composite exhibits a higher elastic modulus and low thermal expansion coefficient when compared to aluminum. Diamond and metal matrix composites used in masonry cutting tools where fine diamond grains are dispersed in a metallic matrix. Growth potential for PM technology can be visualized in numerous industries including but not limited to micro-miniature devices, membrane filters, metal-ceramic seals and wear resistant structures [1], [2], [31].

2.2 Test Methods for Powder Metallurgy

2.2.1 Porosity

Porosity characterization is implemented to quantify the area porosity based on the light reflectivity from a metallographically polished cross-section of the coating. Care should be taken during polishing to avoid the introduction of artifacts or particle pull-out. Low viscosity epoxy resin and a vacuum chamber is recommended to ensure the pore structure is encapsulated to prevent altering the structure. Once the cross-sections are properly prepared an image is captured and post processed using an image analysis software such as ImageJ to convert the image into a binary mask, the area porosity is determined as the fraction of black pixels representing voids number of entire pixels in the image. Porosity can also be estimated theoretically by comparing the measured density of the material to the theoretical density of the material, the difference between the two would be caused by the voids that are present and therefore be a measure of porosity.

2.2.2 Density

The material density is an important factor in powder metallurgy as it is used as a classification for similar alloy compositions and is directly related to numerous properties of the material the method for testing density in powder metallurgy products is ASTM B962-15 and similar standard from the MPIF 42. The implementation of this measurement may be considered more practical than porosity measurements as metallographic sample preparation is not required and the sample can be tested as produced condition. This test method can also be easily applied to irregularly shaped parts due to the fact the density is calculated using Archimedes principle of buoyancy, in parts with a closed poor network the internal voids apply a buoyant force that can not be accurately measured so there is an inherent uncertainty in the reported density.

2.2.3 Hardness Testing

The Rockwell hardness test is an empirical indentation hardness test referred to as ASTM E18-12, which can provide useful information about the materials, which may correlate to tensile strength, wear resistance, ductility, and other physical properties. The test involves an indenter being brought into contact perpendicular to the test surface, which should also be perpendicular to equipment stage. A preliminary force is then applied for the specified dwell time and the baseline depth of indentation is measured. The test force is then applied at a controlled rate, which is also held for a specified dwell time, after which is removed and the final depth of indentation is measured and the hardness is calculated. Modern Rockwell testers are automated to apply the set loads for dwell times automatically, resulting in extremely effective and repeatable hardness testing. It should be noted that prior to testing any samples a calibration test should be conducted on a calibration block at the intended Rockwell scale to ensure the equipment is operating properly and upon completion of testing an additional calibration test should be conducted to confirm the accuracy of readings throughout the testing process. As with the density testing the presence of voids within the materials and specifically subsurface voids do not offer any resistance to the mechanical deformation of the indenter and as such the results from the test are typically reported as apparent hardness due to this reason [11], [32].

2.2.4 Fatigue Testing

The response to fatigue in powder metallurgy produced materials is significantly different than those produced through conventional methods, not only due the pores are natural initiation sites for cracks to form, they also limit the amount of cross sectional area that bears the applied load and cause stress risers within the material. This allows for plastic deformation to occur at pore sites as well provide a free surface that allows movement of dislocations along slip planes. Figure 8 shows the influence of density on increased crack propagation rates within materials containing high porosity as the stress intensity factor approaches that of the fracture toughness as stated by Cotterel et al. On the basis of structural parts subjected to repetitive loading, fatigue strengths is a defining value that determines the suitability of the material for the role [33].

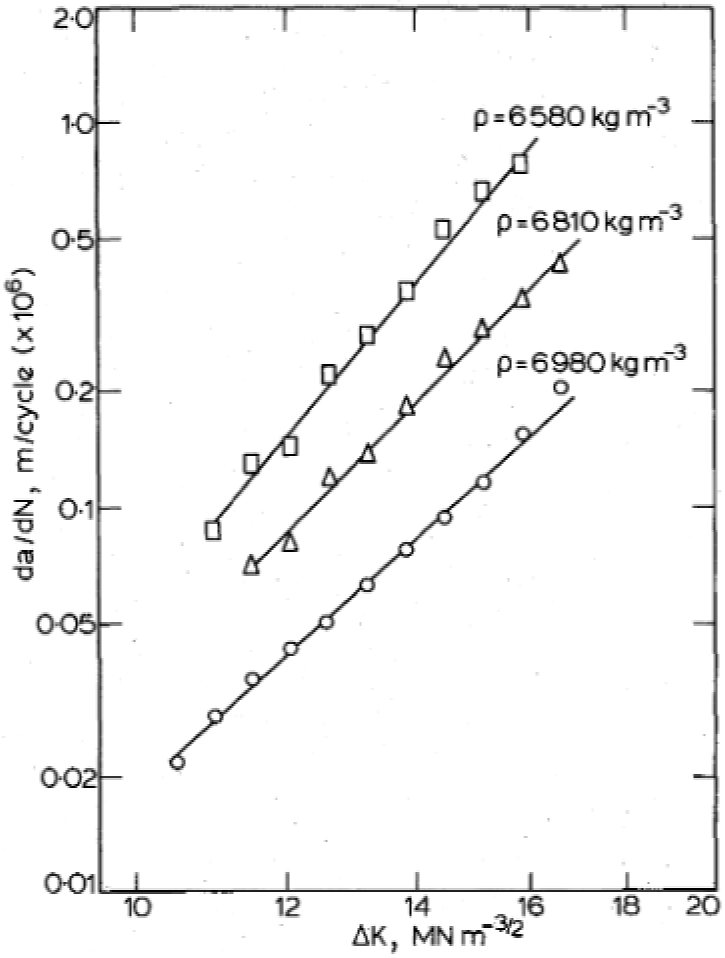

Figure 8 Effect of density on fatigue crack propagation in sintered steel [33]

The fatigue testing follows the standard of MPIF 56 for Rotating beam fatigue endurance limit that utilizes a staircase method to determine statistically the mean endurance limit and a valid confidence interval dependant on the number of test subjects. The method applies a fully reversed loading condition of R=-1, where the tensile and compressive stress are equal but opposite on every revolution of the sample. The testing begins at a predetermined stress that is dependant on the ultimate tensile strength of the material that was previously determined, the test is ran until a failure is detected or the samples survives for a minimum of 10^7 cycles. Depending on the success or failure of the previous samples the load is either increases on a previous run-out condition or decreased due to a failure, the process is repeated for a minimum of 25 test samples. The results from the test processed depending on the amount of total failures or passes and a mean endurance limit is calculated and the student's t-tables are applied to report a confidence interval based on the standard deviation of the mean is also reported for the 10% and 90% endurance limits [33]–[35].

2.2.5 Standards for Testing of Powder Metallurgy Products

Although the powder metallurgy process has been applied for a considerable amount of time over the past half century the method has seen a steady increase in market penetration into more common ferrous and even more recently non-ferrous materials. Due to this fact, the governing body overseeing powder metallurgy and powder processing, Metal Powder Industries Federation, is still in the process of developing applicable standards for all the new materials being produced by numerous manufactures. Aluminum product do not have a naming convention at the time of writing this thesis, however, the ASTM standard for naming aluminum alloys was used a reference based on the elemental composition. ASTM and MPIF standards are similar in testing and sample sizing and only differ in the matter of form and style dependant on the different group, this is due to the close collaboration between the two agencies, Table 2 lists all the applicable standards and current similar standards in other bodies [34], [36]–[38].

Table 2 Cross Index of Related Standards for Powder Metallurgy [8]

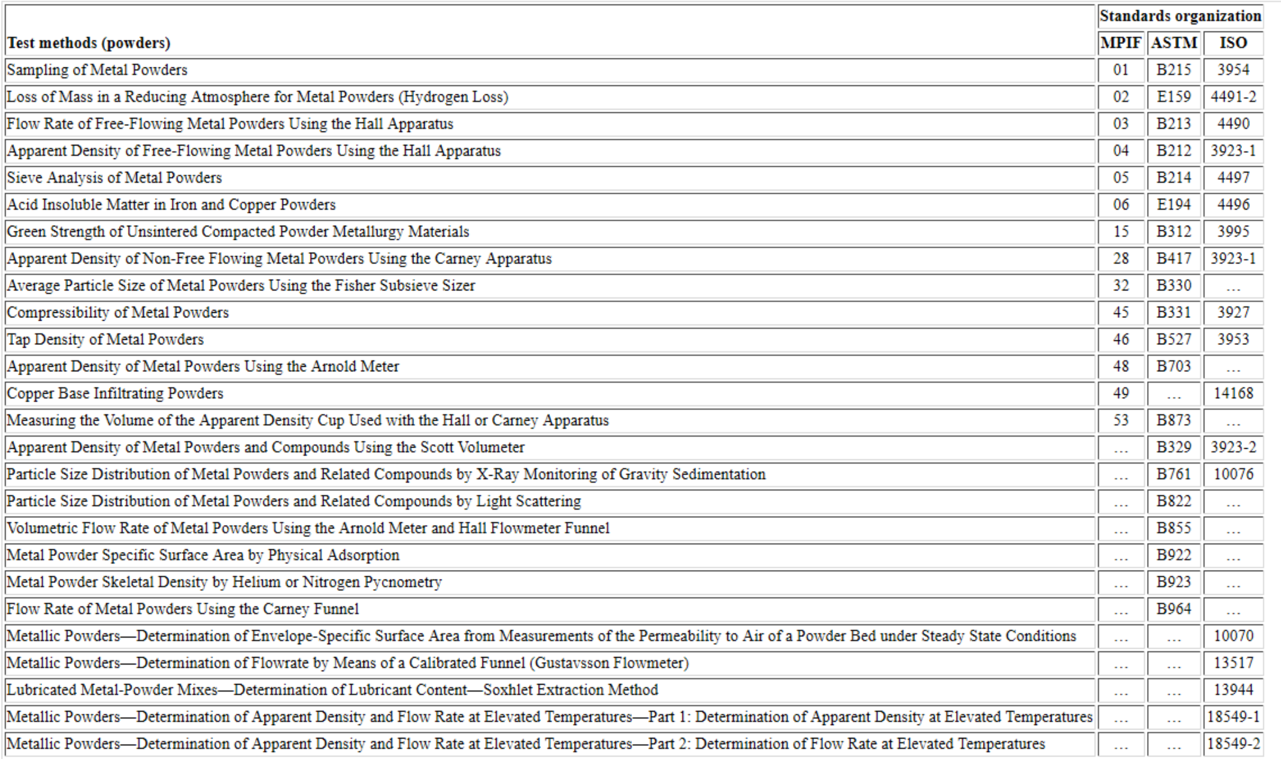

Test methods (powders)	Standards organization		
	MPIF	ASTM	ISO
Sampling of Metal Powders	01	B215	3954
Loss of Mass in a Reducing Atmosphere for Metal Powders (Hydrogen Loss)	02	E159	4491-2
Flow Rate of Free-Flowing Metal Powders Using the Hall Apparatus	03	B213	4490
Apparent Density of Free-Flowing Metal Powders Using the Hall Apparatus	04	B212	3923-1
Sieve Analysis of Metal Powders	05	B214	4497
Acid Insoluble Matter in Iron and Copper Powders	06	E194	4496
Green Strength of Unsintered Compacted Powder Metallurgy Materials	15	B312	3995
Apparent Density of Non-Free Flowing Metal Powders Using the Carney Apparatus	28	B417	3923-1
Average Particle Size of Metal Powders Using the Fisher Subsieve Sizer	32	B330	…
Compressibility of Metal Powders	45	B331	3927
Tap Density of Metal Powders	46	B527	3953
Apparent Density of Metal Powders Using the Arnold Meter	48	B703	…
Copper Base Infiltrating Powders	49	…	14168
Measuring the Volume of the Apparent Density Cup Used with the Hall or Carney Apparatus	53	B873	…
Apparent Density of Metal Powders and Compounds Using the Scott Volumeter	…	B329	3923-2
Particle Size Distribution of Metal Powders and Related Compounds by X-Ray Monitoring of Gravity Sedimentation	…	B761	10076
Particle Size Distribution of Metal Powders and Related Compounds by Light Scattering	…	B822	…
Volumetric Flow Rate of Metal Powders Using the Arnold Meter and Hall Flowmeter Funnel	…	B855	…
Metal Powder Specific Surface Area by Physical Adsorption	…	B922	…
Metal Powder Skeletal Density by Helium or Nitrogen Pycnometry	…	B923	…
Flow Rate of Metal Powders Using the Carney Funnel	…	B964	…
Metallic Powders—Determination of Envelope-Specific Surface Area from Measurements of the Permeability to Air of a Powder Bed under Steady State Conditions	…	…	10070
Metallic Powders—Determination of Flowrate by Means of a Calibrated Funnel (Gustavsson Flowmeter)	…	…	13517
Lubricated Metal-Powder Mixes—Determination of Lubricant Content—Soxhlet Extraction Method	…	…	13944
Metallic Powders—Determination of Apparent Density and Flow Rate at Elevated Temperatures—Part 1: Determination of Apparent Density at Elevated Temperatures	…	…	18549-1
Metallic Powders—Determination of Apparent Density and Flow Rate at Elevated Temperatures—Part 2: Determination of Flow Rate at Elevated Temperatures	…	…	18549-2

2.3 Purpose of Research

This research is conducted to test the mechanical and dynamic properties of proprietary lightweight materials produced as proposed replacement for a powder metallurgy produced ferrous based material. The proposed materials are produced by proprietary process of third party suppliers to be used in structural applications. Some of these materials were not commercially produced at the time of this thesis and remain in the development stage. The research offers a third-party analysis of the microstructure, elemental analysis, density, hardness, porosity, tensile strength, compression strength, and fatigue strength of these materials as it refers to the use of the material in a component of an internal combustion engine.

Chapter 3: Material and Experimental Methods

Chapter three provides an outline of the materials and experimental procedures used to characterize the mechanical and dynamic properties of powder metallurgy and additive manufactured materials, including porosity, hardness, density, tensile, compressive and fatigue strengths.

The materials are intended to replace the reference FC0205 materials in the current component of an internal combustion engine. The testing is done on all materials to establish a minimum based on the results of the FC0205 material, the other materials must meet or exceed these values to be considered a suitable replacement for the currently used material.

3.1 FC-0205

The material currently in use for the component of the internal combustion engine is a ferrous based alloy with main constituents of carbon and copper and is currently manufactured by an international sintered products company. Within the standard the materials are reported as have a range of values or a minimum value due to the probabilistic nature of the materials upon manufacture with a carbon range of 0.3 – 0.5% and copper content up to 2.5%. The FC0205 material is designates as copper infiltrated steel as the copper is used as a liquid phase sintering phase to enhance the densification of the steel [39].

3.2 Aluminum Alloy A

Aluminum alloy A is a cold press and sintered aluminum alloy that is equivalent to a A92014 alloy with main constituents of aluminum, copper and magnesium is manufactured by an American powder product manufacturer. No specifics of the powder or processing parameters, sinter temperature, sinter times or sinter atmosphere were shared during the research project.

3.3 Aluminum Alloy B

Aluminum alloy B is a cold press and sintered aluminum alloy with the main constituent of aluminum, copper and magnesium manufactured by a major international manufacturer of sintered materials. The elemental proportions of the alloy were not shared by the manufacturer before testing. No specifics of the powder or processing parameters, sinter temperature, sinter times or sinter atmosphere were shared during the research project.

3.4 Titanium A

Titanium A is a cold press and sintered commercially pure titanium material produced by an American titanium powder producer, the powder was produced by the same company as the compacted test subjects. No specifics of the powder morphology, sinter temperature or sinter atmosphere where given during the research project.

3.5 Titanium B

Titanium B is a commercially pure titanium manufactured by an additive manufacturing process developed by the company that supplied the test materials. The new proprietary method utilizing a plasma transferred arc solid free form fabrication where a metal powder is injected into a stream of plasma controlled by a robotic arm capable of 3-dimensional positioning. The part is built layer by layer from a CAD file and CAM software controlling the deposition nozzle.

3.6 Microstructural Analysis

This section describes the method of observing the microstructure after mechanical abrasion and chemically etching the surface.

3.6.1 Sectioning

To examine the as sintered microstructure of the samples the supplied samples were sectioned using a Buehler low speed diamond saw equipped with a 127mm IsoMet Diamond Wafering blade. The samples were cut using mineral spirits as a lubricant and running at approximately 250 rpm with a load of 500g. After sectioning the samples were cleaned with a steady stream of water to ensure complete cleansing of the pore structure, this was then followed by a gentle wash in isopropyl alcohol for the aluminum samples and ethanol for the titanium samples.

3.6.2 Mounting and Polishing

When the samples were completely dried they were mounted using epothin 2 epoxy mounting resin and hardener, the samples were placed in a vacuum chamber under a 1 atm vacuum for a minimum of 9 hours while curing. After the samples were fully cured they were roughly ground using 120 grit Silicon Carbide sanding disk on a metallographic polishing machine on both sides and set back into the mounting cups inverted from the original mounting orientation. A small quantity of epoxy was added to the mounting sleeves and set in the vacuum chamber at a 1 atm vacuum for a minimum of 9 hours, this ensured that all surface pores are set in epoxy to minimize the disturbance of the pore structure during grinding and polishing. The epoxy was chosen for the low viscosity and ability to fully infiltrate a porous structure. After the mounting procedure was completed the samples were ground and polished according to ASTM E3-11 using a manual rotary polisher. The grinding and polishing steps were similar for all samples and outlined in Table 3.

Table 3 Manual Grinding/Polishing Procedure [40]

Purpose	Lubricant	SiC Grit	Force Load (N)	Duration (s)	Surface Speed (RPM)
Planer grinding until all specimens are in the same plane	Water	120	20 – 30	30-300	200
Rough Grinding	Water	240	20 – 30	30	200

	Water	400	20 – 30	30	200
Fine Grinding	Water	600	20 – 30	30	200
	Water	800	20 – 30	30	200
	Water	1200	20 – 30	60	200
Rough Polishing	None	3 µm	10 - 20	300	100
Fine Polishing	None	1 µm	10 - 20	300	100

3.6.3 Etching

Once the samples were polished they were observed and recorded using a stereoscopic light microscope. The samples were then etched according to the outline described in ASTM E407-07 with Natal etchant 74 in standard was used to reveal the steel structure, Keller's etchant (3) and Kroll's etchant (192) was used for the aluminum and titanium samples respectively. The samples were then observed under with a light microscope before being observed with a FEI Quanta 200 FEG scanning electron microscope equipped with an EDAX (EDS) X-Ray detector at the Great Lakes Institute for Environmental Research(GLIER) [41].

3.7 Elemental Composition

This section outlines the process to determine the elemental constitutes of the test material through acid digestion and optical spectroscopy.

To determine the elemental constituents and their respective quantities within the test samples, small amounts of each sample were converted into powder to be analyzed using inductively conductive plasma optical emission spectroscopy. The titanium and aluminum samples were treated in an bath of isopropyl alcohol and ultrasonically cleaned and dried. A new file was used to prepare a small powder sample of at least 1 gram of each material. The powder sample was washed, filtered and dried prior to being sent to GLIER. At the GLIER the powders were digested in a solution of nitric acid and hydrogen fluoride and sealed in a Teflon container for 1 hour at room temperature. The solution was then heated to 100^{o}C for 4 hours in the closed container to ensure complete digestion. The sample was left for 12 hours at 80^{o}C with the container open under a fume hood to evaporate the hydrogen fluoride, then additional nitric acid was added and heated to 100^{o}C in a closed container for 4 hours. The solution was then separated into separate containers containing a 1% solution of nitric acid, a set of blank samples was prepared at the same time to be used as a baseline reading. The samples were then placed in an Aglient 720 ICP-OES and the spectroscopy reading were reported as a concentration of μg/g, with a minimum detection level of μg/kg. The concentrations were converted to weight percentages and reported as such.

3.8 X-Ray Spectroscopy

This section outlines the process of determining the crystallography of the test samples through X-ray diffraction.

Sectioned samples were prepared and sent to the University of Western Ontario's Department of Chemical and Biochemical Engineering for analysis in a Bruker Apex II Diffractometer. The diffractometer uses a Copper Kα wavelength of 0.15418 nm, the results were analyzed using a peak detection algorithm in MATLAB and then processed according to Bragg's Law where λ is the wavelength of Cu Kα [42].

$$Sin\,\theta = \frac{\lambda}{2d_{hkl}} \tag{2}$$

The results were further manipulated to attain the d spacing for specific planes within the structure using the following relationship.

$$sin^2\,\theta = \frac{\lambda^2}{4a_o^2}(h^2 + k^2 + l^2) \qquad (3)$$

Where all possible planes will diffract in positive integers dependant on the cubic structure of the material. The results were compared to published crystallographic data to determine if other elements were present.

3.9 Mass Properties

This section outlines the process to measure the density of the test materials through image analysis and buoyant force calculations.

3.9.1 Density

The density of each material was measured using Archimedes' principle according to ASTM B962 – 15, samples were prepared to a size that would fit in the test apparatus. The sample was then thoroughly rinsed and ultrasonically washed treated in an isopropyl alcohol solution then rinsed and washed in an appropriate solvent. The samples were then carefully dried, weighed, and then deposited into an oil bath, where the samples were vacuum impregnated for 30 minutes and then rested in the oil bath for an additional 30 minutes at atmospheric pressure to remove air and draw oil into pores within the coating. After vacuum impregnation, the samples were removed from the bath and excess oil was gently wiped away from the sample surface and reweighed. The sample was then suspended in room temperature water using a wire suspension rig, which allows for the suspended coating to be weighed while suspended in water without the beaker of water contacting the suspension rig or the scale a schematic of this is depicted in Figure 9. The diameter of the wires is dependent on the mass of the samples as outlined in Table 4.

Table 4 - Maximum recommended wire diameter for specimen suspension apparatus [43]

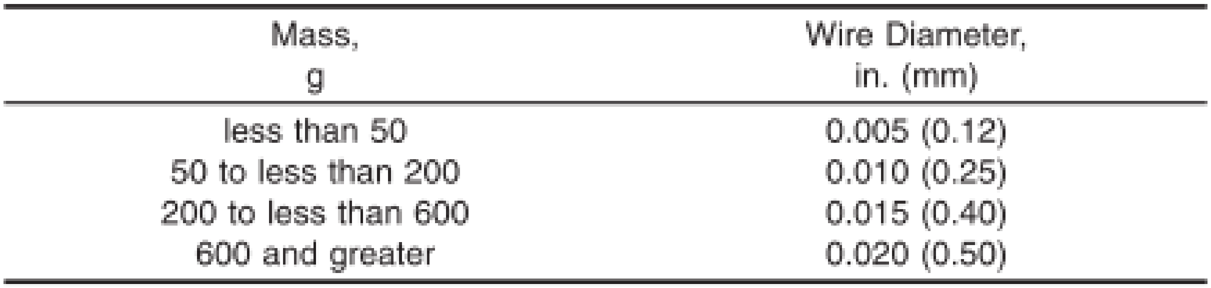

Mass, g	Wire Diameter, in. (mm)
less than 50	0.005 (0.12)
50 to less than 200	0.010 (0.25)
200 to less than 600	0.015 (0.40)
600 and greater	0.020 (0.50)

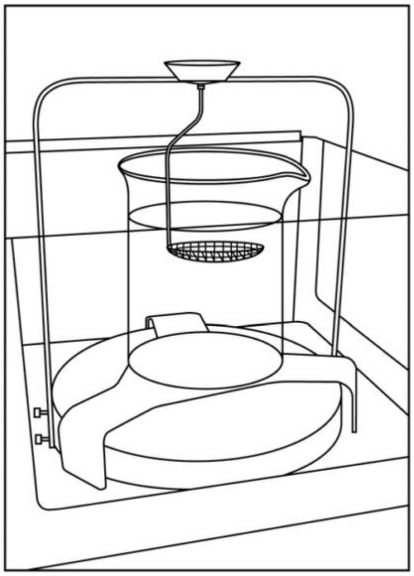

Figure 9 Beaker support above balance pan schematic, which allows for the mass of the suspended object within the basket to be weighed accounting for the force of buoyancy without the mass of the water suspension influencing the scale, according to ASTM B962 [43]

Then the coating density was calculated using Equation 4.

$$D = \frac{A \cdot P_w}{B - (C - E)} \tag{4}$$

Where: D is the coating density, A is the mass of the sample in air (g), B is the mass of the oil-impregnated sample (g), C is the mass of the oil-impregnated sample and suspension rig imbed in water (g), E is the mass of the suspension rig immersed in water (g), and P_w is the temperature dependent density of the water (g/cm^3).

3.9.2 Porosity

The coating porosity was determined from optical images of polished coating cross-sections according to ASTM E-2109, where the samples were prepared and polished as described in section 3.6.2. Once polished the sample cross-sections was observed using a light microscope, where the image was captured and processed using ImageJ. The image was converted to a grayscale image in ImageJ then the threshold value was adjusted to ensure the visible pores were included in the black pixel count without including any other surface artifacts that are not pores. The image was then converting to a binary mask which assigned a black or white color to the pixel according to the threshold value chosen previously, pores were assigned black pixels with the background as white pixels. The image particles were then analyzed using the "Analyze Particles" function within ImageJ, where the percent area is presented as a ratio of black pixels to total pixels within the picture, which estimates porosity of the specified area in a 2-dimensional plane. Images were assembled as composites over a large enough error to eliminates skewing the results with a large pore to image ratio. Porosity was also estimated using density calculated in 3.9.1, where the difference between a theoretical density estimated to be close to that of a fully dense A92XXX series alloy 2.8 g/cm^3 and 4.5 g/cm^3 when comparing the titanium materials [42]-[43].

3.10 Hardness

This section outlines the techniques used to determine the hardness of the materials by measuring the amount of deformation caused by an applied load upon a specific indenter geometry.

The hardness was measured using a Mitutoyo Rockwell hardness tester Figure 10, set to B scale according to ASTM E-18. As per the standard procedure a steel ball indenter was used with an indentation force of 100 kgf. Prior to testing a calibration test was conducted on a HRB calibration block to confirm the hardness tester is calibrated and operating normally. Then 10 indentations on each sample were completed with the distance between subsequent indentations at least three times the diameter of the previous indentation to avoid error associated with strain hardening of the sample. After the testing was completed an additional calibration test was conducted to confirm the equipment was still operating accurately. From the 10 indentations of each sample mean and standard deviations were computed.

Figure 10 Mitutoyo Rockwell hardness testing machine

3.11 Tensile Testing

This section outlines the process to used to test the tensile properties of the material through the application of a tensile load applied axially.

Tensile testing was conducted per ASTM E8 (MPIF 10) where a tensile sample is subjected to a load that is parallel with the long axis of the test piece. The tensile testing was conducted using an MTS Criterion universal testing machine with a maximum load of 150kN. The tensile samples were fabricated according to the shape and size parameters as described by Figure 11 and Table 5. The test samples were measured with calipers at three separate regions of their gauge, the measurements were averaged and recorded to determine the cross-sectional area. The samples were loaded into the jaws of the test sample, care was taken to ensure the grip sections were adequately and evenly situated in the grip and the sample was parallel to the cross-head axis. The extensimeter was attached to the gauge section of the test subject. The data signals were zeroed with the machines software testing software, including load, cross-head displacement and extensometer readings. The cross-head speed was set to 0.05 mm/min and the test was started, the cross-head strain was applied constantly until a failure was detected by the software.

The data was then analyzed in raw data form to determine the Young's modulus, 0.2% strain offset yield strength, ultimate tensile strength and maximum elongation of the material. The stress strain graphs were inspected for anomalies. The test was run a minimum of three times per material and the materials properties are reported.

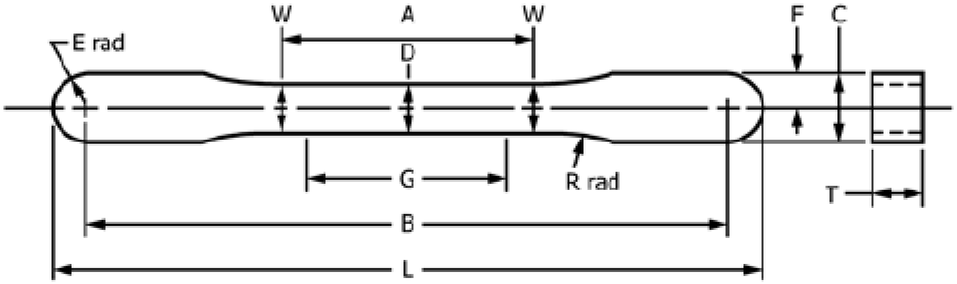

Figure 11 Tensile test sample geometry for powder metallurgy produced samples

Table 5 Die Sizing for tensile test samples

	Die Dimensions Tensile Sample	[mm]	±
G	Gauge Length	25.4	0.08
D	Width at center	5.72	0.03
W	Width at end of reduced parallel section	5.97	0.03
T	Compacted thickness	4.955	1.395
R	Radius of Fillet	25.4	
A	Length of reduced parallel section	31.8	
B	Grip length	80.95	0.03
L	Overall length	89.64	0.03
C	Width of grip section	8.71	0.03
F	Half-width of grip section	4.34	0.03
E	End radius	4.34	0.03

3.12 Compression Testing

This section outlines the procedure to determine the compression characteristics by applying a compressive load to a sample.

Compression testing was completed as per ASTM standard E9-09 (MPIF 61) using an MTS criterion universal testing machine with compression platens installed. The compression pins were placed in the center of the platen with a low friction material added to either end to prevent binding and barrelling of the test sample. The top platen was brought into contact with the test sample and the load and crosshead data signals were zeroed. The test was conducted at a crosshead speed of 0.05 mm/min and was ran until failure of the samples was detected. The resulting data was processed to determine the compressive yield strength and ultimate compressive strength of the material [31], [46].

3.13 Fatigue Testing

This section outlines the process to determine fatigue stress confidence interval using a rotating beam fatigue machine.

Fatigue testing was carried out according to the guidelines set out in the MPIF 56 standard, there is currently no equivalent standard from ASTM for fatigue of powder metallurgy metallic materials. The samples were fabricated according to the specification outlined in the standard presented in Figure 12 the dimensions are presented in Table 6. The loading condition for a rotating beam fatigue machine determined by the following equation:

$$M = \frac{\pi \sigma_a D^3}{32} \tag{5}$$

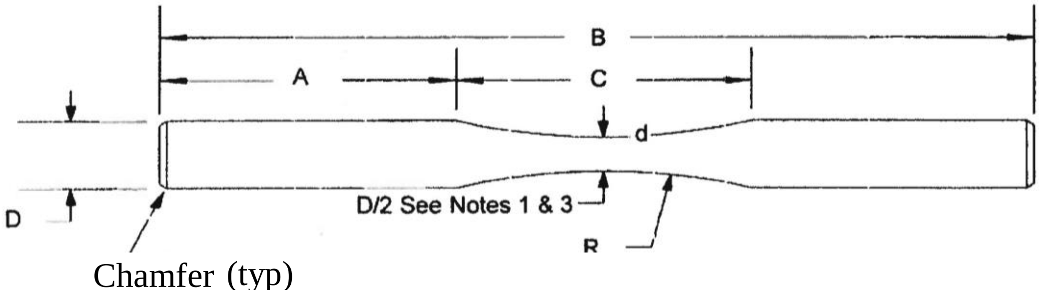

Figure 12 Fatigue Test specimen geometry

Table 6 Dimensions for fatigue testing samples

Diameter D [mm]	A [mm]	B [mm]	C [mm]	R [mm]

9.52 ± 0.001	25.40 ± 0.200	75.00 ± 0.200	25.40 ± 0.050	34.93 (Ref.)

The samples are inspected and lightly smoothed with #000 steel wool, care was taken to limit the grinding was parallel to the long axis of the sample as to not impart an artificial stress riser to the outer edge of the test sample. The test piece was loaded into the drive collet and secured then the free end collet was secured to the sample with the weight supported. The machine was started and the rotation was observed to ensure the sample did not exhibit signs of run-out. The desired test condition was set on the load bar and the clamp was secured to prevent movement of the load block. The load support was removed with care taken not to apply the load in a sudden motion while the sample was rotating at a slow speed. Once the machine was set in the running condition the speed was increased to approximately 10000 rpm, this was verified with a photo tachometer that read a reflective indicator attached to the spindle. The counter was reset to zero and the test was conducted until failure of the test subject or a minimum of 10^7 cycles was accomplished.

As per the standard the starting stress for the sample was determined from the ultimate tensile stress, the initial stress estimated to be about a third of the UTS. The testing followed a staircase method that depended on the results of the previous test, if the sample achieved runout the stress was increased by a step size and the test was ran again at the higher stress. If the sampled failed to meet 10^7 cycles before failure the test was recorded as a failure and the next sample was run at a stress lowered by the step size, the stress was increased by approximately 10 MP and this step size was consisted for all materials and fatigue testing. The amount of cycles was recorded along with the calculated stress in the sample. Failed samples were inspected to ensure that the fracture occurred with the minimum cross section of the sample, another outside of this area was considered an invalid result and the test was repeated. Upon completion of a minimum of 25 fatigue tests the results were tabulated with passing tests indicated with ‘O’ and failures denoted as ‘X’. The mean alternating stress was calculated using a weighted factor depending on the greater number of passes or failures within the samples set, according to equation 5. A is the product of the frequency and step increase of the results, B is the product of the step increment squared and the frequency value. σ_{a0} is the minimum stress amplitude that corresponds minimum the total of pass or fails within the test group, d is the step size for all testing this was held constant at 10 MPa.

$$\sigma_{A,50} = \sigma_{a0} + d\left(\frac{A}{N} \pm 0.5\right) \tag{6}$$

Students’ t tables were applied to the number of test conducted to report a confidence interval of 10% and 90% survivability probability. The results were also summarized in an S-N curve for each material tested [34].

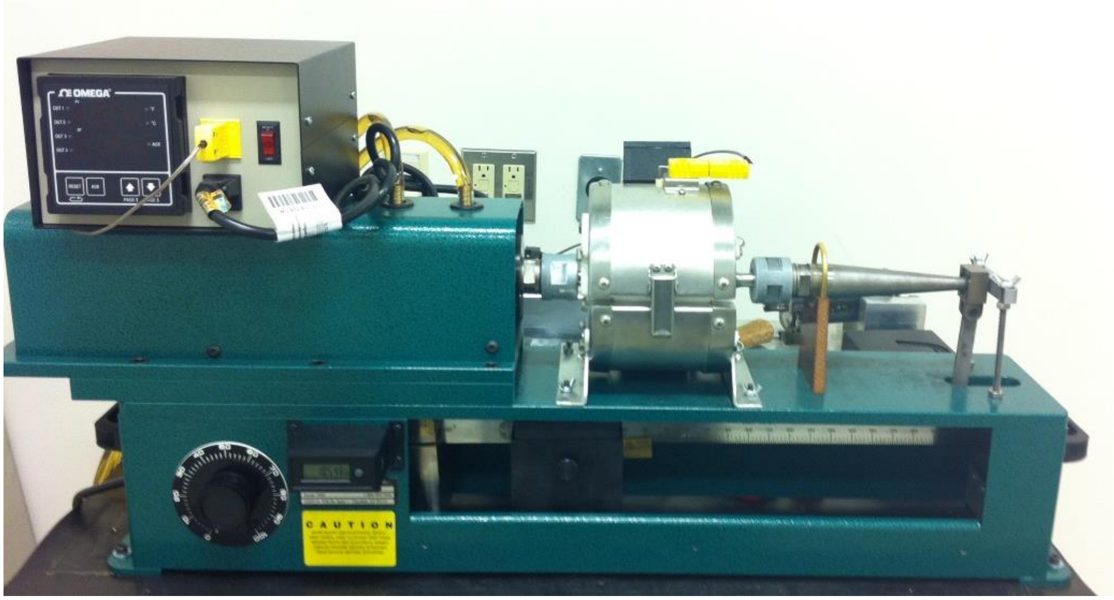

Figure 13 RBF-200 HT rotating beam fatigue machine

Chapter 4: Experimental Results

This chapter outlines the results obtained from the experiments conducted on the test materials presented in chapter 3. The test results are organized in the same manner as they were completed.

4.1 Density

This section outlines the results of the density measurements of researched materials in the as received conditions, measured according to ASTM B962 using Archimedes method. The density is required to properly characterize the materials and is common practice in the powder metallurgy industry. The test piece was measured prior to the experiment by placing it on a calibrated scale that was tared before taking the initial measurement, the result was an average of three separate mass readings in grams. The material was submerged in an SAE 5W-30 motor oil then placed in a vacuum chamber at 1 atm for 30 minutes to allow the oil to penetrate the exposed pore structure then allowed to sit in the oil for a further 30 minutes under normal atmospheric conditions. A wire holder was fabricated using a 0.12mm wire conforming to the standard the wire holder was placed in a beaker of water suspended over the scale and positioned that only holder would be placed on the calibrated scale. The mass of the wire assembly submerged in water was recorded and the temperature of the water was recorded. The sample was placed in the wire basic that was prepared for the test apparatus and carefully submerged in the water beaker, care was taken not to disrupt the test setup, the mass of the test sample was then recorded.

4.1.1 FC0205

Table 7 B962-15 Test results to determine Archimedes density of FC0205.

FC0205 Archimedes Density Values	
7.759	Mass of Test Piece in Air (g)
7.595	Mass of oil impregnated sample (g)

8.906	oil impr. And support immersed in water (g)
2.438	Mass of support immersed in water (g)
0.998	Density of water (g/cm^3)
6.875	Density of material based on Equation (4)

The density from the procedure was found to be 6.875 g/cm^3, taking the accepted density of copper steel to be 7.6 g/cm^3 [47] the porosity can be calculated from the difference and was found to be 10.96%. There is almost 59% difference between the porosity found through image analysis and Archimedes density, the error can be attributed to the process of taking a 2-dimensional look at the pore structure which does not give a true representation of the 3-dimensial pore structure as well the degree of interconnectivity between the pores does have an effect on the Archimedes density [1], [16], [39], [43], [47].

4.1.2 Aluminum Alloy A

Table 8 Test Results of Archimedes Density on Aluminum A

Aluminum A Archimedes Density Values	
2.818	Mass of Test Piece in Air (g)
2.820	Mass of oil impregnated sample (g)
4.161	oil impr. And support immersed in water (g)
2.438	Mass of support immersed in water (g)
0.998	Density of water (g/cm^3)
2.566	Density of material based on Equation (4)

The density of the sample determined by ASTM standard B962-15 is 2.566 g/cm^3 and using the published density data for 2XXX series aluminum alloys of 2.78 g/cm^3 a porosity of 7.71% with an experimental error of 21.83% between the porosity measurements. The chemical composition falls in the range 2XXX series aluminum alloys [44].

4.1.3 Aluminum Alloy B

Table 9 Test Results of Archimedes Density on Aluminum B

Aluminum B Archimedes Density Values	
3.378	Mass of Test Piece in Air (g)
3.382	Mass of oil impregnated sample (g)
4.588	oil impr. And support immersed in water (g)
2.438	Mass of support immersed in water (g)
0.998	Density of water (g/cm^3)
2.737	Density of material based on Equation (4)

The density of the sample determined by ASTM standard B962-15 is 2.736 g/cm^3 and using the published density data for 2XXX series aluminum alloys of 2.78 g/cm^3 and a porosity based on density was found to be a 1.58%, comparing that to 2.09% found through image analysis shows a good correlation the porosity is randomly distributed with small pores.

4.1.4 Titanium A

Table 10 Test Results of Archimedes Density on Titanium A

Titanium A Archimedes Density Values	
3.066	Mass of Test Piece in Air (g)
3.067	Mass of oil impregnated sample (g)
4.759	oil impr. And support immersed in water (g)
2.438	Mass of support immersed in water (g)
0.998	Density of water (g/cm^3)
4.107	Density of material based on Equation (4)

The results from the Archimedes testing resulting in a density of 4.11 g/cm^3, given the accepted value of 4.51 g/cm^3 a porosity of 8.96% is found using the Archimedes method and with a porosity of 6.25% found through image analysis with an experimental error of 30.21% between the methods. The difference between the methods seems to grow as the size of the closed pore structure provides more buoyant force and lowers the mass found in the Archimedes method.

4.1.5 Titanium B

Table 11 Test Results of Archimedes Density on Titanium B

Titanium B Archimedes Density Values	
5.427	Mass of Test Piece in Air (g)
5.434	Mass of oil impregnated sample (g)
6.660	oil impr. And support immersed in water (g)
2.438	Mass of support immersed in water (g)
0.998	Density of water (g/cm^3)
4.469	Density of material based on Equation (4)

Applying ASTM B962-15 the density is 4.469g/cm^3 and considering the accepted standard density of pure titanium to be 4.507 g/cm^3 the porosity can be determined to be 0.913% with an experimental error between the two methods of 73.06% [44].

4.2 Porosity

This section represents the results from image analysis of the optical images of the test materials using optical microscopy in the polished and etched stated. The porosity is an indication of the 2-dimensional pore structure of the material with a direct correlation to material properties. All samples were sectioned using a low-speed saw with a diamond blade, then set in cold mount epoxy resin. The samples were ground and polished according to the prescribed system. Images were then taken using a stereo microscope after the polishing, then the images were analyzed using the ImageJ software to determine the porosity.

4.2.1 FC0205

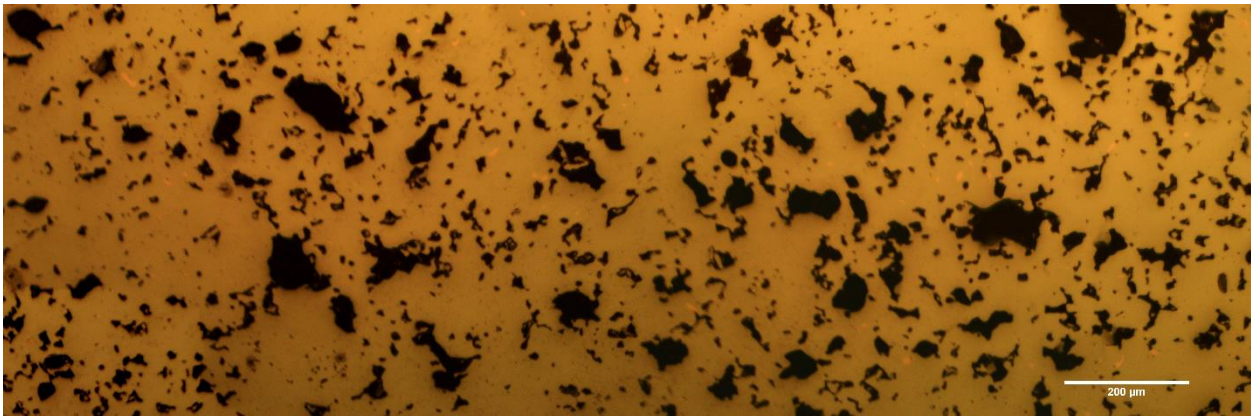

Figure 14 Composite image of FC0205 Sample was polished to reveal pore structure 100X magnification

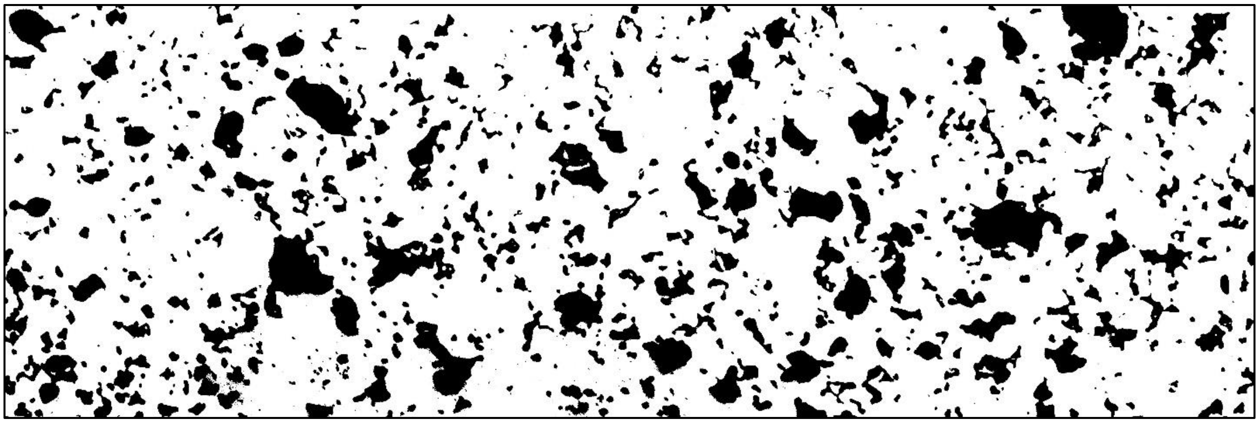

Figure 15 Binary image was produced from Figure 14 for pore analysis

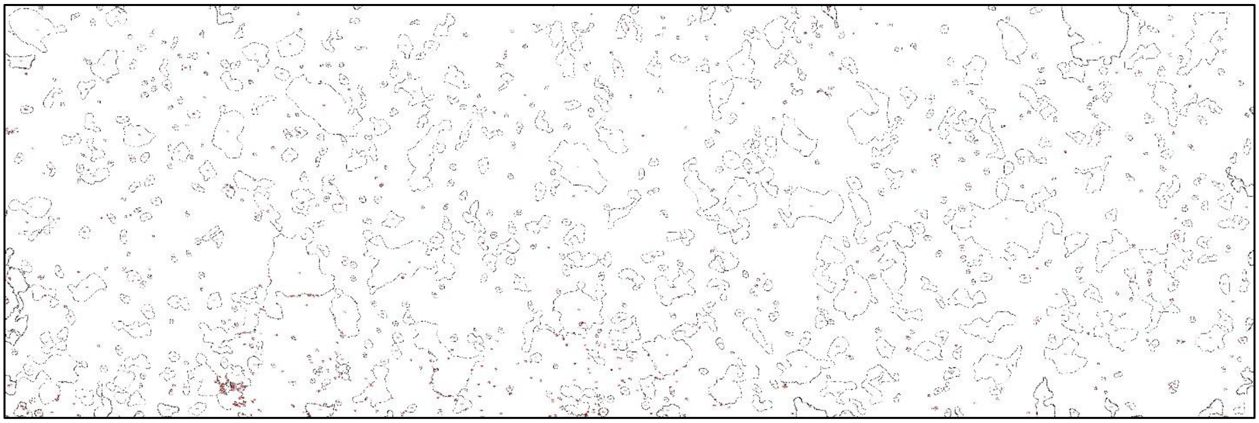

Figure 16 Individual pores identified and measured using ImageJ from Figure 15

The FC0205 sample was sectioned and encapsulated in low viscosity epoxy under vacuum to ensure there was no artificial damage done to the pores during sample preparation. Using ImageJ to analyze the pre-etched micrographs for pore size and degree of porosity by converting Figure 14, to a binary image Figure 15 and finding the ratio between black pixels and the total pixels contained in the image. The porosity was found to be 17.42% by area fraction. The pore size and distribution was also tabulated from Figure 16, with an average pore area to be .02 % of the total area with a deviation of .06% by area. This was averaged over several areas and the images are a sample of the process completed on this area. As the image area is smaller the presence of large pores will artificially skew the porosity measurements which is why this method has not been adopted as a standard measurement within the industry, this was studied to determine a correlation between the structure and strengths.

4.2.2 Aluminum A

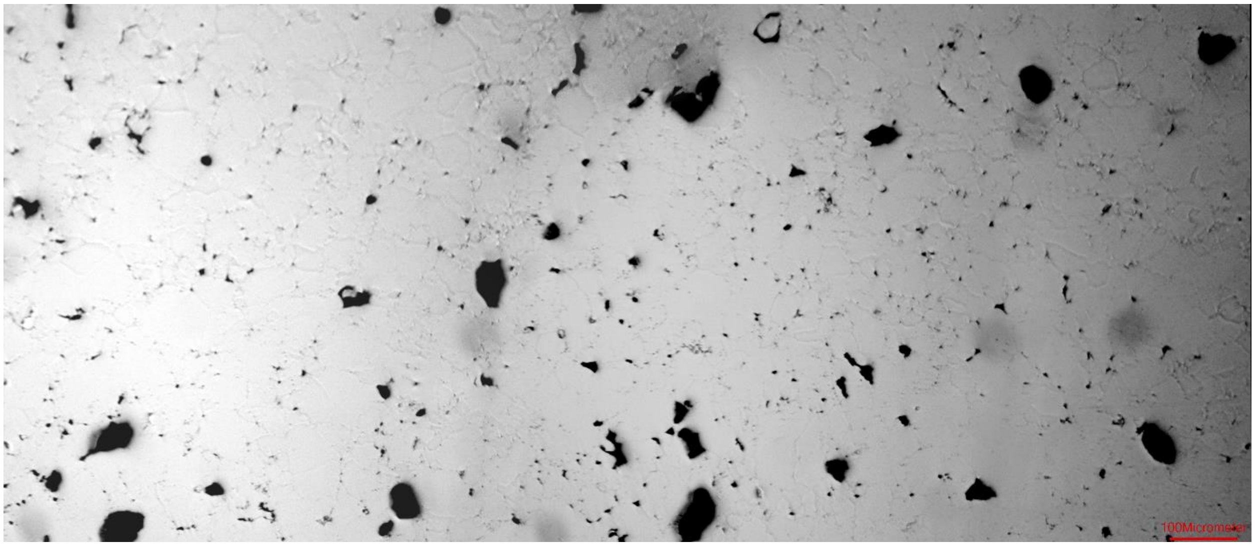

Figure 17 Composite image of Al A polished sample before etching 100X magnification

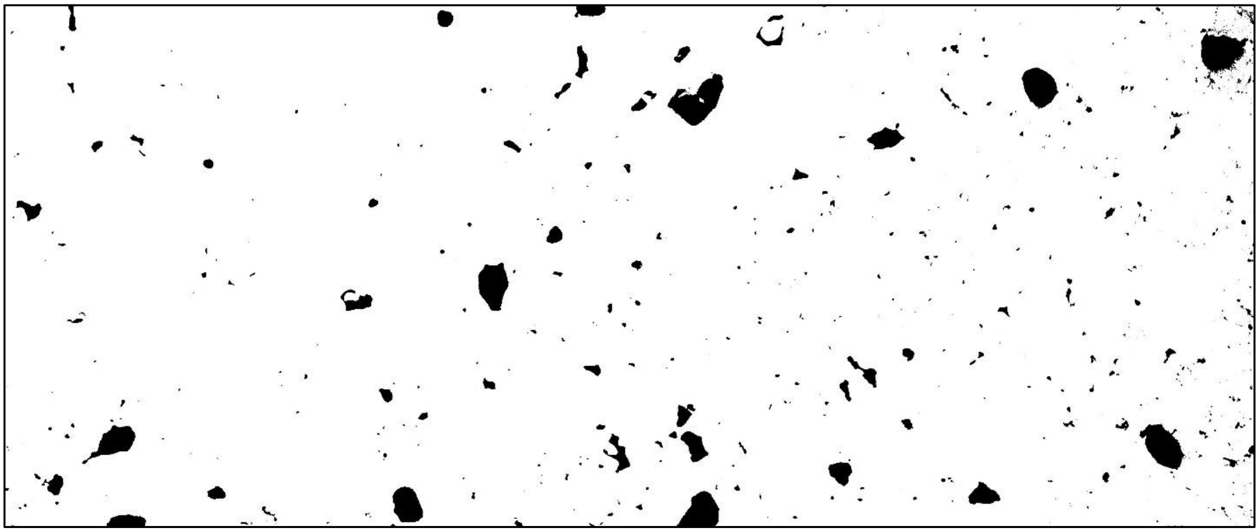

Figure 18 Binary image mask created from polished optical image Figure 17

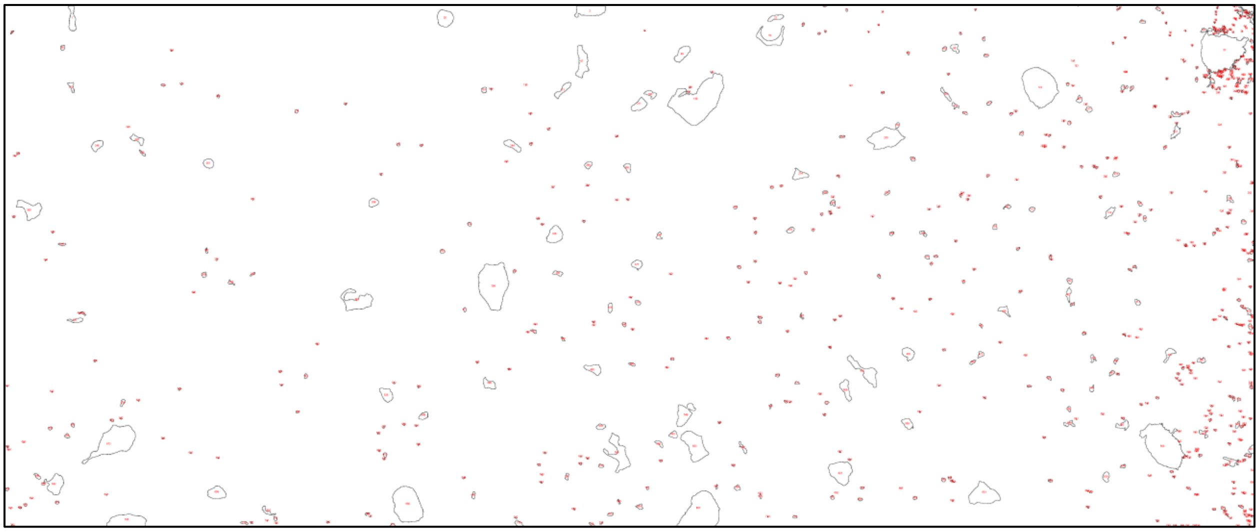

Figure 19 Pore identification from binary mask Figure 18.

After grinding and polishing the cold mounted samples optical images were taken under a stereo microscope to acquire the image in Figure 17. Image analysis determined a porosity of 6.03% with an average pore size of 0.127% with a standard deviation of 0.62% with respect to total area by a binary mask in Figure 18 and pore distribution in Figure 19. Pore sizes varied across the samples from large to small, with a majority of smaller pores observed. Some of the larger pores were identified as a coalescent of smaller pores. The pore structure between the aluminum samples show a variation in size and shape although the mechanical properties are relatively close between the materials. This may lead to a correlation between the size and structure of the pores that is a critical factor affecting materials properties of these tested materials that are equally important to the overall porosity of the material.

4.2.3 Aluminum B

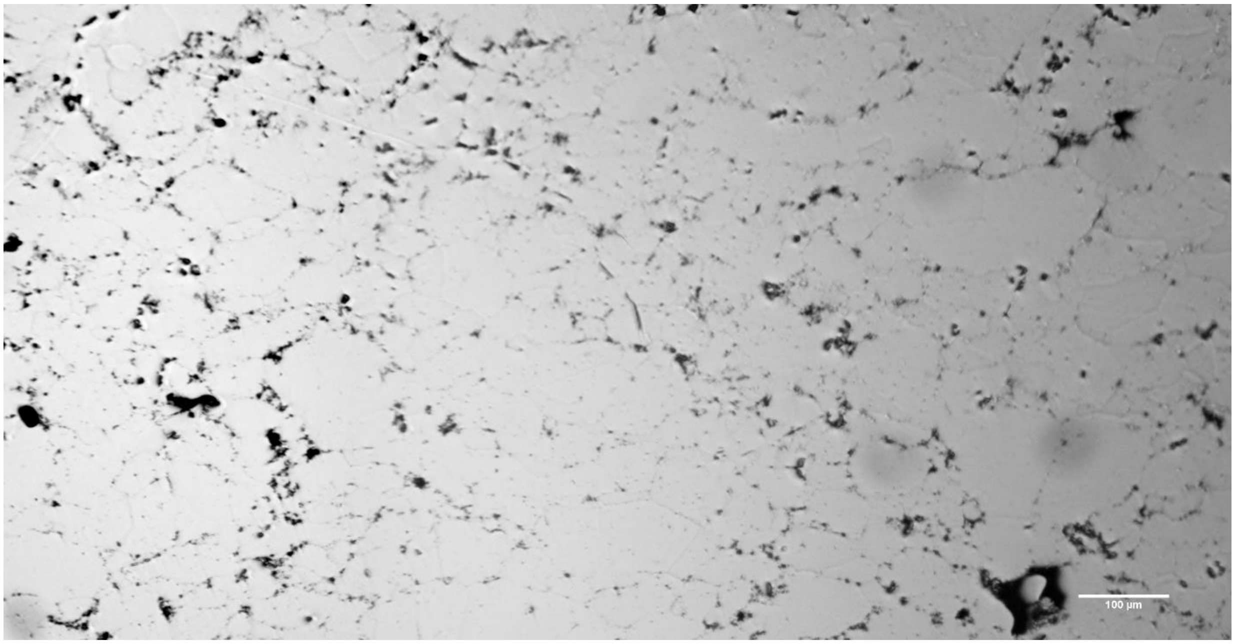

Figure 20 Composite image of polished sample of Al B 100X Magnification

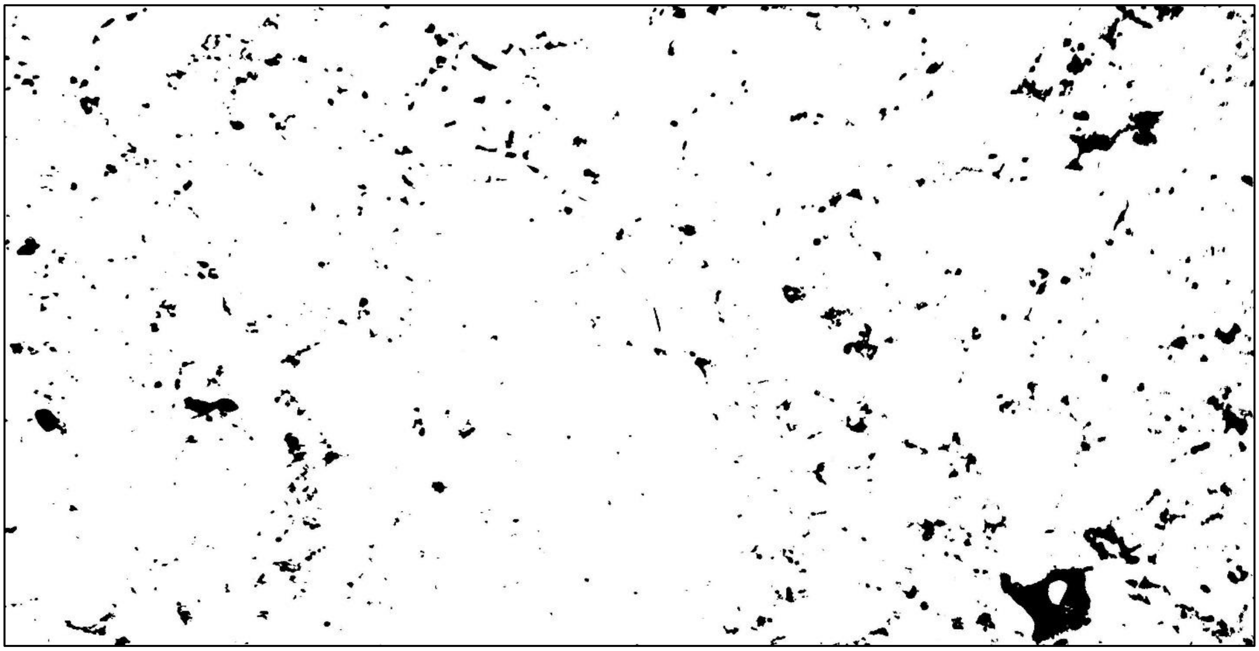

Figure 21 Binary image mask of pore structure constructed from polished image from Figure 20

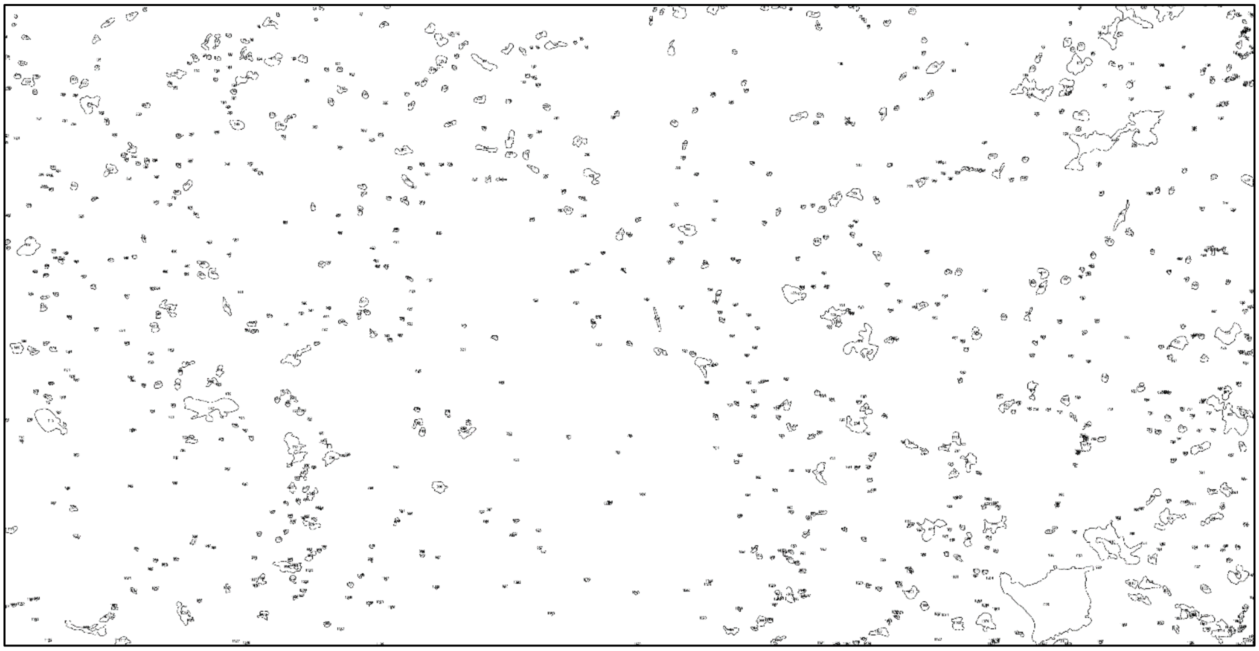

Figure 22 Pore identification from binary image mask of polished sample.

Image analysis of Figure 20 was done my making a binary mask shown in Figure 21 determined a porosity of 2.093% with an average pore size determined from Figure 22 of 0.09% and a standard deviation of 0.47%. The Al-B samples showed a random distribution of pores with an overall smaller pore size when comparted to the other aluminum sample, the difference in pore morphology can be attributed to the size and shape of the powder products that were used to make the compact. The press and sinter parameters can also change the size and distribution of the pore structure, however, none of these parameters were disclosed during the research project.

The aluminum materials seem to be sensitive to the pore size and structure as well as overall porosity, possibly arising from the tendency to form in irregular shapes with sharp corners that is found in greater number in the aluminum samples over the titanium materials. The FC0205 reference sample has similar pores structure with a mixture of smooth pores and irregular shaped pores, the mechanical properties indicate a lower sensitivity to these structures but more testing would be needed to confirm.

4.2.4 Titanium A

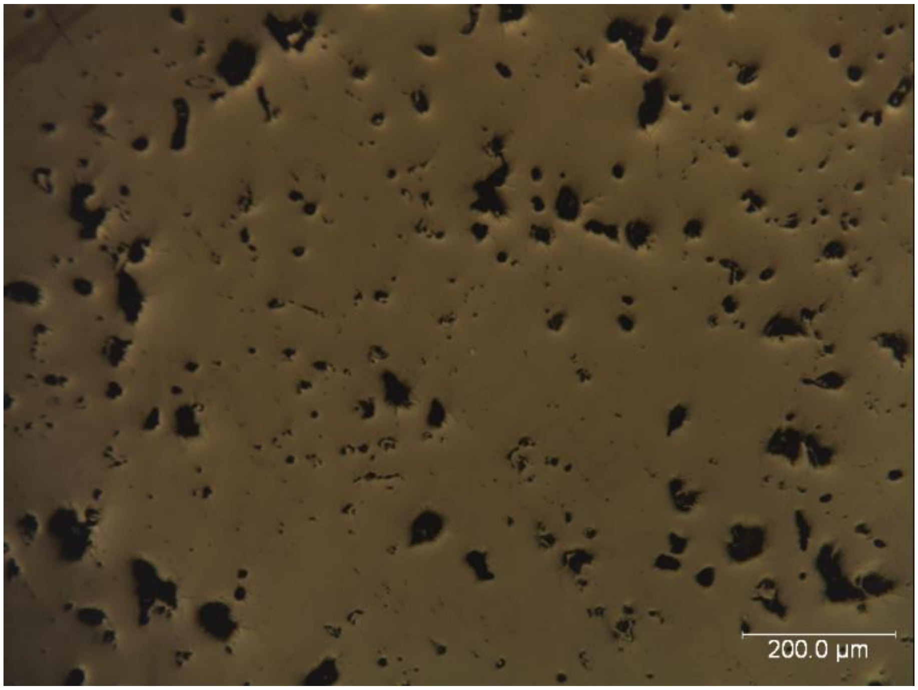

Figure 23 A Titanium polished sample at 100X magnification

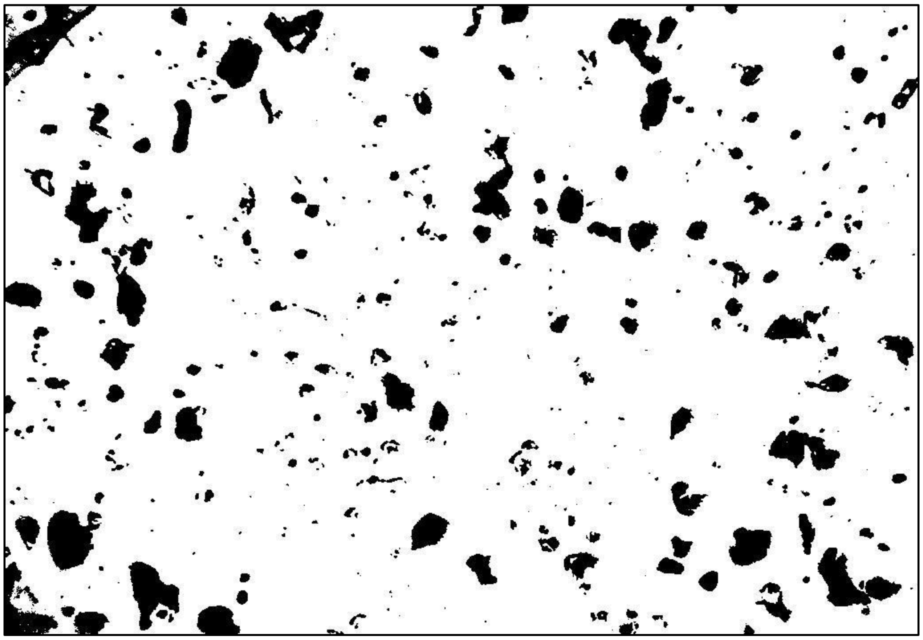

Figure 24 A Ti binary image mask constructed from polished sample.

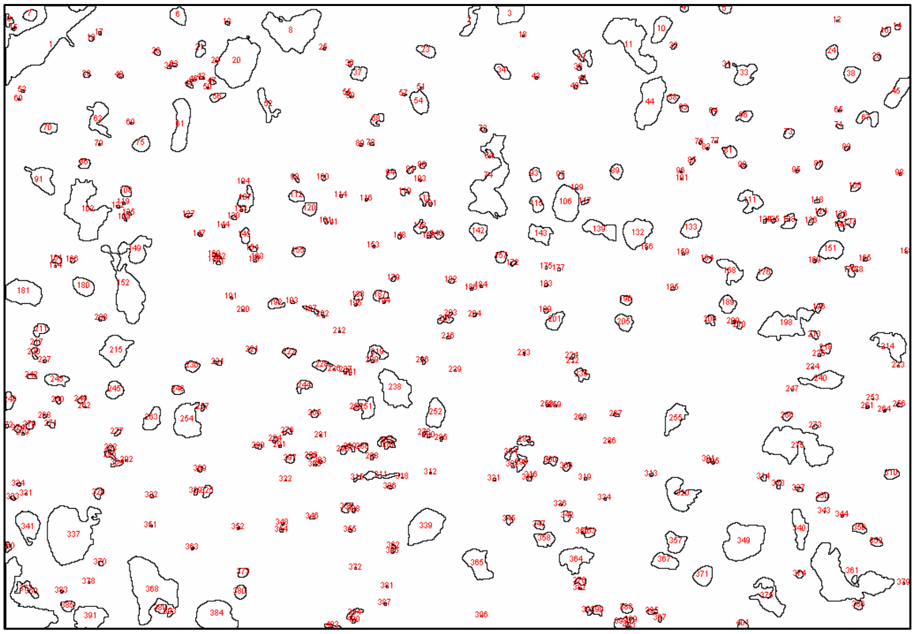

Figure 25 Pore identification of Ti-A from polished binary mask

The titanium samples were prepared in the same manner as the previous samples, capturing the pores structure in a low-viscosity epoxy before grinding and polishing the sample as described in the previous chapter. Image analysis resulted in a 6.25% porosity from Figure 24 and Figure 25 with an average pore size of 0.158% of total area and a standard deviation of 0.45%. The pore structure is mapped from several areas and shown here as a representative of the process, the pores show a variability in sizing with smooth transitions and limited sharp corners as seen in Figure 25. The morphology shows evidence of larger pores being formed by the amalgamation of smaller pores, this has been shown to be a failure mechanism when the material is subjected to stress.

4.2.5 Titanium B

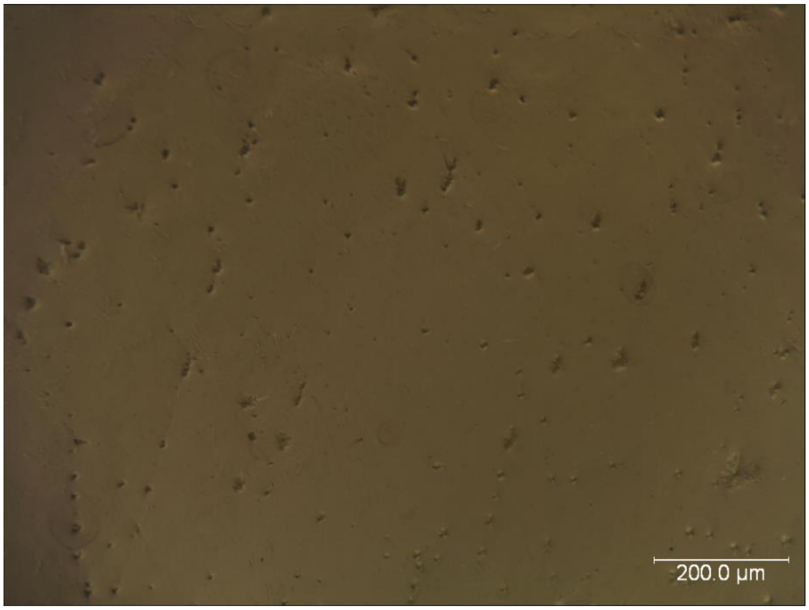

Figure 26 Ti B polished sample 100X Magnification

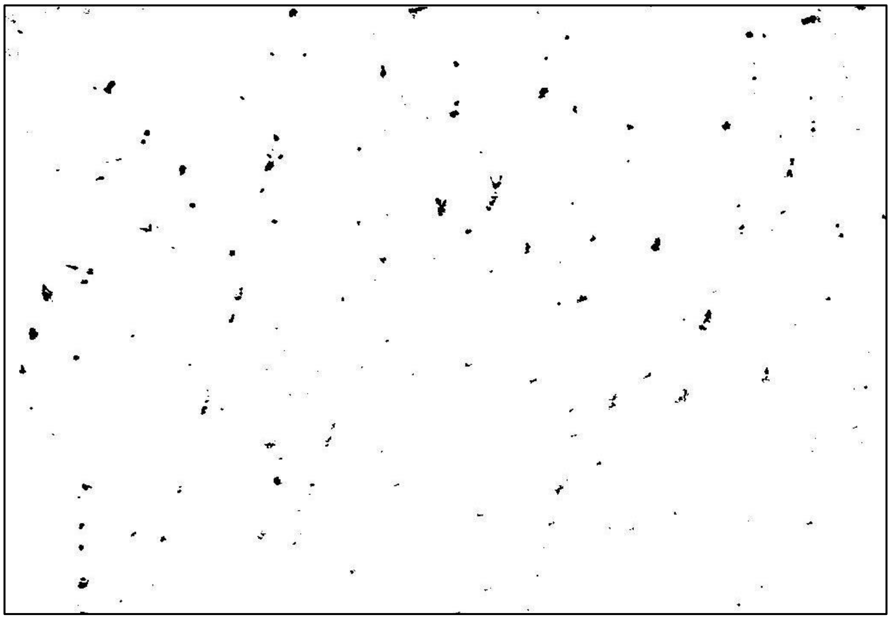

Figure 27 Binary Image produced from polished optical image.

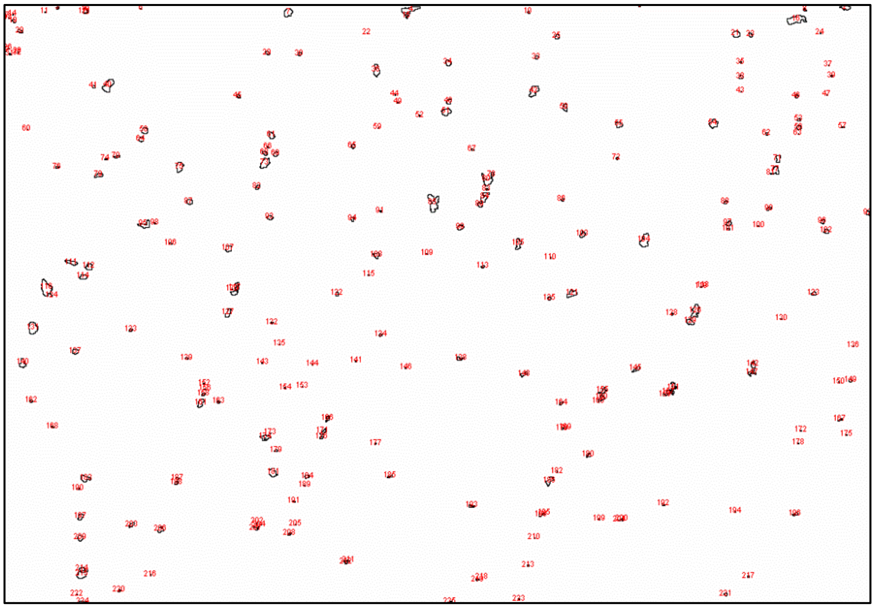

Figure 28 Results from computer generated pore analysis Ti B

The porosity determined from image analysis techniques of Figure 26 and Figure 27 is 0.246% with an average percent area of the pores is 0.0028% and a standard deviation of 0.0038%. The pore structure is small in comparison to all the other tested materials with a random distribution through the entire material revealed in Figure 28. This was the lowest porosity measured in all the samples and resulting with the highest mechanical properties as well as the only material that met or exceeded the reference material.

The Titanium materials were produced by different methods and the resultant pore structure is minimized in the Ti-B sample made through additive manufacturing. The method does not rely on the sintering concepts presented in chapter 2, instead a stream of superheated plasma is used as a build medium. This method produces a lower porosity as shown in the findings when compared to all the tested materials.

4.3 Hardness

This section represents the apparent density measurements of all the test materials measured according to ASTM – E18. All values are reported in HRB scale and the testing was conducted on tensile test bars in the as-received condition the test sites were moved along the face of the tensile sample to ensure a minimum length between the previous indentation.

4.3.1 FC0205

Table 12 presents the results of the hardness testing of FC0205 where a tensile test bar was used due to the parallel sides of the material to limit any artificial influence on the test results. The data shows a good correlation with only one test result below 70 HRB, the overall average is 73.34 ± 2.73 HRB with only the titanium samples had superior hardness results.

Table 12 Results of Hardness testing for FC0205 results shown in HRB scale.

FC-0205	Avg	St. dev
74.1	73.34	2.73
72.4		
76.2		
73.6		
74.1		
74.3		
76.6		
66.7		
72.2		
73.2		

4.3.2 Aluminum Alloy A

The hardness of Al-A was 51.01 ±1.35 HRB with little variation between the test sites according to Table 13 this was slightly lower that Al-B test results and can be related back to the difference in porosity of the samples. The experimental density of Al-B was higher than that of Al-A and would result in a higher apparent hardness due to the limit number of pores that the hardness test would engage.

Table 13 Hardness data results for Aluminum A samples in HRB

Al-A	Avg.	Stdev
51.7	51.01	1.35
51.7		
49.3		
48.9		
50		
50.5		
51.9		
51.4		
53.4		
51.3		

4.3.3 Aluminum Alloy B

The hardness of Al-B was 62.01 ±3.27 HRB with little variation between the test sites according ranging from 54.8 to 65.7 as shown in Table 14. Due to the lower porosity of the Al-B test material when comparted to the Al-A samples that were produced in a similar method the hardness of the Al-B samples was higher by approximately 21%. The Al-B sample has approximately 6% higher density that the Al-A sample and shows a good correlation between increased hardness and increased density.

Table 14 Tabulated hardness results from testing of Aluminum B samples in HRB.

Al-B	Avg.	Stdev
64.9	62.01	3.27
61.8		
62.9		
54.8		
58.9		
64.2		
64.3		
65.7		
61.8		
60.8		

4.3.4 Titanium A

The variability in test results is low for Ti-A titanium with an average of 79.36 ± 091 HRB, the standard deviation of the values indicates a good agreement between the test sites and no anomaly's that might have been found if a sub-surface pore was present during the testing. The relative size difference between the pore and the indenter would negate any erroneous readings as well as long as the indenter is sufficiently larger than the average pore size.

Table 15 Hardness values collected during testing of Titanium Al Samples in HRB.

Ti-A	Avg	Stdev
79.3	79.36	0.91
78.9		
80.4		
79.5		
80.2		
80.7		
79		
78.1		
79.5		
78		

4.3.5 Titanium B

Table 16 Hardness testing results of Titanium B values reported in HRB.

Ti-B	Avg	Stdev
94.1	95.69	0.90
95.6		
96		
96.5		
97.1		
95.2		
94.9		
95.1		
95.8		
96.6		

As expected the Ti-B sample exhibits the highest hardness at 96.69 ± 0.90 HRB due to the lowest porosity found through both image analysis and when comparing densities. Although a fair comparison would be between the Ti-A samples as they have similar elemental composition the hardness of the Ti-A samples is still higher than the reference material. The reference material having a high porosity when compared to all the other test samples it would be expected to have similarly poor mechanical properties. The inclusion of the secondary phases found in both the FC0205 and Ti-B seem to have a positive influence on the mechanical properties of the materials.

4.4 Elemental Composition and Microstructure

This section presents the results obtained during elemental composition experiments including X-ray diffraction and optical spectroscopy as well as microstructure observations from SEM and optical micrographs.

4.4.1 FC0205

The FC0205 samples were prepared for optical and SEM observations by mounting the samples in a cold mount epoxy and following the grinding and polishing steps outined in chapter three. After the polishing steps were completed the sample was etched using a Nital solution to reveal the grain structure. The elemental composition was obtained from a published standard [39].

Table 17 Elemental Composition of FC0205, data collected from MPIF Standard 35 [39]

Carbon %	Copper %	Iron %
0.3 – 0.6	1.5 -3.9	Balance

Table 17 is comprised of the accepted standard for composition of FC0205 and was not independently tested to verify the actual content during the presented research as no pertinent information would be gained.

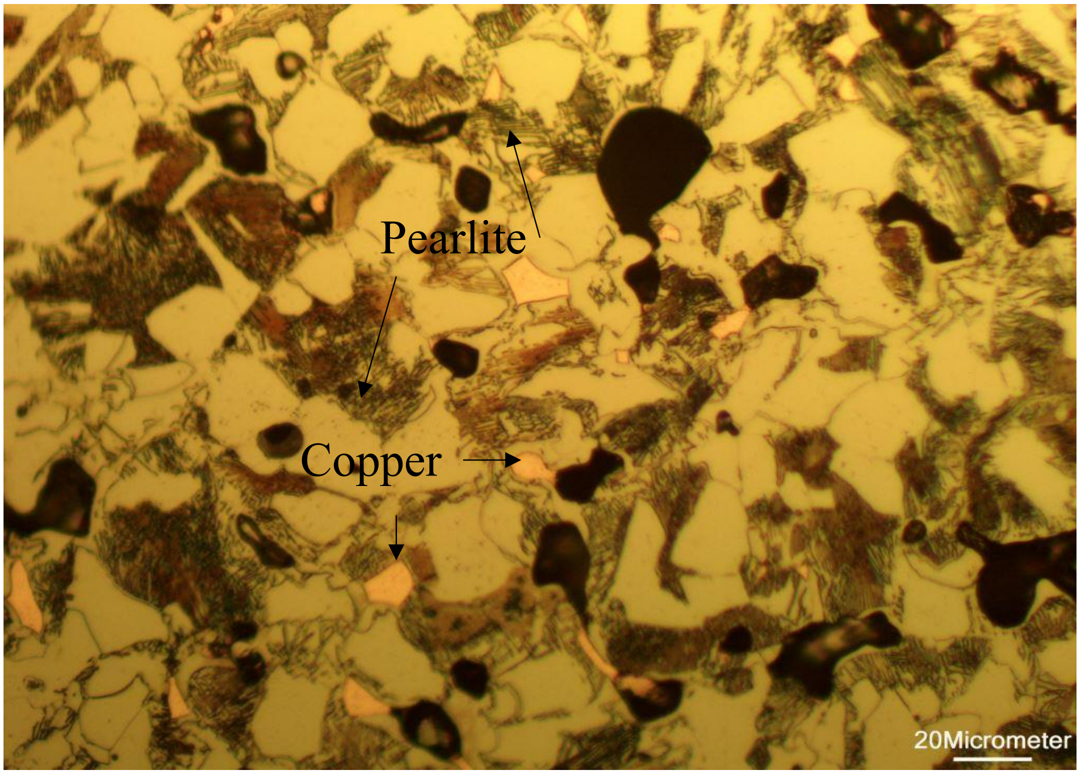

Figure 29 FC0205 Etched sample showing copper rich regions and pearlite phases 400X Magnification.

The copper content exceeded 2% wt. in the FC0205 and this is evident by the second phase of pure copper that can be seen in the microstructure in Figure 29, 2% is the limit for copper in solution with the Fe-C system. Pearlite structure is evident in the FC0205 recognizable from the lamellar structure and equiaxed grain structure that develops as a result of the grain structure formed from the liquid phase sintering [1],[4]-[5].

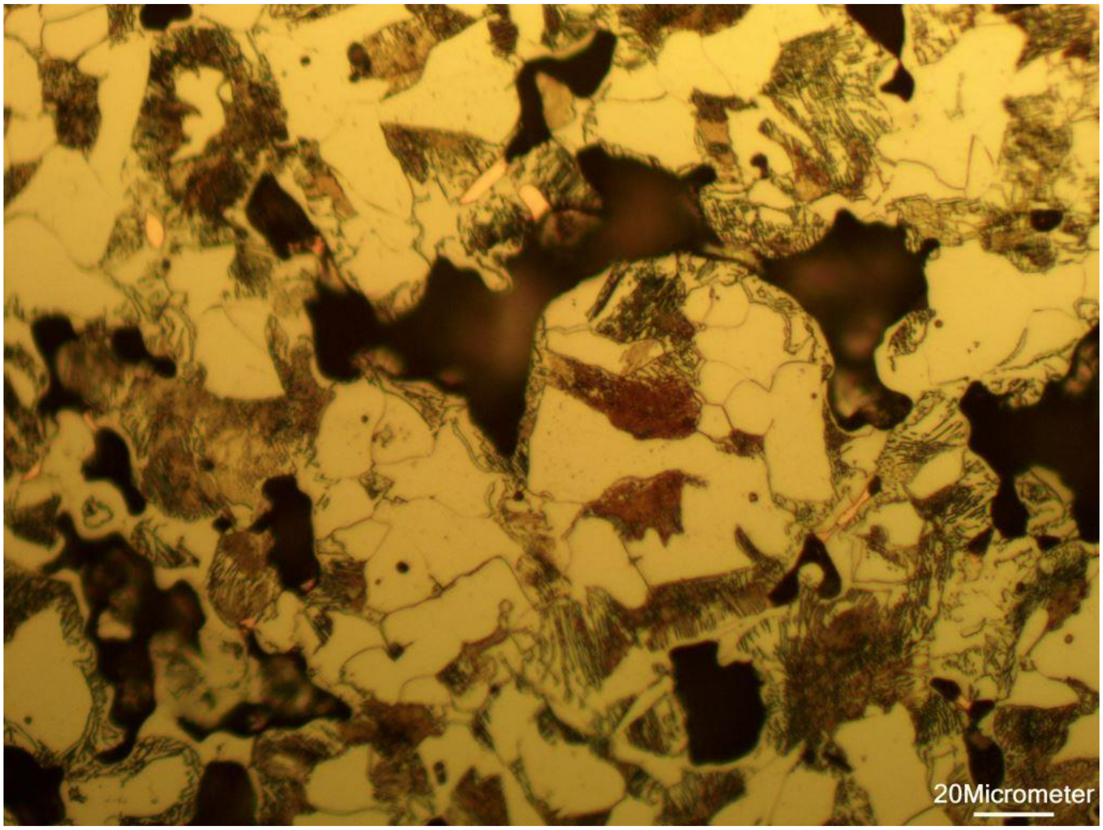

Figure 30 Etched sample of FC0205 centered over a pore structure 400X Magnification.

Figure 30 shows a magnified view of the pore structure within the FC0205 shows a combination of irregularly shaped grains and interconnectivity between the pores present in the micrograph. The large pore presented in the center of the image is a combination of smaller pores that have accumulated to form a large, irregularly shape pore.

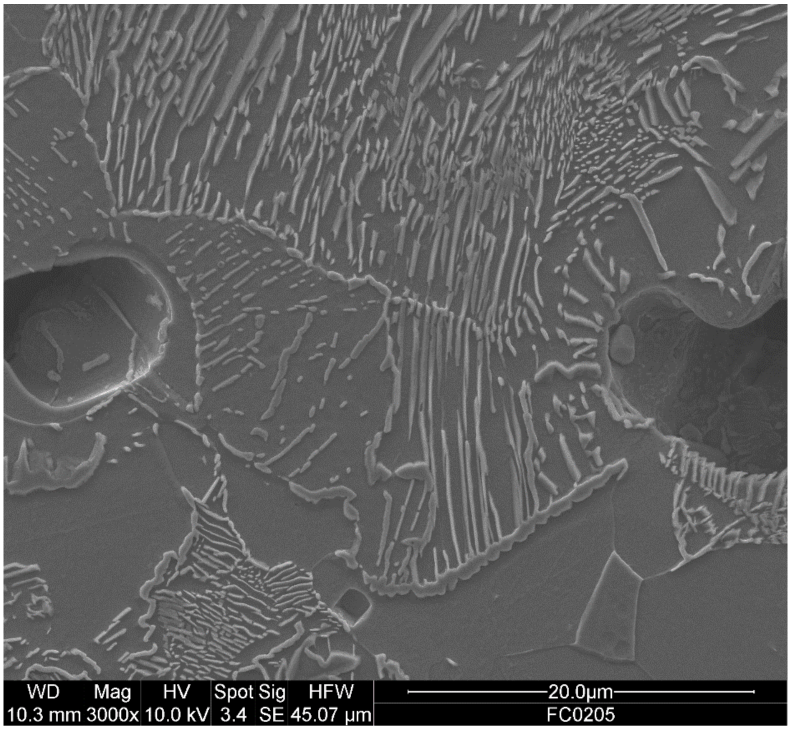

Figure 31 Magnification of grain and pore interface from of FC0205 ***Error! Reference source not found.***

Although the porosity of the FC0205 materials was found to be higher than the other materials the range of microstructural features and secondary phases found within the copper steel is directly related higher strengths that have been found during testing. The pearlite structure shown in Figure 31 appears to extend into the pore structure. The secondary phases are primarily responsible for the increase in mechanical properties of the FC0205 material as they aid in crack blunting, crack arresting as well as allowing for a higher load to be carried by the reduced cross section as stated by Drar et al [36]. Based on the porosity alone the reference material would have the worst fatigue and tensile strengths.

4.4.2 Aluminum Alloy A

The aluminum alloy A was mounted in a cold set epoxy under vacuum, after the sample was removed from the epoxy it was then ground and polished according to the strategy established in chapter three. After the sample was sufficiently polished a solution of Keller's etch was applied to the surface for a sufficient amount of time to reveal the grain structure but not long enough to over etch and artificially change the structure. The sample was then observed under a stereo microscope and images were taken to examine the grain structure.

Figure 32 Polished and etched (Keller's) sample of Al- A

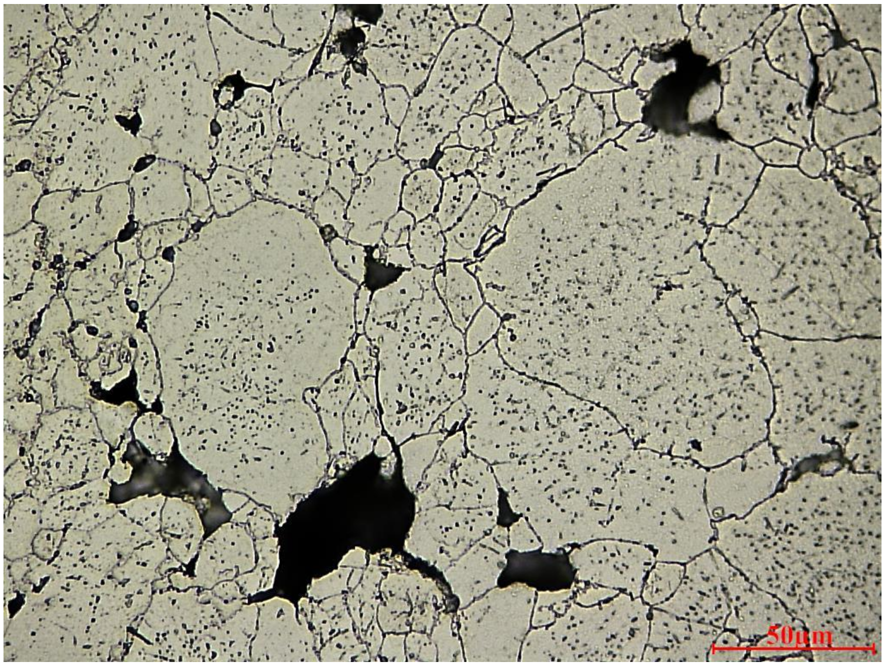

Figure 33 Magnified view of pore and grain structure of Al A samples

The etched micrograph samples in Figure 32 and Figure 33 show a variety of grain sizing, the pores have some degree of interconnectivity along the grain boundaries. Comparing grains between the two aluminum samples, the grains visible in Figure 32 are smaller in size than the grains visible in Figure 36. Upon further investigation under SEM as in Figure 34, the inclusions are seen within the grain boundaries are actually micro voids that have formed during the sintering process. The micro voids would also degrade the mechanical properties of this material through linking and decreasing the cross-sectional area that would be available to bear the loading condition.

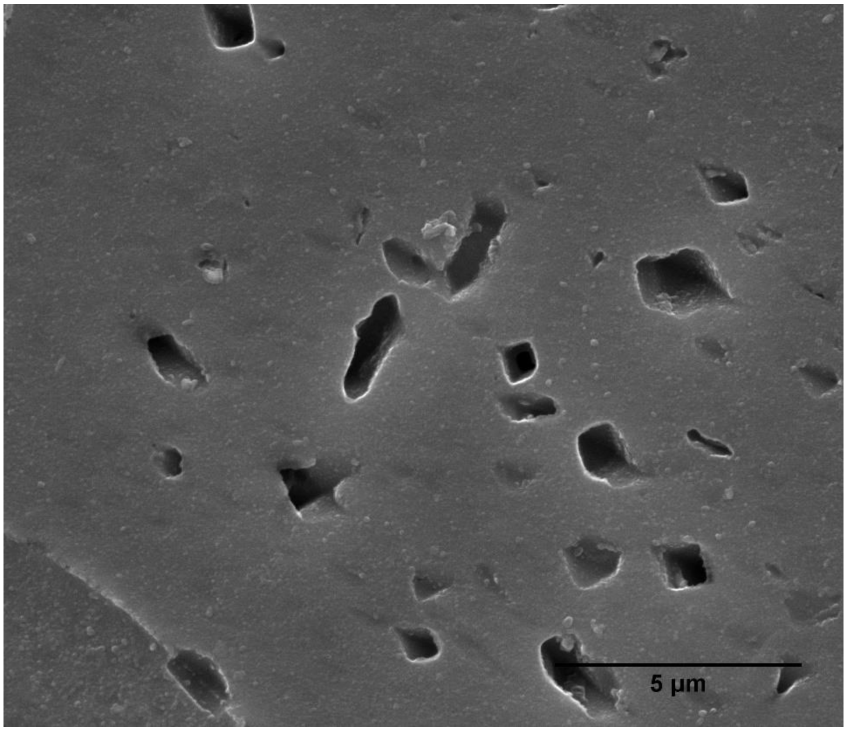

Figure 34 SEM image of Al A sample with indication of EDS sample spot.

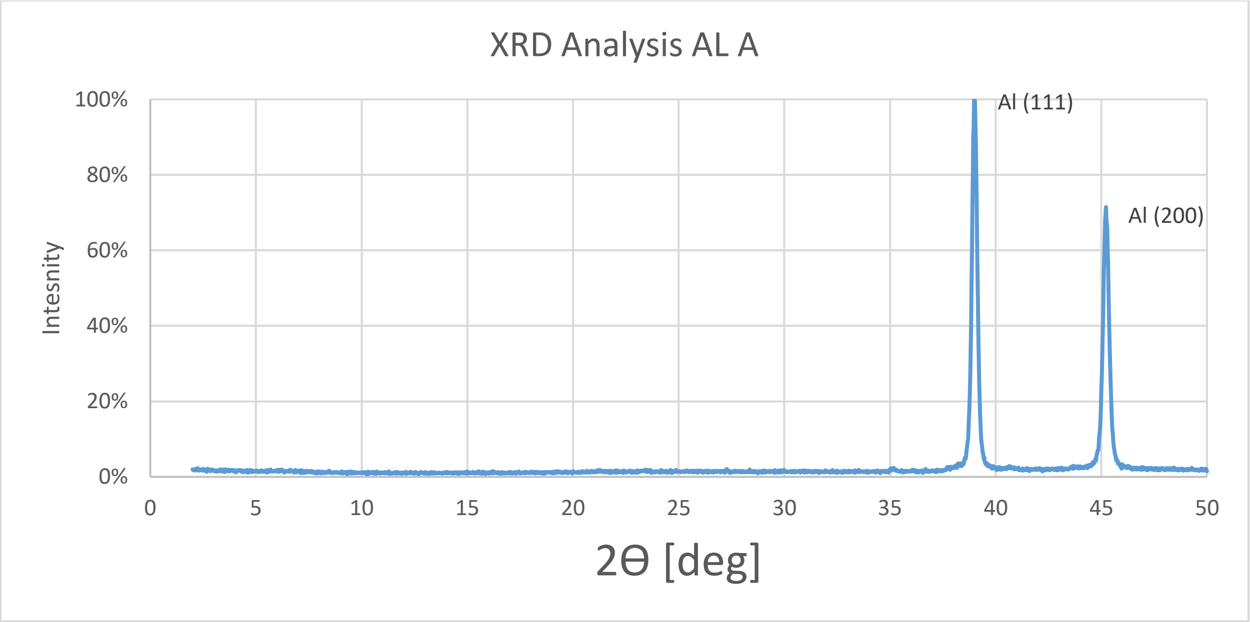

Figure 35 XRD data of Al A sample

XRD analysis of the sample shows consistency with bulk aluminum matrix with a lattice parameter of 0.400 nm. Evidence of a $CuAl_2$ crystal structure and silicon structure were found through XRD which was consistent with ICP-OES sampling [9]-[11]. Although no visible evidence was found of precipitates in the material, it is possible that they were not large enough to be observed.

Table 18 is the results of analysis of the peaks found by applying Bragg's Law Equation (2) and (3) to find the lattice parameter and inter-planar spacing of the elements. The table list the expected elements along with the Bravais index that would be associated with the crystal structure. The diffraction test did not extend the diffraction rays past the 50° angle which would make the classification of the crystal structures based on insufficient data to make an assertion to the crystal structure.

Table 18 Inter-planar spacing table from XRD data and Bragg's Law of Al- A

Peak	2Θ	$\sin\Theta$	$\sin^2\Theta$	$\sin^2\Theta/\sin^2\Theta_{min}=(h^2+k^2+l^2)/$	$\sin^2\Theta/\sin^2\Theta_{min*}(h^2+k^2+l^2)_{min}$	$h^2+l^2+k^2$	h	k	l	$d_{hkl}=l/2*\sin\Theta$	lattice parameter	
1	23.42	0.202958	0.04119	1	1	1	1	0	0	0.379832	0.379831908	
2	35.18	0.302204	0.09133	2.217102877	2.217102877	2	0	0	2	0.255093	0.510185978	Mg (1 0 1)
3	39	0.333807	0.11143	2.705062555	3	3	1	1	1	0.230942	0.400003155	Al (1 1 1)
4	40.64	0.347263	0.12059	2.927546917	2	2	1	0	1	0.221993	0.31394568	Si (1 0 1)
5	45.22	0.384456	0.14781	3.588236806	3.9794682	4	2	0	0	0.200517	0.401033722	Al (2 0 0)

Due to the limitations of the XRD analysis and the inability to identify any precipitates in the aluminum structure the material was studied using an inductively conductive plasma optical emission spectroscopy by digesting a sample of the material in a solution of hydrogen fluoride and nitric acid, the exact process was covered in chapter three. The results of the elemental composition are presented in Table 19.

Table 19 Elemental Composition determined from ICP-OES

	Element wt%				
	Al	Cu	Mg	Ti	Si
Al - A	82.74	11.28	2.30	2.01	1.07

The composition of the tested samples is inline with the composition of a 2XXX series alloy, the tested samples shows an elevated weight percent of copper that may be due to the sample preparation, the composition of the powder used to produce the material.

4.4.3 Aluminum Alloy B

The general procedure was followed of sample preparation outline in chapter three, with the addition of etching the surface Keller's etchant, an acid solution. This revealed the grain structure that is visible in Figure 36.

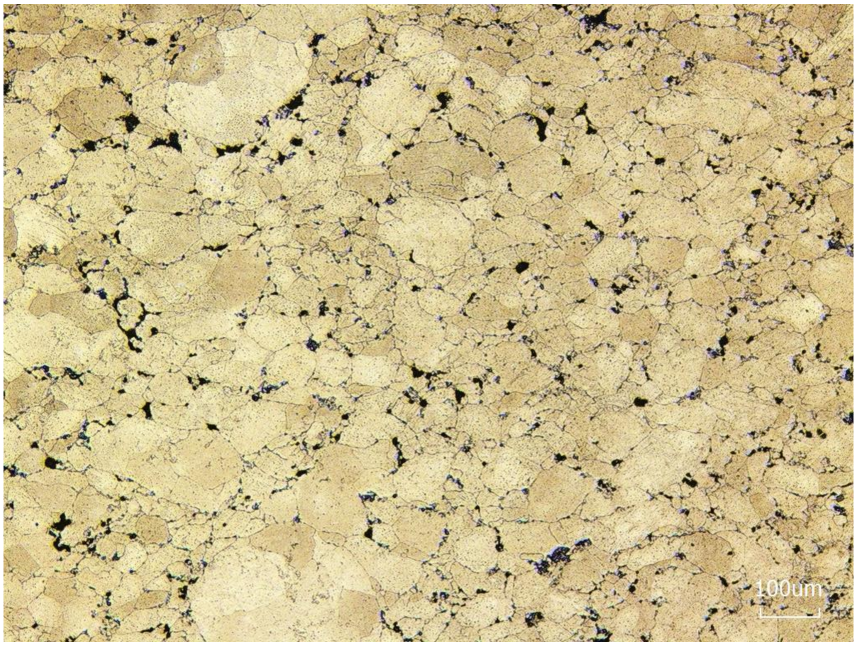

Figure 36 Etched by Keller's etchant showing grain definition of Al-B.

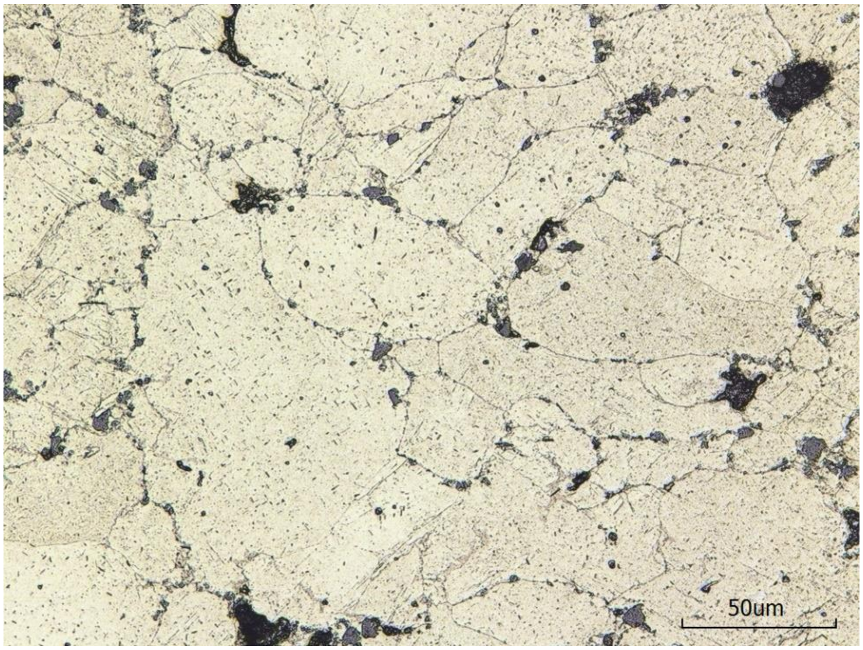

Figure 37 A magnified view of grain boundaries of AL-B sample.

In Figure 36 and Figure 37, the grain structure is less varied than that of the Al-A sample, with less evidence of larger pores that is consistent with the porosity found through image analysis. The optical micrographs also show similar micro voids in the interior of the grain structure that are highlighted in Figure 38, as well as secondary phase accumulated along the grain boundaries [10]-[12].

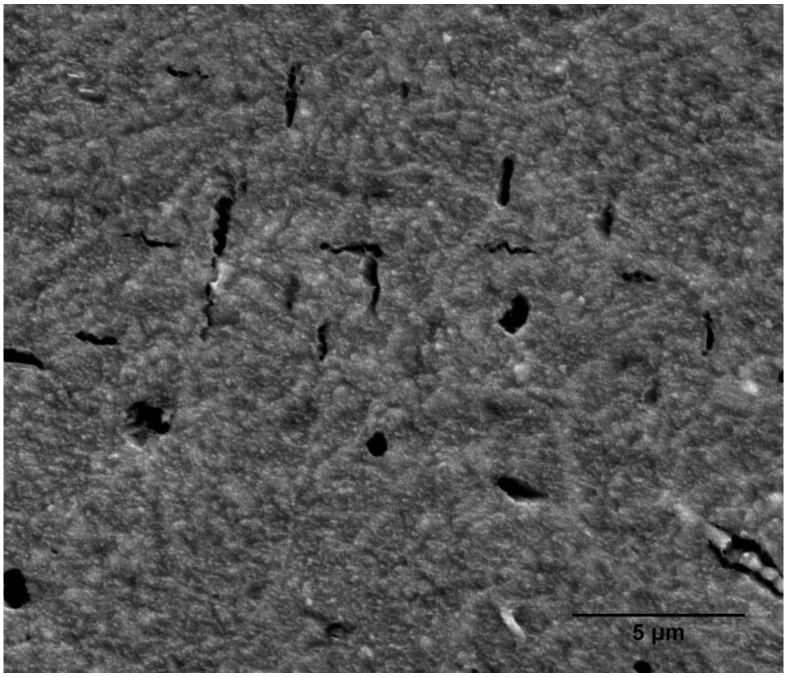

Figure 38 SEM image of Al –B showing micro voids within the grain interior

Crystallography of the sample was investigated by X-ray diffraction of the sample conducted at the University of Western Ontario lab for chemistry. The peaks that are visible in Figure 40 were used in Bragg's law equations (2) and (3) to determine the interplanar spacing and lattice parameter associated with the crystal planes. The peaks labeled in Figure 40 are only that of the aluminum as with the range of diffraction angles was not wide enough to gather sufficient data to make a confident assessment.

Figure 39 EDS mapping results from figure 48

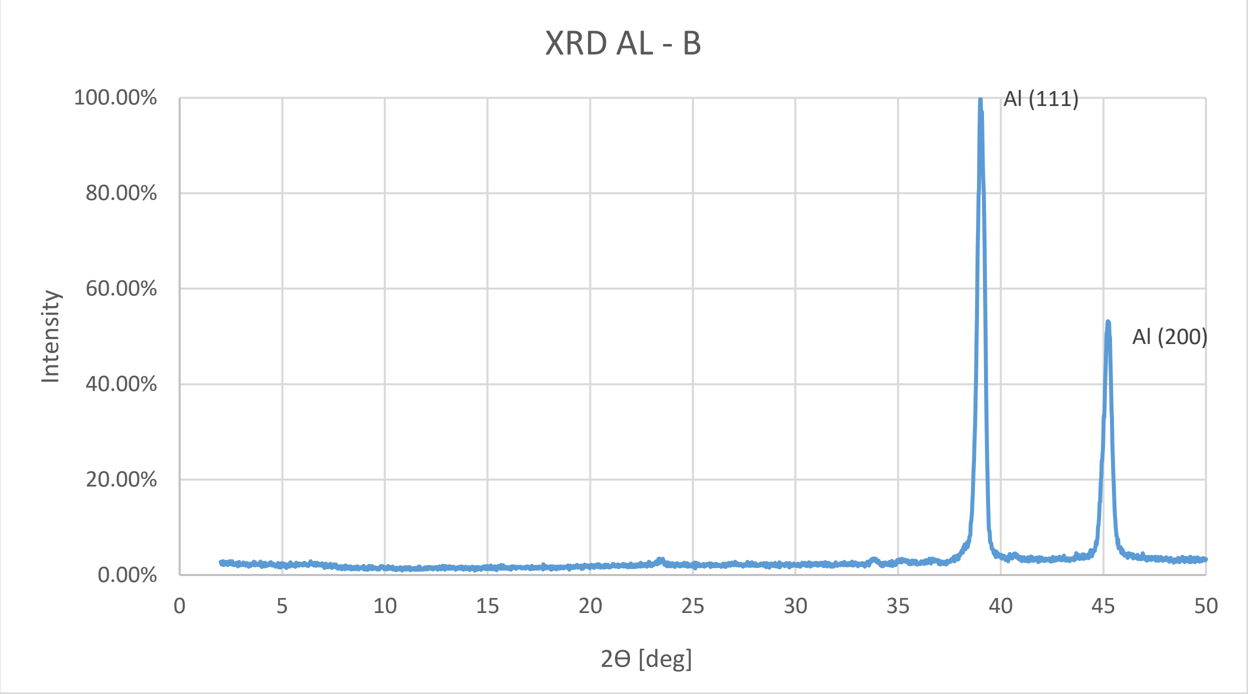

Figure 40 XRD Data for Al B sample

Table 20 preliminary inter-planar spacing determination from XRD Data

Peak	2Θ	sinΘ	$\sin^2\Theta$	$\sin^2\Theta/\sin^2\Theta_{min}=(h^2+k^2+l^2)/$	$\sin^2\Theta/\sin^2\Theta_{min*}(h^2+k^2+l^2)_{min}$	$h^2+l^2+k^2$	h	k	l	$d_{hkl}=l/2*\sin\Theta$	lattice parameter	Phase and plane
1	23.38	0.202616	0.04105	1	1	1	1	0	0	0.380473	0.380472684	
2	33.82	0.290869	0.0846	2.060849604	2.060849604	2	1	0	1	0.265033	0.374813591	Mg(1 0 1)
4	39.02	0.333971	0.11154	2.716873165	2.716873165	3	1	1	1	0.230828	0.39980611	Al (1 1 1)
6	45.22	0.384456	0.14781	3.600353708	3.600353708	4	2	0	0	0.200517	0.401033722	Al(2 0 0)

Table 21 Elemental composition determined from ICP-OES

	Element wt%				
Al -B	Al	Cu	Mg	Ti	Si
	64.07	28.13	5.43	1.06	0.65

The elemental composition determined by ICP-OES shows a high weight percent of copper over what would be expected from a 2XXX series alloy that has a maximum of 6 wt%, this could be from the dissolved samples having a high copper content over and above the general chemistry of the sample or the copper was added in this quantity by the producer. The copper was difficult to decipher from the XRD as copper and the compounds form with aluminum share similar diffraction peaks as aluminum. The chemical composition nor processing parameters was not disclosed.

4.4.4 Titanium A

After mounting and polishing the sample the titanium samples were etched with Kroll’s etchant to reveal the grain structure, optical images were taken as represented in Figure 41as well SEM images Figure 42 Figure 43.

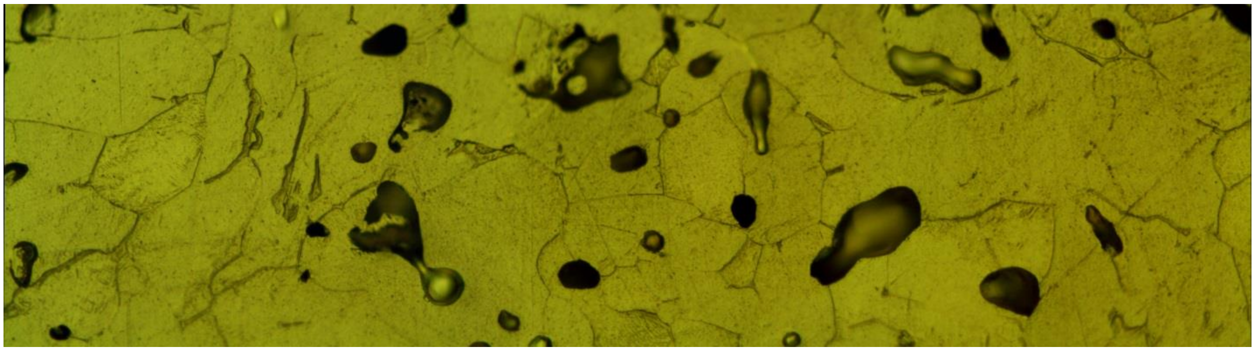

Figure 41 Ti A etched sample at 500X Magnification

Figure 41 shows a uniform flake-like grain structure with pores forming within grains and the pores have a smooth rounded appearance.

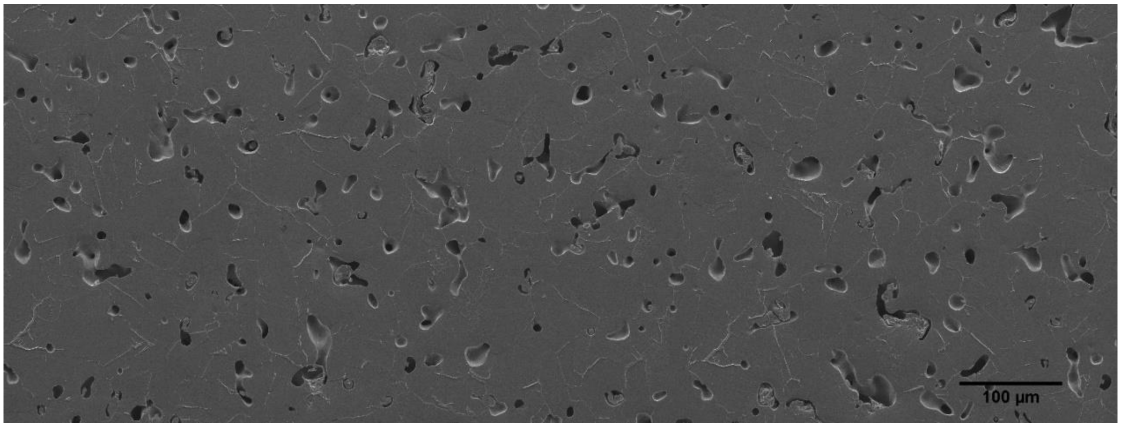

Figure 42 Composite SEM image of Ti A at 200X Magnification

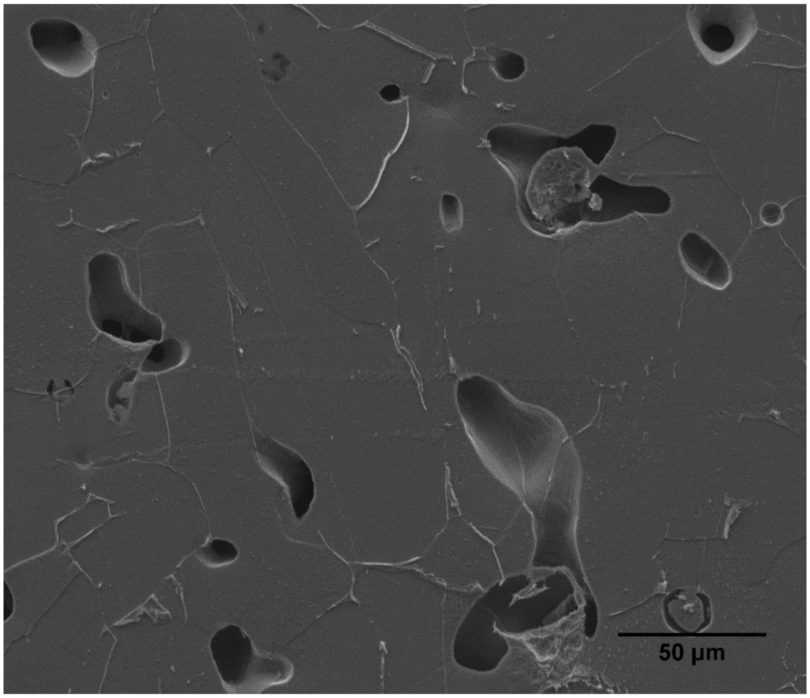

Figure 43 SEM Image of Grain and pore interface

SEM imaging reveals the pores are well dispersed throughout the structure with a majority of the pores having smooth edges shown in Figure 42. A pore with a cap is visible in the upper right corner of Figure 43 and this is a main reason for the vacuum impregnating during the mounting process to ensure that pores of this nature are not disturbed or altered by the preparation process.

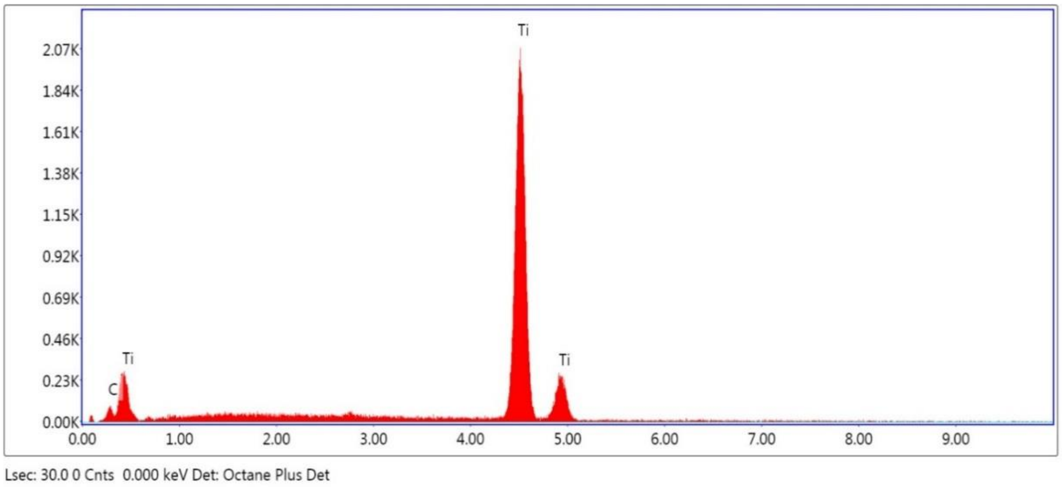

Figure 44 EDS data from bulk phase of Ti A

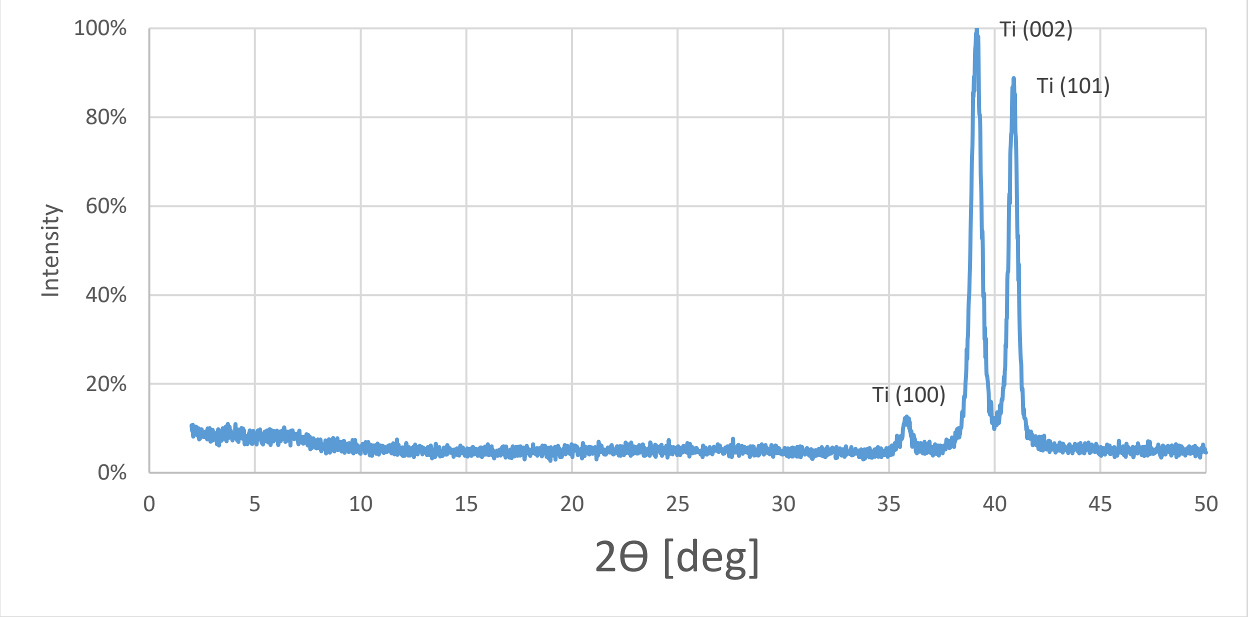

Figure 45 XRD data of TI A sample

The XRD crystallography examination displays definite peaks that are consistent with hexagonal structure of titanium with a c/a value of 1.64415, there is also indication from the XRD analysis that Ti may be present with a c/a value of 1.5878 [7,8].

Table 22 Elemental composition determined from ICP-OES

	Element wt%				
Ti -A	Ti	Si	Fe	Co	V
	99.03	0.32	0.24	0.18	0.11

The ICP-OES and EDS mapping conducted on the samples showed similar results have a pure elemental composition of titanium, the carbon peak in Figure 44 is from a carbon coating applied during the SEM session to promote electron discharging. The XRD peaks shown in Figure 45 are consistent with a titanium sample.

Table 23 Preliminary Inter-planar spacing table from XRD data and Bragg's Law of Ti A

Peak	2Θ	sinΘ	$\sin^2\Theta$	$\sin^2\Theta/\sin^2\Theta_{min}=(h^2+k^2+l^2)/$	$\sin^2\Theta/\sin^2\Theta_{min^*}(h^2+k^2+l^2)_{min}$	$h^2+l^2+k^2$	h	k	l	$d_{hkl}=l\ /2$ *sinΘ	lattice parameter	Average Lattice Parameter
1	35.84	0.307689	0.09467	1	3	3	1	1	1	0.250545	0.433957331	HCP Ti
2	39.16	0.335123	0.11231	1.186272412	3.558817235					0.230035	0	
3	40.9	0.34939	0.12207	1.289428531	3.868285594	4	2	0	0	0.220642	0.441283572	

4.4.5 Titanium B

The additive manufactured titanium was etched with Kroll's etch after the grinding and polishing was completed. Figure 46 shows the structure revealed after etching, the grains appear to be elongated and with varying size and configuration. Figure 47 is an SEM micrograph that reveals clusters of a second phase inclusion disperse throughout the grain structure, the grain structure under SEM irregularly shaped.

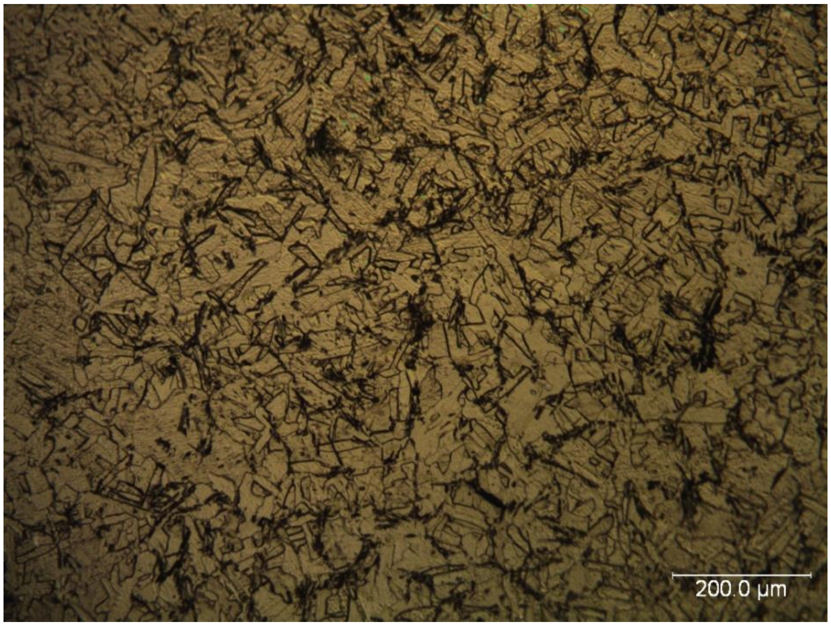

Figure 46 micrograph of pre-etched Ti-B

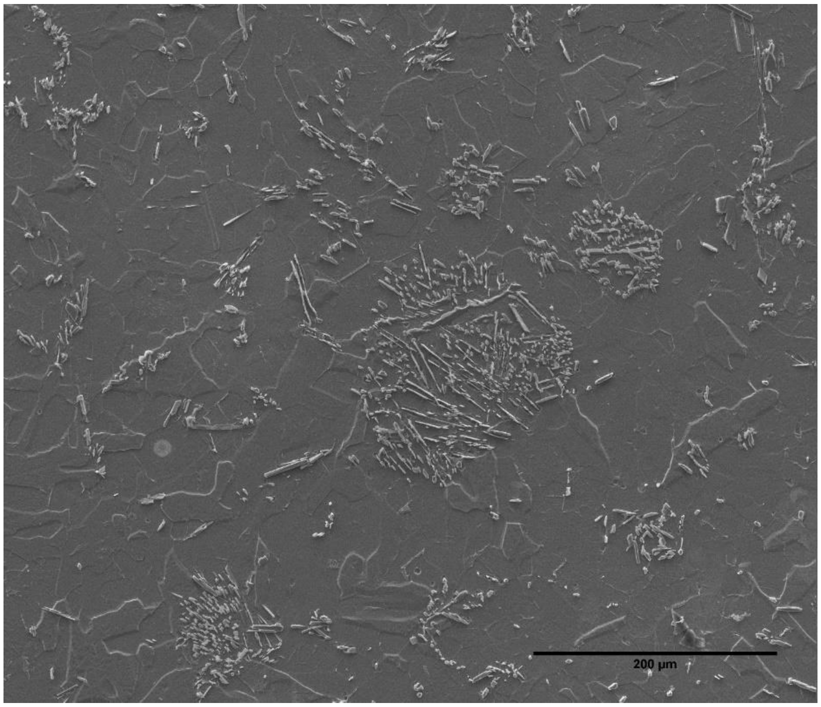

Figure 47 SEM Image of Ti B grain structure with a secondary phase of fibroid structure

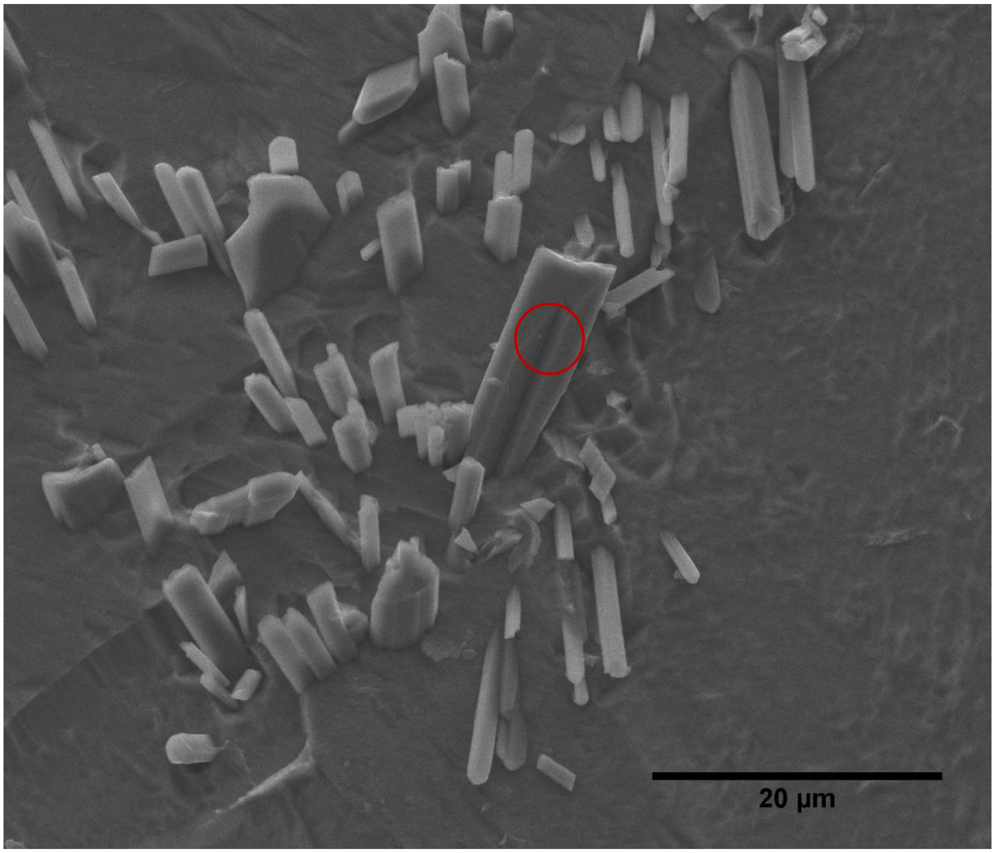

Figure 48 SEM Image of fibroid structure found within the sample, circle represents EDS spot analysis of the polished and etched surface,

Figure 48 is an SEM image that shows a dispersion of fibroid structures dispersed in the bulk matrix, with the following EDS data from sample location indicated as a red dot and the subsequent EDS results presented in Figure 49. The structures were evident throughout the material at various locations in a random manner.

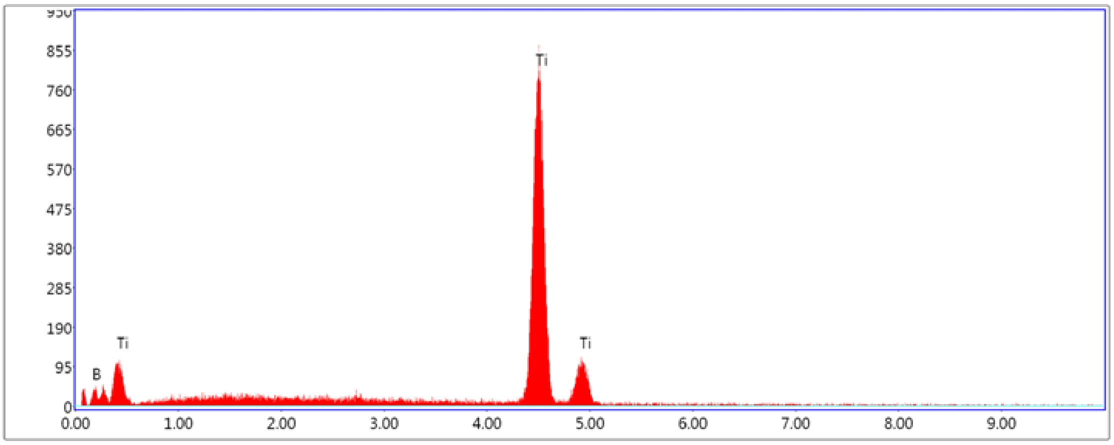

Figure 49 Results of EDX from Figure 48

The structures found within the material are a second phase intermetallic of titanium and boron, the two possible candidates are TiB and TiB_2. The intermetallic was confirmed to be TiB from the characteristic structure compared to similar results found by other researchers. TiB was further confirmed from SAED during the TEM sessions that was conducted near the end of the research. Similar structures were presented by other research such as Zhang et al. [52] the found a correlation to the cooling rate of the composite with the distribution of the included intermetallic. The process of fabricating this material is most likely the cause of formation of these formations to due the thermal cycling during the build process.

Table 24 Elemental composition determined from ICP-OES

	Element wt%				
	Ti	Al	B	Si	Fe
Ti - B	97.3	0.82	0.63	0.37	0.2

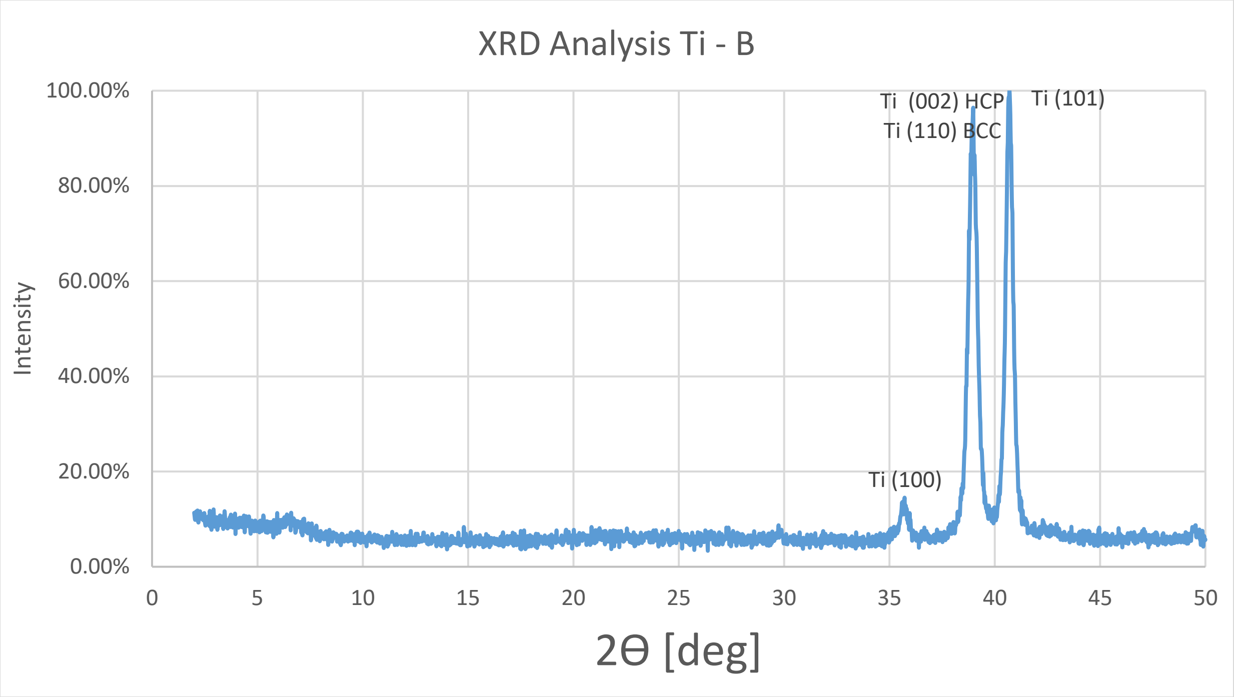

Figure 50 XRD Analysis of Ti B Sample

Analysis of the XRD data along with the EDX results it can be determined that the sample is a grade of commercially pure titanium. The XRD data shows peaks that are consistent hexagonal closed packed crystal structure titanium. There is a possibility that a body centered cubic structured may have been formed due to the high temperature processing of the plasma transferred arc however the peaks of the XRD data overlap with both structures in the tested range of angles [7]-[8].

Table 25 Inter-planar spacing table from XRD data and Bragg's Law of Ti A

Peak	2ϴ	sinϴ	$\sin^2\Theta$	$\sin^2\Theta/\sin^2\Theta_{min}=(h^2+k^2+l^2)/(h^2+k^2+l^2)_{min}$	$\sin^2\Theta/\sin^2\Theta_{min*}(h^2+k^2+l^2)_{min}$	$h^2+l^2+k^2$	h	k	l	d_{hkl}=l /2 *sinϴ	lattice parameter	
1	35.72	0.306692	0.09406	1	3	3	1	1	1	0.25136	0.435367429	HCP Ti
2	38.98	0.333642	0.111317	1.183468823	3.550406469					0.231056	0	
3	40.7	0.347754	0.120933	1.285697347	3.857092042	4	2	0	0	0.22168	0.443359409	

4.5 Tensile Testing

This section shows the results from the tensile testing of the tested materials according to ASTM E8 (MPIF 10). The tensile samples were machined by the respective suppliers and were testing in the as received condition. Tensile testing was conducting using an extensimeter attached to the test samples. Before testing the test, samples were measured using a set of calibrated calibers at three separate locations for both the width and thickness along the gauge length, the results were averaged and that value was used for the cross-sectional area measurement.

4.5.1 FC0205

The reference material was tested three times on the MTS criterion universal test machine with a crosshead speed of 0.05mm/min, the graph of the tensile test is presented below in Figure 51.

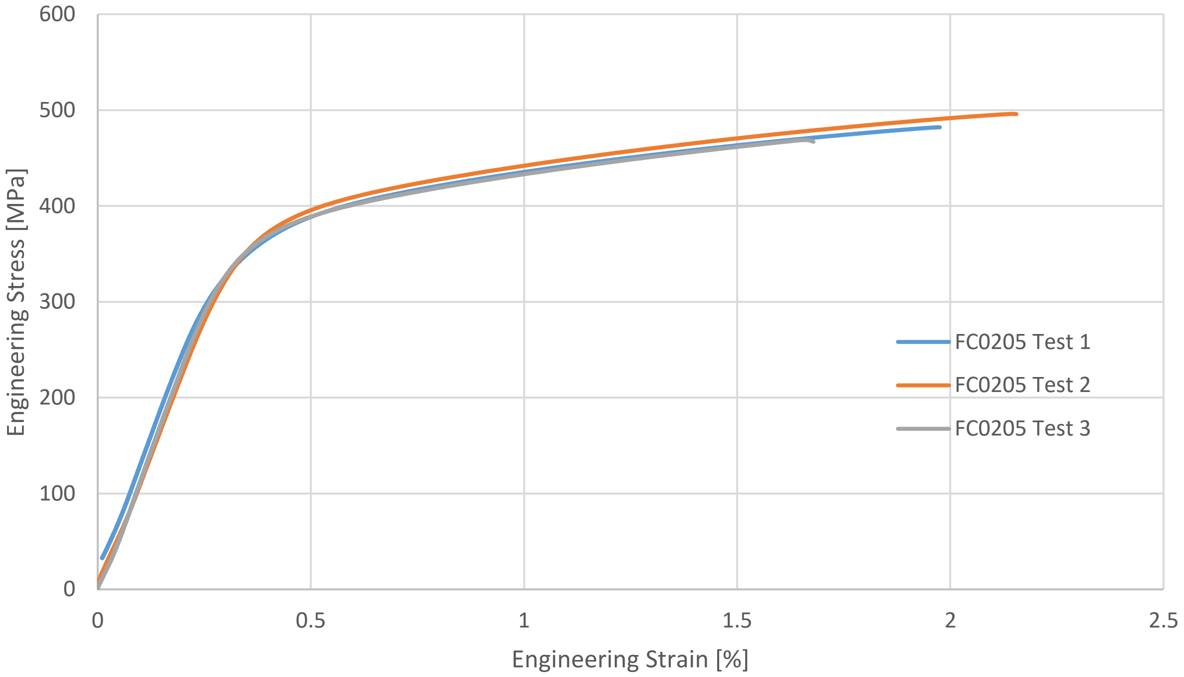

Figure 51 Tensile test results of the FC-0205 samples

The Tensile test results of the three samples show consistency between all samples with only slight variation in the strain at rupture.

Table 26 Tabulated results from the tensile test of FC0205

	Ultimate Tensile Strength MPa	Std. Deviation	Yield Strength MPa	Std. Deviation	Tensile Elongation, %	Std. Deviation
PM-FC0205	482.32	13.59	393.40	5.77	1.92	0.24

The results of the tensile tests in Table 26 are consistent with accepted data for this particular alloy with an ultimate tensile strength of 482.32 MPa and a yield strength of 393.40 MPa the variation between measurements is small [39].

4.5.2 Aluminum Alloy A

The cold press and sintered aluminum sample Al-A was tested using the MTS Criterion universal testing machine, the data from the extensometer was used to calculate the strain of the material. Two tests were performed with a crosshead speed of 0.05mm/min, the elastic region showed similar results with slightly different yield strength and ultimate tensile strengths as visible in Figure 52 Tensile test results for al-A samples.

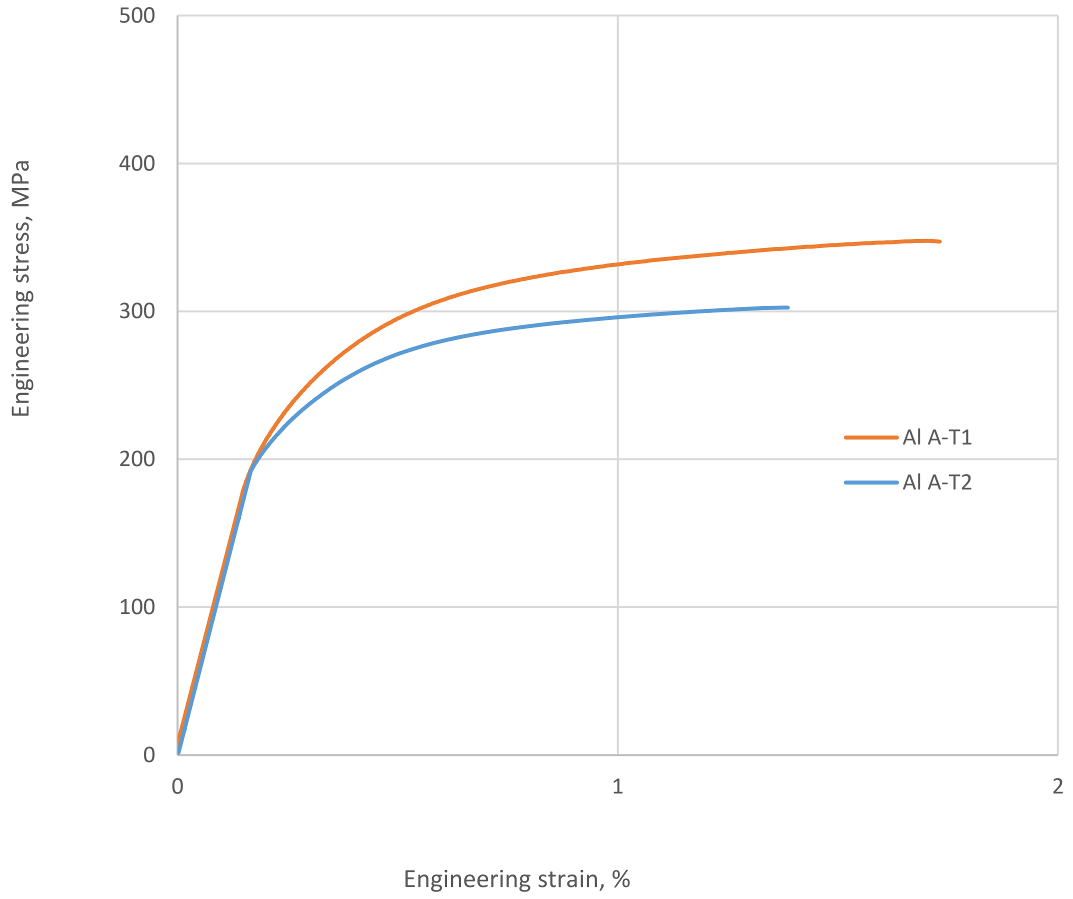

Figure 52 Tensile test results for al-A samples.

The ultimate tensile strength of the material is averaged from the tensile test with a UTS of 325.10 MPa and yield strength of 285.00 MPa. The elongation of the sample was lower than that of the Al -B sample.

Table 27 Compiled data from the tensile testing of aluminum samples from A

	Ultimate Tensile Strength MPa	**Std. Deviation**	**Yield Strength MPa**	**Std. Deviation**	**Tensile Elongation %**	**Std. Deviation**
Al - A	325.10	31.91	285.00	2.92	2.02	0.40

4.5.3 Aluminum Alloy B

The cold press and sintered aluminum material underwent tensile testing using the MTS criterion universal test machine. Two tests were performed on the material with a crosshead speed of 0.05 mm/min.

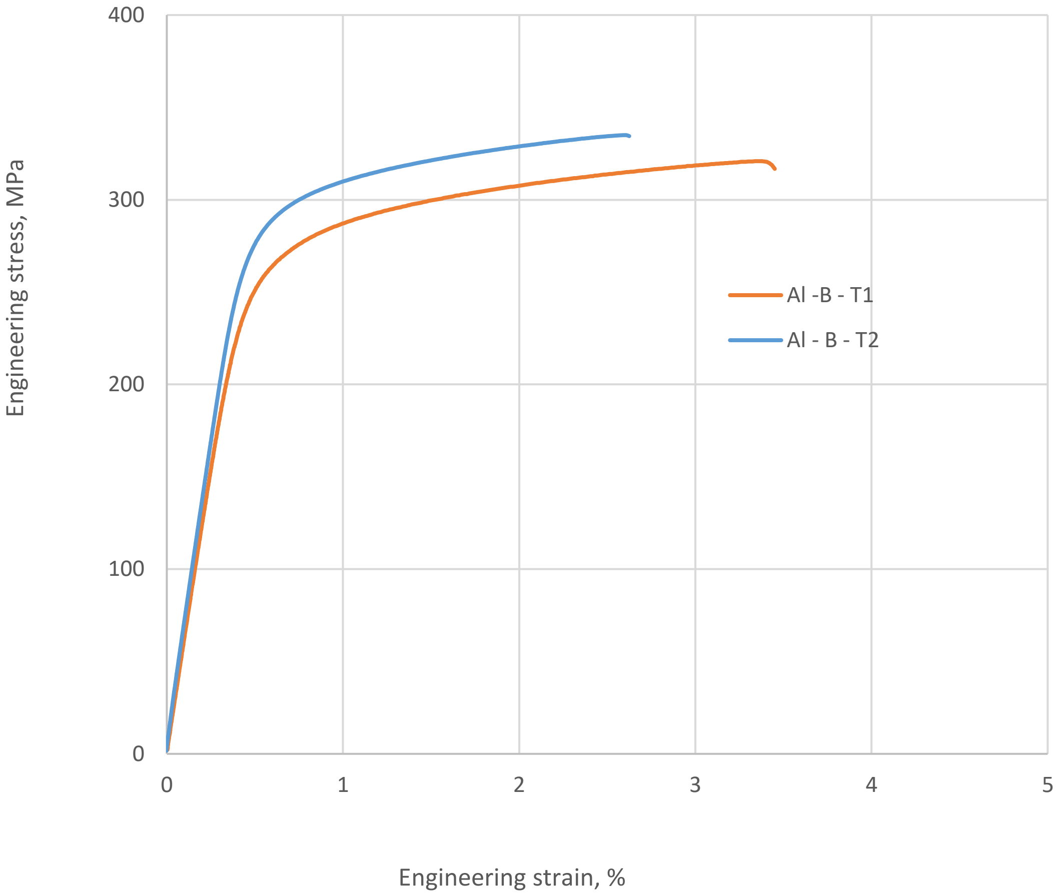

Figure 53 Tensile test results Al-B

Figure 53 displays the results of the tensile test, the two test samples drift apart slightly at the limit of the elastic range and exhibit different yield strengths. The elongation is slightly longer than that of the Al-A sample.

Table 28 Tensile test data of Al-B

	Ultimate Tensile Strength MPa	Std. Deviation	Yield Strength MPa	Std. Deviation	Tensile Elongation %	Std. Deviation
Al - B	327.93	9.97	279.07	19.70	3.04	0.59

the results are presented Table 28 with an acceptable deviation of the strengths, the ultimate and yield strengths of the two aluminum samples are extremely similar with only a difference in elongation.

4.5.4 Titanium A

The cold press and sintered titanium samples was tested using the MTS criterion universal test machine with a crosshead speed of 0.05mm/min.

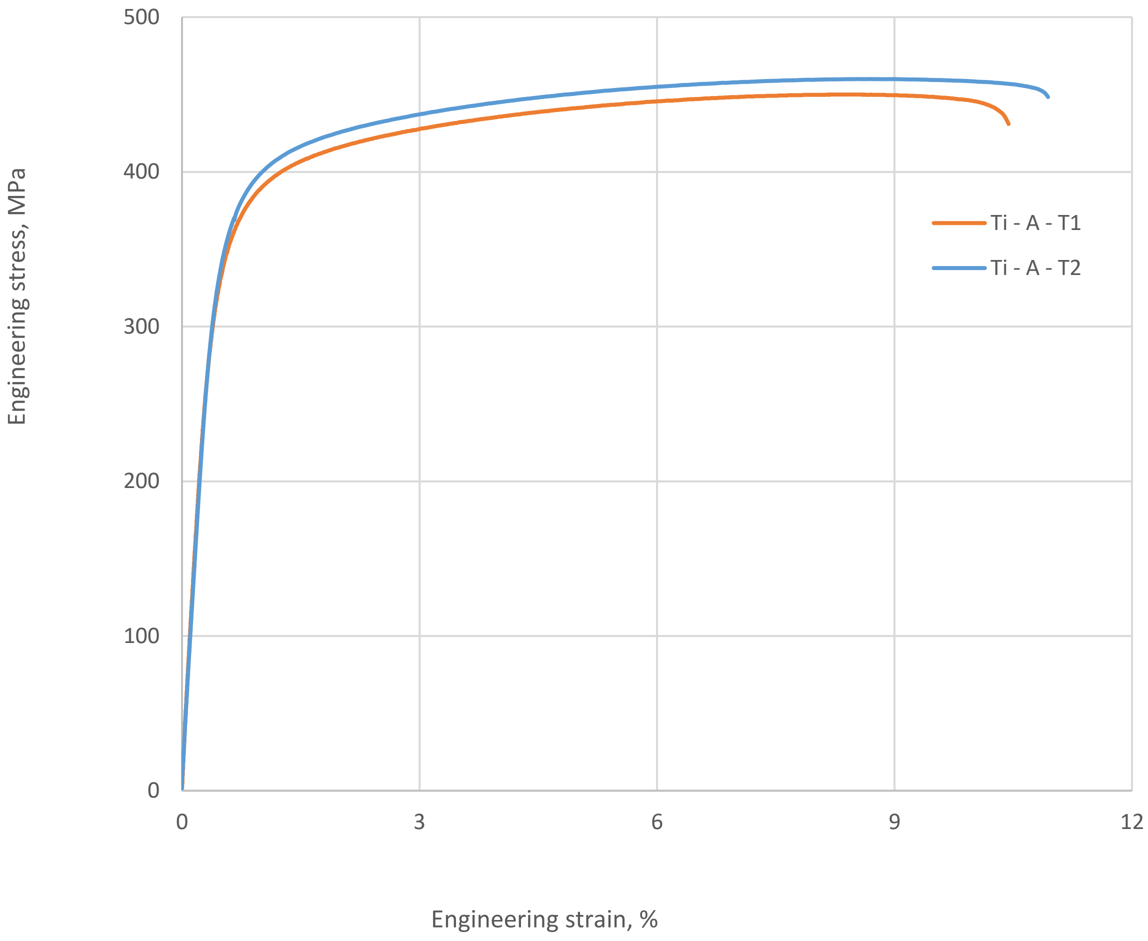

Figure 54 Tensile test results for Ti-A

Figure 54 is the tensile test plotted using the data collected during the tensile test, the two tests are nearly plotted on top of each other with a slightly lower yield point for test 1.

Table 29 Tensile data for Ti-A

	Ultimate Tensile Strength MPa	Std. Deviation	Yield Strength MPa	Std. Deviation	Tensile Elongation %	Std. Deviation
Ti - A	455.01	7.09	357.99	4.29	10.69	0.35

The results from the tensile test are presented in Table 29, with a UTS of 455.01 MPa and a yield strength of 357.99 MPa. The values are lower than those of TI-B but not by as much as would be expected considering the difference in porosity values, the TI-A does not seem to be as susceptible to weakening from pores during static loading.

4.5.5 Titanium B

The additive manufacture titanium was subjected to tensile testing where two samples were ruptured, the crosshead speed for both tests was 0.05 mm/min.

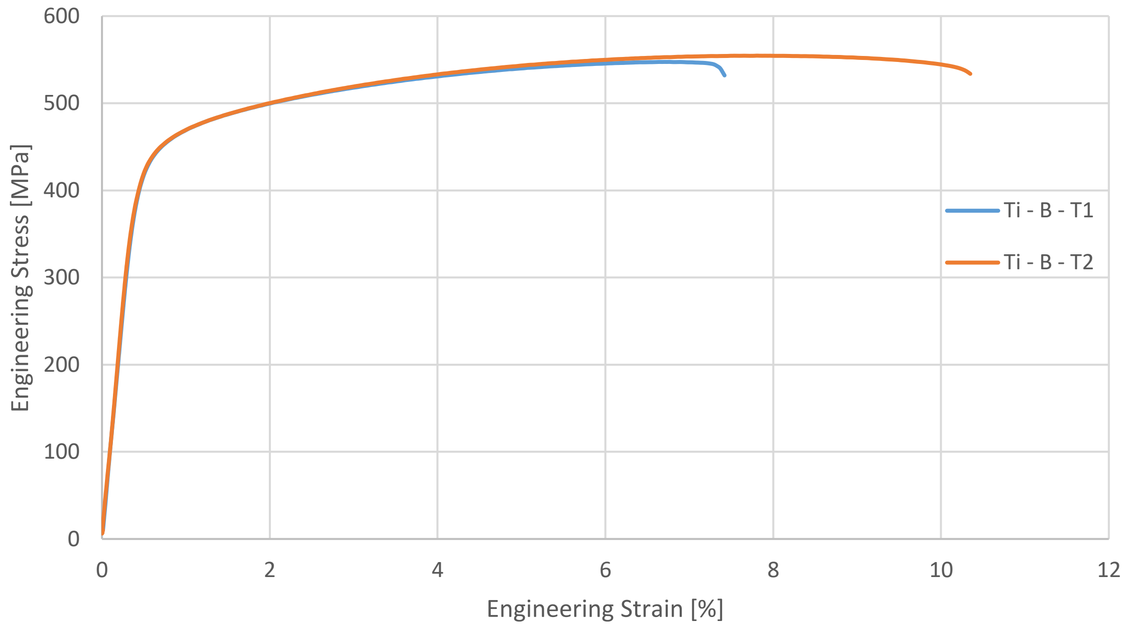

Figure 55 Tensile test results for Ti B

Figure 55 displays the graph of the tensile test conducted on Ti-B, the only difference from the two test comes from the elongation at rupture where the second sample ruptured before achieving the same elongation.

Table 30 Tabulated data from tensile testing of Ti B samples

	Ultimate Tensile Strength MPa	**Std. Deviation**	**Yield Strength MPa**	**Std. Deviation**	**Tensile Elongation %**	**Std. Deviation**
Ti - B	551.00	5.09	446.59	2.76	8.88	2.07

The calculated tensile values are presented in Table 30, the values show a small deviations from the mean with similar, the ultimate tensile strength of this material is comparable to fully wrought commercially pure titanium, grade 4 with a UTS of 550 MPa, however the yield strength and elongation is lower than that of commercially pure titanium [44]. The TiB inclusions could be responsible for comparable strength of fully dense materials, where a degradation in properties would be expected due to the porosity.

4.6 Compression Testing

This section summaries the results of the compression testing completed on the test materials, the test was conducted according to ASTM E9. The test samples were machined by the suppliers according to the specification in the standard to minimize buckling. The compression plates on the MTS criterion universal test machine were treated with molybdenum disulfide to limit the friction between the test pins and plates to deter the onset of barreling.

4.6.1 FC0205

The reference material was tested three times with a cross head speed of 0.05 mm/min.

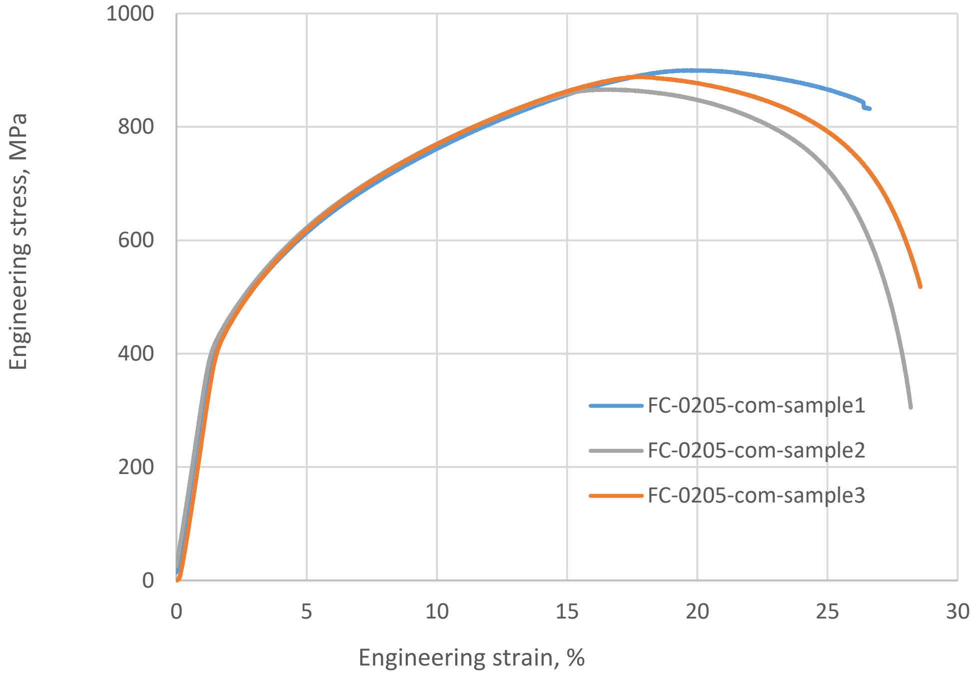

Figure 56 Compressive testing stress strain diagram of FC-0205

The graphs in Figure 56 from the compression test show consistency between the test samples with only slightly different ultimate compressive strengths.

Table 31 Compressive test summary for FC0205

	Ultimate Compressive Strength MPa	Std. Deviation	Yield Strength MPa	Std. Deviation
FC0205	884.87	17.14	420.17	8.63

The results of the compression testing on FC-0205 are shown in Table 31, the material displays a high compressive strength, this is due to the pore structure do not hinder compressive strength and could also slightly improve it as the amount more force is required to close some of the pores before the failure begins. The tensile and compressive yields exhibit different values due to the nature of distortion of the void structure under compression, where as the tension test meet a point of material overload due to the reduced cross section of the pores structure.

4.6.2 Aluminum Alloy A

The cold press and sintered aluminum alloy was tested in compression with a crosshead speed of 0.05mm/min, the test was completed for two samples.

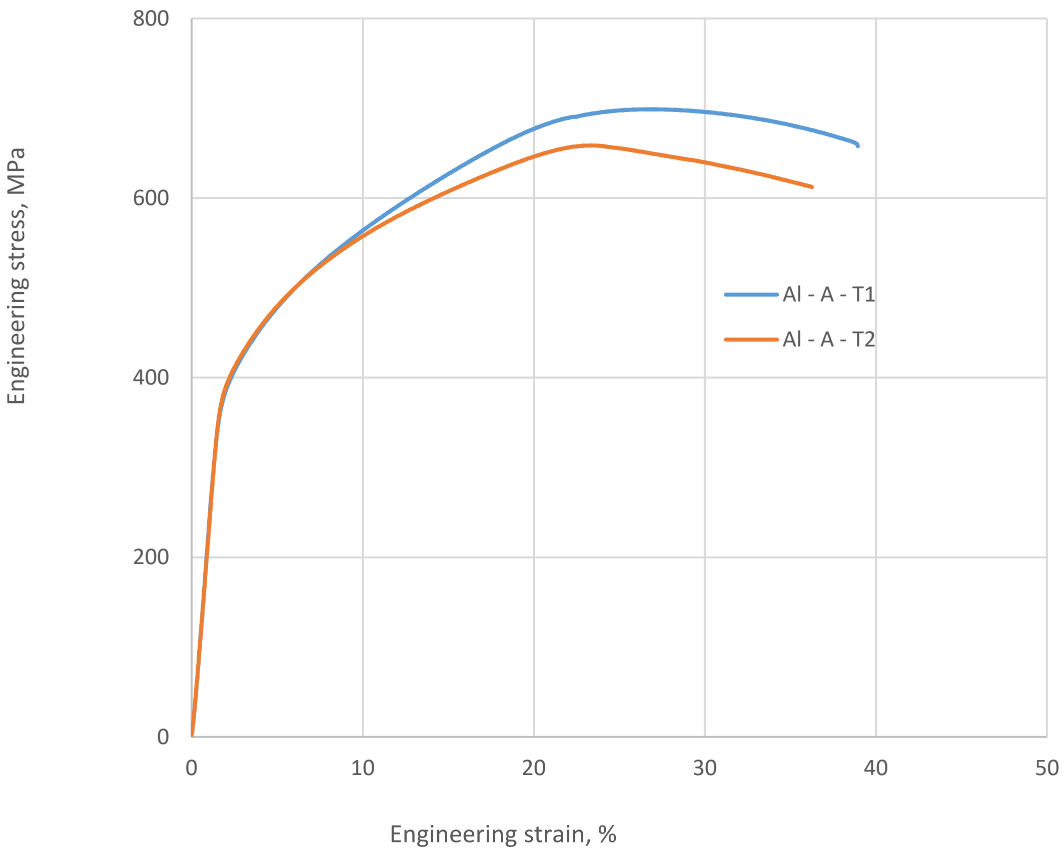

Figure 57 Compression test results of Al – A

Figure 57 presents the results from the compression test were both test show similar behavior into the plastic zone and only slightly deviate near the ultimate compressive strength.

Table 32 Compression test data summary Al - A

	Ultimate Compressive Strength MPa	**Std. Deviation**	**Yield Strength MPa**	**Std. Deviation**
AL - A	768.54	2.52	332.29	17.50

Table 32 shows the tabulated data from the compressive tests with an ultimate compressive strength of 768.54 MPa and compressive yield strength of 332.29 MPa, the relatively high compressive strength is due to the pore structure not hindering compressibility in the same manner as it does in tensile loading.

4.6.3 Aluminum Alloy B

The compression tests were completed on the aluminum alloy B, with a crosshead speed of 0.05 mm/min, the test was conducted on two compression samples.

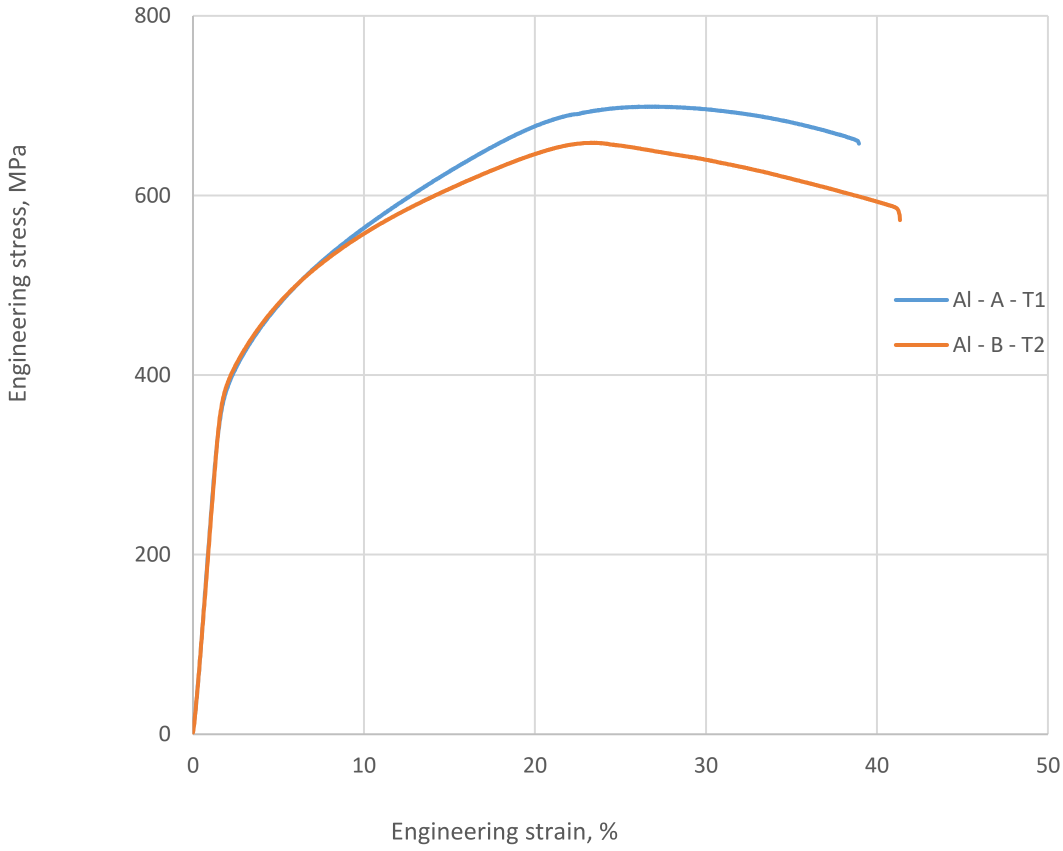

Figure 58 Compression test results of Al-B samples

The graph of compression data in Figure 58, shows a similar trend to that of Al-A maintaining consistency through the elastic region and only slight deviation in the plastic zone.

Table 33 displays the tabulated data from the compressive testing, comparing the aluminum samples the Al-B samples have lower compressive strengths and this may be due to the reduced porosity in the Al-B being able to close any applicable pores and plastically deforming to fracture.

Table 33 Compression test data for Al-B samples

	Ultimate Compressive Strength MPa	**Std. Deviation**	**Yield Strength MPa**	**Std. Deviation**
AL - B	637.52	9.43	346.87	17.50

4.6.4 Titanium A

The cold press and sintered titanium was tested in compression at a crosshead speed of 0.05 mm/min, the tests were completed to rupture twice.

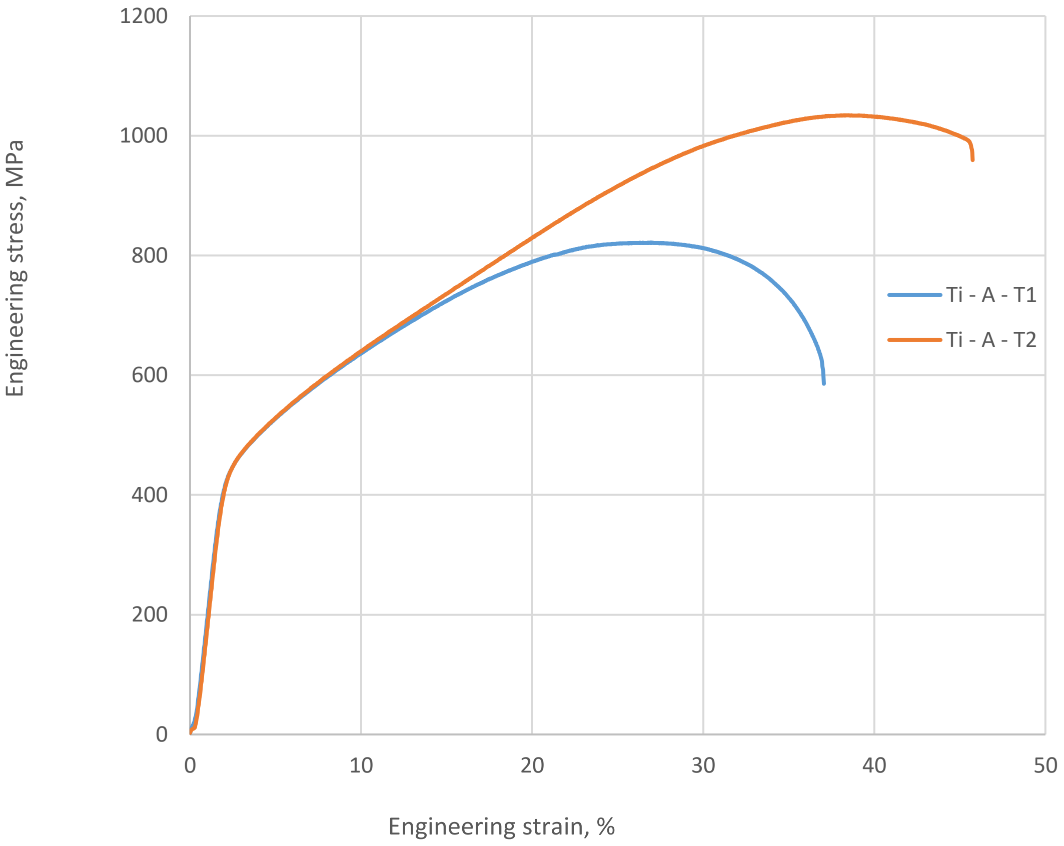

Figure 59 Compression tests results of Ti-A

The compression results are presented in Figure 59 with similar curves before the ultimate stress with a large variation of ultimate compressive strengths.

Table 34 Tabulated results of Compression testing of Ti-A samples

	Ultimate Compressive Strength MPa	**Std. Deviation**	**Yield Strength MPa**	**Std. Deviation**
Ti - A	927.79	150.64	395.11	0.07

Table 34 exhibits the tabulated data of the ultimate compressive strength and yield strength, the UCS is higher than that of Ti-B sample. The difference falls within the deviation of the measurements and could possibly be refined by more testing.

4.6.5 Titanium B

The additive manufactured titanium was tested in compression with a crosshead speed of 0.05mm/min, the test was completed twice.

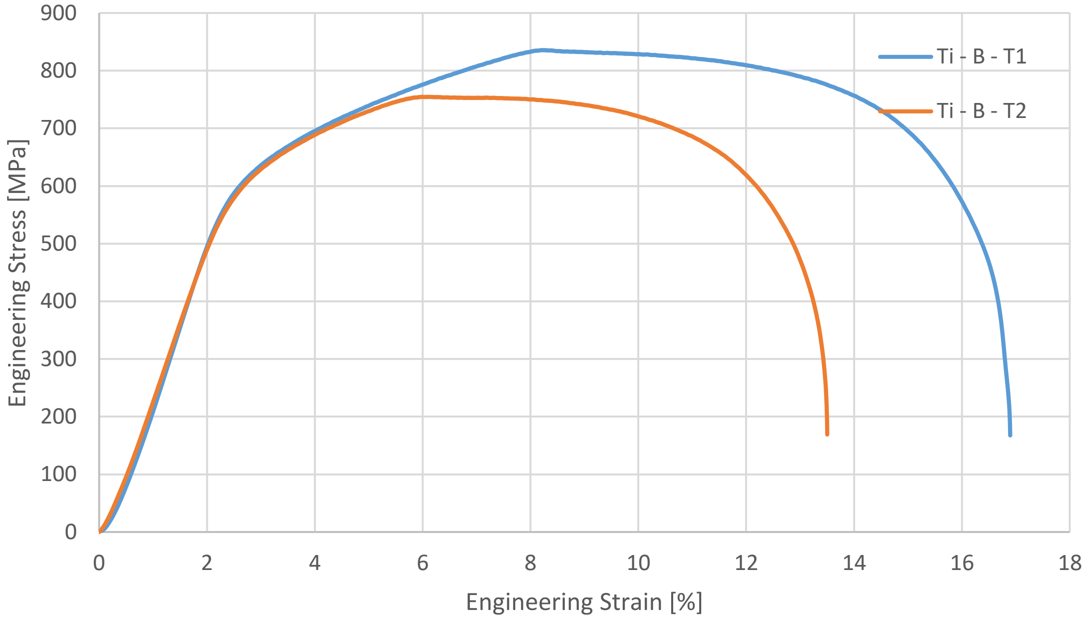

Figure 60 Compression test results of Ti B

Figure 60 shows a variation similar to that of Ti-A with a deviation occurring after yielding, the compressive strain for the low porosity material is lower than that of Ti-A which would be expected due to the distance required to collapse pore structures before rupture.

Table 35 Evaluated data from Compression test on Ti-B

	Ultimate Compressive Strength MPa	**Std. Deviation**	**Yield Strength MPa**	**Std. Deviation**
Ti - A	717.11	0.23	587.86	6.08

The data in Table 35 demonstrates the similar trend from Ti-A with a ultimate compressive stress of 717.11 MPa, and compressive yield stress of 587.86 MPa. The compression strengths were not utilized in this study as the industrial partner was to conduct a bolt torque testing within their facilities, however, these tests were cancelled after the compression testing was completed.

4.7 Fatigue

Fatigue testing of these material is the main focus of this research since the material will experience a cyclical loading if it is found to be a suitable replacement for reference material FC0205. The fatigue samples were prepared by their respective material manufacturers. To test the fatigue strength a sample will be subjected to a cyclic loading in a rotating beam fatigue machine were a constant weight is applied to a cantilevered end that is fixed to the free end of the sample. The other end is attached to a drive collet and rotated by means of an electric motor. The combination of a fixed end that is fixed other than a rotation about its own axis and a weight applied at a set distance a bending moment is induced in the test sample. The rotating beam fatigue machine designed to apply a bending moment in such a way that the maximum tensile loading on the outside of the test sample is equal but opposite that of the compression stress experience through half the cycle. This loading condition is defined as fully reversed loading condition where the ratio of stresses is equal to -1. The test sample is machine to have both ends at a constant diameter to be inserted in the fixture with the center to be reduced in diameter in a gradual manner at the center of the test specimen, the geometry is presented in Figure 12. The test samples are inspected for defects before the minimum diameter is measured and recorded, the sample is then lightly sanded along the long axis with a #000 steel wool before being inserted in the rotating beam machine. The desired stress in the fatigue samples is determined from Equation 5 and the load beam is set according to the manufacturers instructions.

After the test is concluded by either fracture at the midpoint of the test specimen or a successful test by surviving 10 million cycles or more. The stress and test results are recorded in a table similar to that shown in Table 36, with either a pass or fail condition recorded as an O or an X, respectively. Depending on the result of the previous test the next test is run at a lower stress if the previous test failed or a higher stress if the previous test passed, this is repeated for a minimum of 25 samples completed. Upon completed of the staircase chart, the mean alternating stress is determined using a weighted average based on the lowest stress that passed. A confidence interval is then calculated using the Student's t tables based on the number of samples is derived according to Equation 6. Failed test samples were inspected under SEM Microscope to characterize the fracture surface.

4.7.1 FC0205

The reference material was testing initially to determine a minimum threshold that the other samples had to overcome if they were determined to be suitable for a replacement material.

Table 36 Fatigue test results using staircase method

	Calculation of Endurance Limit: Staircase Method																									
	FC0205 P/M Copper Steel																									
		Test Results (X=Failure, O=No Failure)																								
Stress [Mpa]	Stress [kpsi]	1	2	3	4	5	6	7	8	9	10	11	12	13	14	15	16	17	18	19	20	21	22	23	24	25
241.32	35	X																								
203.40	29.5		X																							
193.05	28			X		X																				
182.71	26.5				O		X																			
172.37	25							X		X		X				X								X		X
162.03	23.5								O		O		X		O		X				X		O		O	
151.68	22													O				X		O		O				
141.34	20.5																		O							
	Cycles	62100	363900	5021800	10171900	2169900	746500	2732000	11013200	4923900	11072300	1559200	1860600	10151600	10349400	1114700	1727000	3945600	10324200	11601900	1518000	10290500	11929900	1969900	11633000	4640600

Table 36 shows the results of the staircase method for the FC0205 reference material with the initial stress was set to 241 MPa, this stress was selected based on one third of the ultimate tensile stress of the material to define a starting point of the test. The subsequent failures show a tendency to fail in the low cycle regime due to a high stress state.

Table 37 Fatigue stress confidence interval FC0205

Interval	[MPa]
s	17.4
σ_A 10%	187
σ_A 50%	164
σ_A 90%	141

Table 37 reports the confidence interval as well as the standard deviation of the mean, the 90% survival stress of 141 MPa is used as the maximum safe stress for design purpose when a fatigue condition is to be expected. The value corresponds to the published standard for 90% survivability fatigue limit of 140 MPa [39]. This value is used as the target for the other materials fatigue stress to be considered as a replacement for FC0205 material.

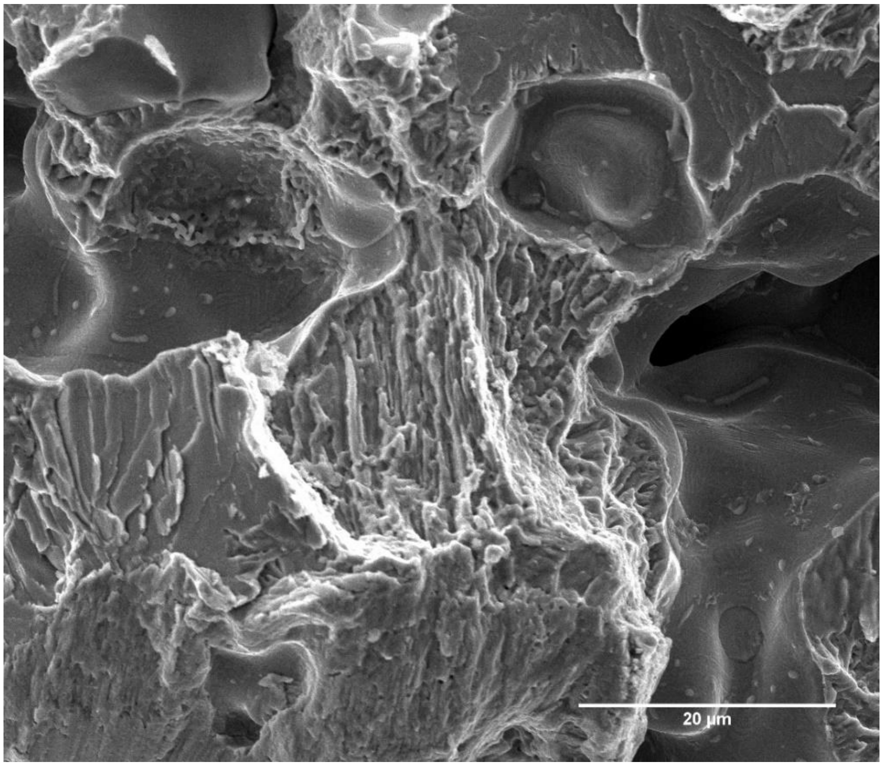

Figure 61 Fracture surface of FC0205

Figure 61 is taken from the fracture surface of a failure sample, the fracture surface shows evidence of serrations possibly from separation of pearlite colonies as well as cleavage fracture. There are two modes of fracture evident in this image that are formed during separate modes of stress overload, the degree of porosity in the material has an influence on the fracture modes. In porous structures it is not uncommon to find numerous fracture modes present within similar regions of a sample due to the propagation of the crack front as it comes into contact with the pore structure [53].

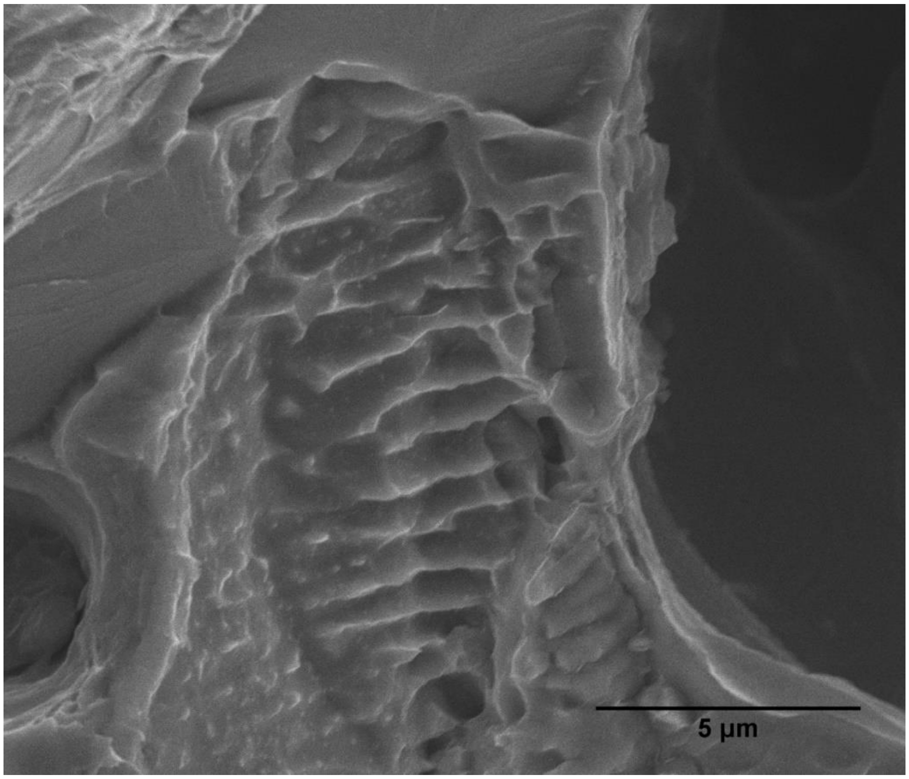

Figure 62 Magnified view of striations from plastic deformation

Along with overload fractures plastic deformation was also visible in close proximity to the other forms of fracture surfaces, Figure 62 shows striations formed from the cyclic nature of a crack opening to a point of plastic deformation and progressing the crack front, then to crack closure during the compression portion of the cycle. As the stress has to be higher than the localized yield strength of the material, high strength phases or inclusions can aid in the fatigue strength of the material.

4.7.2 Aluminum Alloy A

The cold press and sintered aluminum alloy was tested under fully reversed cyclic loading and the fatigue stress and fracture surfaces are presented below.

Table 38 Fatigue Test results staircase method for Al-A

	Calculation of Endurance Limit: Staircase Method																										
RBF Setting [in-lbs]	Aluminum alloy A																										
			Test Results (X=Failure, O=No Failure)																								
	Stress [Mpa]	Stress [kpsi]	1	2	3	4	5	6	7	8	9	10	11	12	13	14	15	16	17	18	19	20	21	22	23	24	25
40.91	151.68	22	X																								
39.95	141.34	20.5		X																							
38.98	131.00	19			X																						
38.01	120.66	17.5				X																					
37.04	110.32	16					X																				
36.07	99.97	14.5						X																			
35.10	89.63	13							X																		
34.13	79.29	11.5								X																	
33.16	68.95	10									X						X		X				X		X		
32.19	58.61	8.5										X		X		O		O		X		O		O		X	
31.22	48.26	7											O		O						O						O
		Cycles	73000	205000	146300	140000	393300	651200	613500	895400	1248900	4489600	11974200	3346700	10954700	10687400	2439100	11654800	3948100	791200	10384100	12241300	954300	1154100	6423800	4762900	10648500

Table 38 shows the results of the fatigue testing of the Al-A material, similar to that of FC0205, the initial stress was considerably higher than the fatigue stress that was eventually determined as indicated by the majority of failures that occurred at the onset.

Table 39 Fatigue stress confidence interval Al-A

Interval	[MPa]
s	4.67
σ_A 10%	64.8
σ_A 50%	58.6
σ_A 90%	52.4

The 90% survivability fatigue stress was presented in Table 39 calculated to be 52.4 MPa, being considerably lower than that of the FC0205 reference of 141 MPa makes the aluminum sample unsuitable as a possible replacement material. The staircase method did not show a large variation in the stress that passed the fatigue test and only varied by 10 MPa and thus leading to a standard deviation of 4.67 MPa showing a low tolerance for fluctuations in stress.

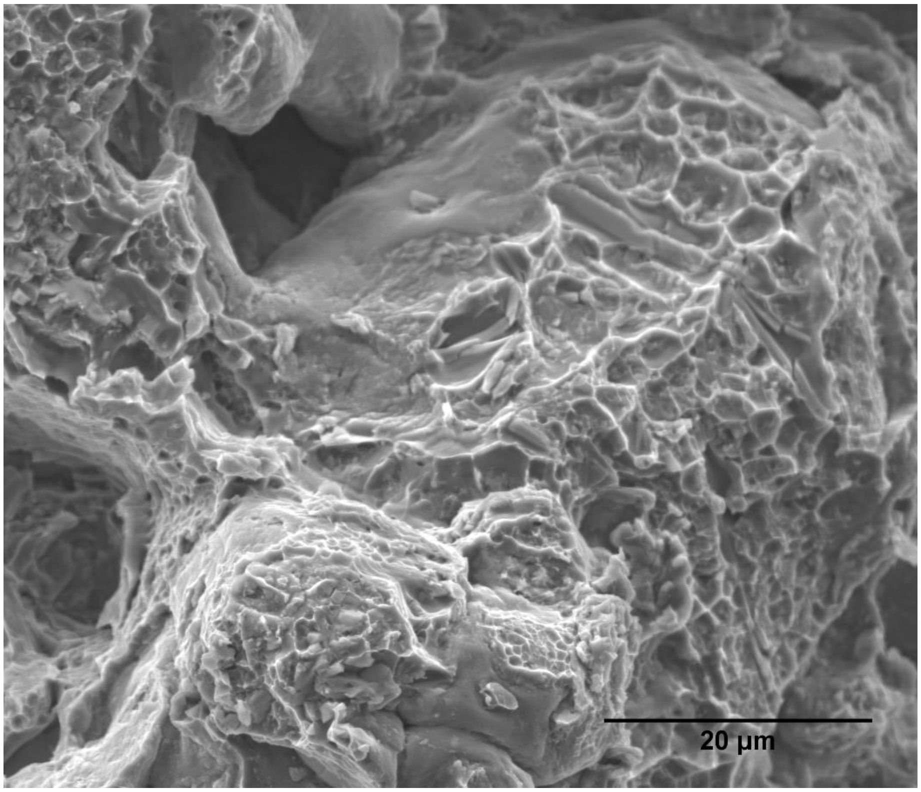

Figure 63 Fracture surface showing ductile tearing Al-A

Figure 63 shows a fracture image from the Al-A sample showing regions of ductile tearing and dimple rupture from the micro void coalescing during plastic deformation along the crack front, there are small areas that show serration intermixed with the dimple rupturing. EDS mapping was conducting on the fracture surface to determine if any compositional changes had a significant effect on the fracture surface. The maps are presented in Figure 64, showing a dispersion of copper in solid solution throughout the sample, magnesium concentrations are visible in the lower section of image where ductile tearing and dimple ruptures are present. There is no significant difference in fracture surface that has a high concentration of magnesium as compared to the bulk matrix.

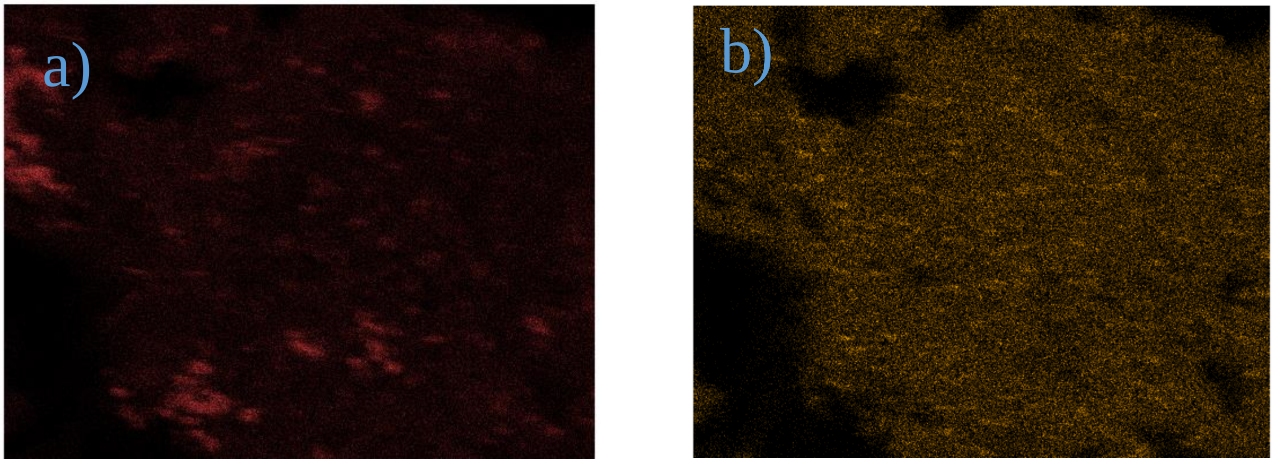

Figure 64 Concentration of (a)Mg and (b) Cu in Al-A from fracture surface of Figure 63

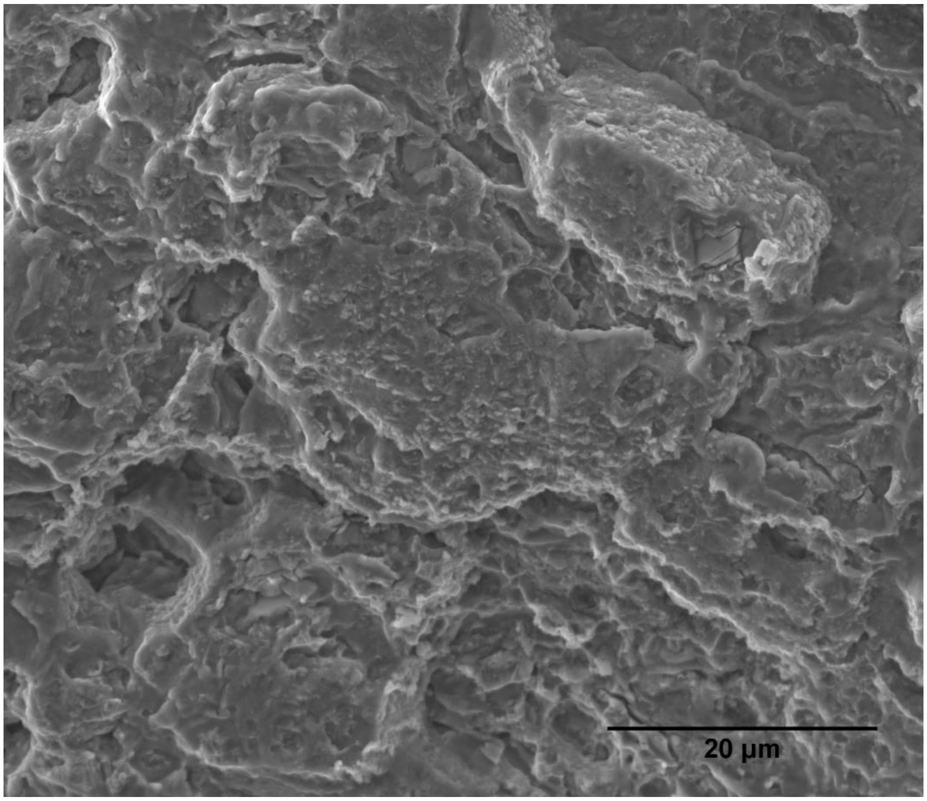

Figure 65 Fracture surface with serrated edges from fracture Al-A

Figure 65 shows a secondary SEM image of a fracture surface from Al-A test samples with a high degree of serrations formed in an overload region causing a catastrophic failure, there is some evidence of cleavage fracture with the image as well.

4.7.3 Aluminum Alloy B

The cold press and sintered aluminum alloy B was tested under fully reversed cyclic loading and the fatigue stress and fracture surfaces are presented below.

Table 40 Fatigue test results staircase method Al-B

Calculation of Endurance Limit: Staircase Method																										
Aluminum alloy B																										
		Test Results (X=Failure, O=No Failure)																								
Stress [Mpa]	Stress [kpsi]	1	2	3	4	5	6	7	8	9	10	11	12	13	14	15	16	17	18	19	20	21	22	23	24	25
137.90	20	X																								
127.55	18.5		X																							
117.21	17			X																						
106.87	15.5				X																					
96.53	14					X																				
86.18	12.5						X																			
75.84	11							X		X				X						X				X		
65.50	9.5								O		X		O		X		X		O		X		O		X	
55.16	8											O				O		O				O				O
	Cycles	112100	116600	124700	142100	1648600	1563300	2559000	10175400	4568100	1576300	5043800	16971200	895300	3546900	11325400	1247300	16748100	13475100	749100	9821400	11569000	10987600	4573100	2579600	13654800

The fatigue test results shown in Table 40 for Al-B are similar to that of Al-A where there is a steady decrease of stress in the initial test pieces. The preliminary test samples failed in the low cycle regime until the first test that passed 10^7 cycles at 65.5 MPa after which tests steadied between a passing stress range of 55.16 MPa to 65.5 MPa. The 90% survivability fatigue stress is much lower than the reference materials of 141 MPa but the Al-B material is slightly higher than that of Al-B by approximately 6 MPa. Table 41 shows the mean stress calculated from the fatigue result at 64.93 MPa with a standard deviation of 4.62 MPa, resulting in a 90% survivability fatigue stress of 58.83 MPa.

Table 41 Fatigue stress confidence interval Al-B

Interval	[MPa]
s	**4.623**
σ_A 10%	**71.02**
σ_A 50%	**64.93**
σ_A 90%	**58.83**

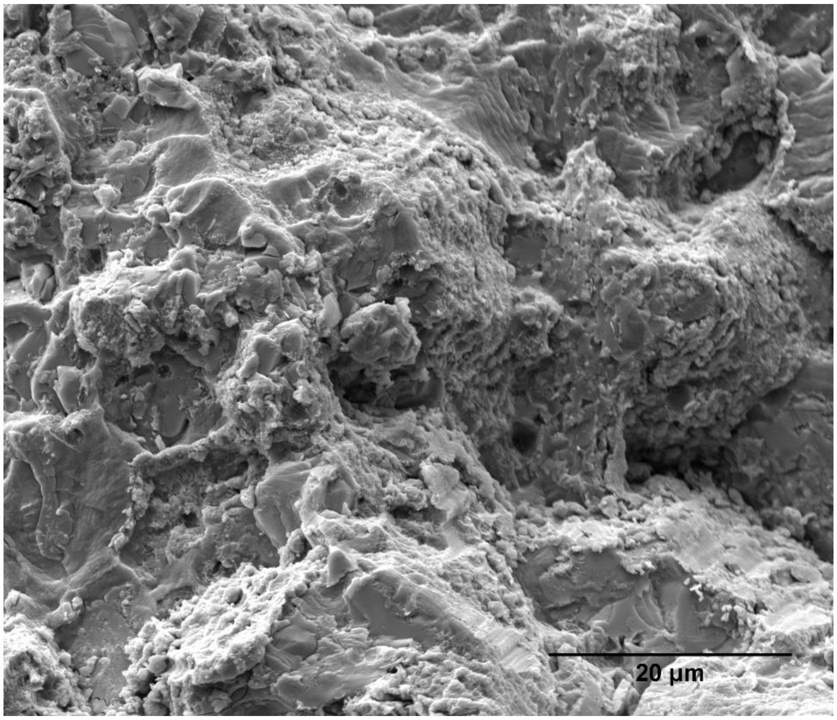

Figure 66 Fracture surface with granulated edges and regions of cleavage fracture

The fracture surface shown in Figure 66 is considerably different from that of Al-A, the topography has more variation from intergranular fracture that follows forces the crack path around the larger grain sizes. There is a granulated crack surface with evidence of cleavage fractures on the fracture surface. The fracture surface pictured was examined under EDS to determine if elemental composition has an influence on the fracture surface, the mapping is presented in Figure 67 below. The copper in this material is shown as a secondary phase but does not seem to influence the fracture surface in an appreciable way, the magnesium is similar to that found in Al-A where there appears to be a occurrence of cleavage fracture in the areas with high concentrations of magnesium.

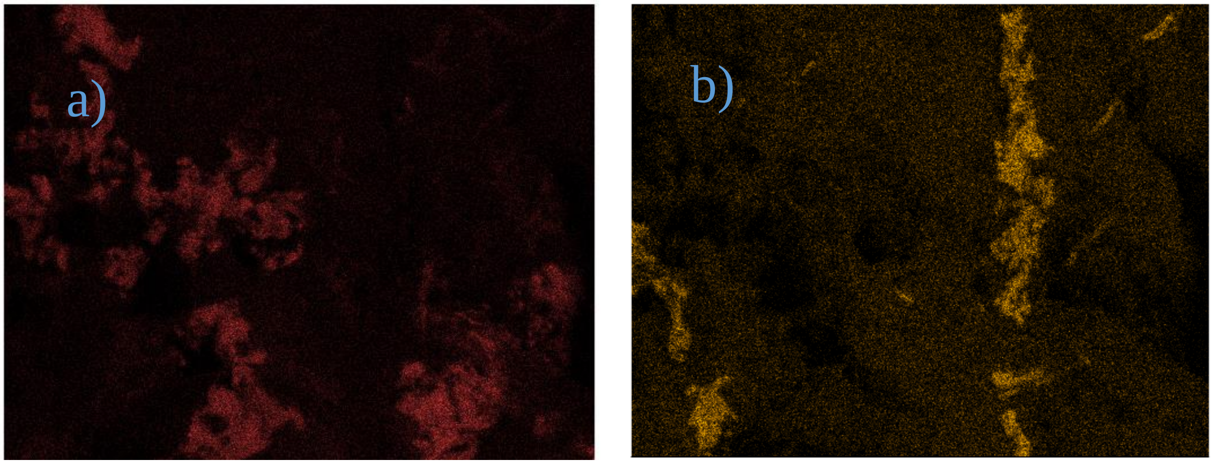

Figure 67 Elemental compositional mapping (a) Mg concentrations and (b) Cu concentrations

The presence of micro voids also leads to ductile tearing as seen in Figure 68, also showing a magnified view of the crenulated edges of the fracture surfaces. Absent in the fracture images are areas of smooth pore walls that are seen in Al-A and FC0205. The fracture appears to the shape of cup that is representative of ductile fracture, with the surface showing signs of micro void coalescences that lead to fracture. Although the fracture surfaces show a difference in fracture modes the fatigue strengths are very similar and appear independent of the grain size, pore morphology or degree of porosity.

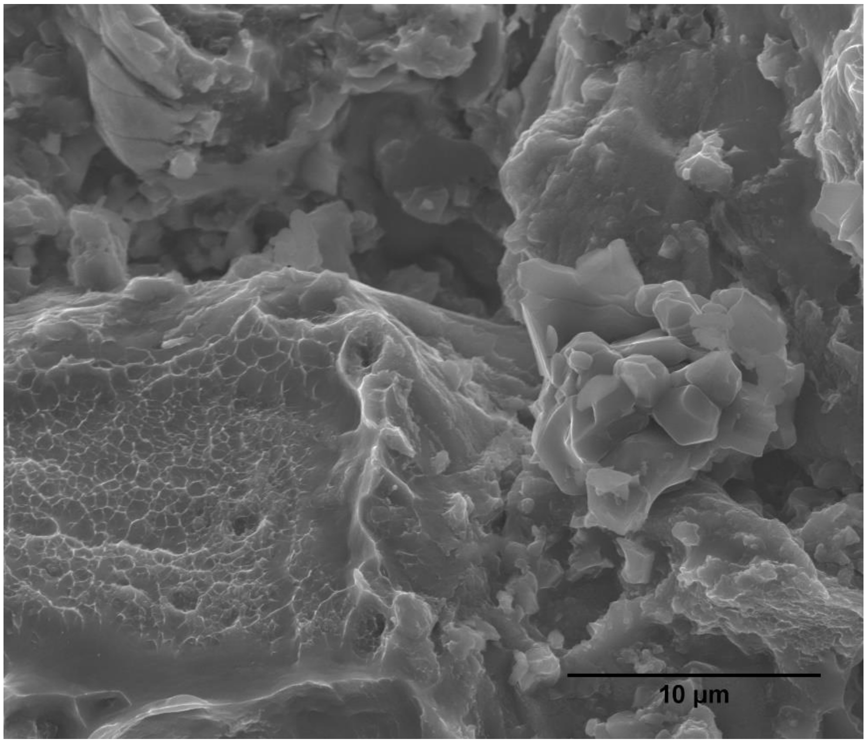

Figure 68 Secondary electron image showing micro-ductile tearing

4.7.4 Titanium A

The cold press and sintered titanium material was testing under fully reversed cyclical loading beginning with an initial stress based on a third of the tested ultimate tensile stress equal to 131 MPa.

Table 42 Fatigue test results staircase method Ti-A

Calculation of Endurance Limit: Staircase Method																										
Titanium A																										
		Test Results (X=Failure, O=No Failure)																								
Stress [Mpa]	Stress [kpsi]	1	2	3	4	5	6	7	8	9	10	11	12	13	14	15	16	17	18	19	20	21	22	23	24	25
131.00	19	X																								
120.66	17.5		X																X							
110.32	16			X		X		X		X								O		X						X
99.97	14.5				O		O		O		X		X		X		O				X		X		O	
89.63	13											O		O		O						O		O		
	Cycles	5072100	850200	1318300	10043100	1403800	10024600	444500	10911200	3167200	3305200	10696400	5425900	10358800	3876300	10039200	1031920	10324000	1054400	1521000	1156700	12764100	7766300	10856100	11459600	1786500

The fatigue results presented Table 42 show less variability within the range of tested stresses with a correlation with fatigue of fully wrought titanium materials that have fatigue endurance limit around a third of the ultimate tensile strength. That is not to say that this material experiences a fatigue limit or a stress which below that the material does not exhibit a response to fatigue stress, more testing would have to be completed to see if that is a possibility. The passing stress has an upper limit of 110.32 MPa and a mean stress of 101.38 MPa. The 90% survivability presented in Table 43 based on the fatigue results for Ti-A is 91.62 MPa, a considerable amount lower than FC0205 at 141 MPa.

Table 43 Fatigue stress confidence interval Ti-A

Interval	[MPa]
s	**7.41**
σ_A 10%	**111.15**
σ_A 50%	**101.38**
σ_A 90%	**91.62**

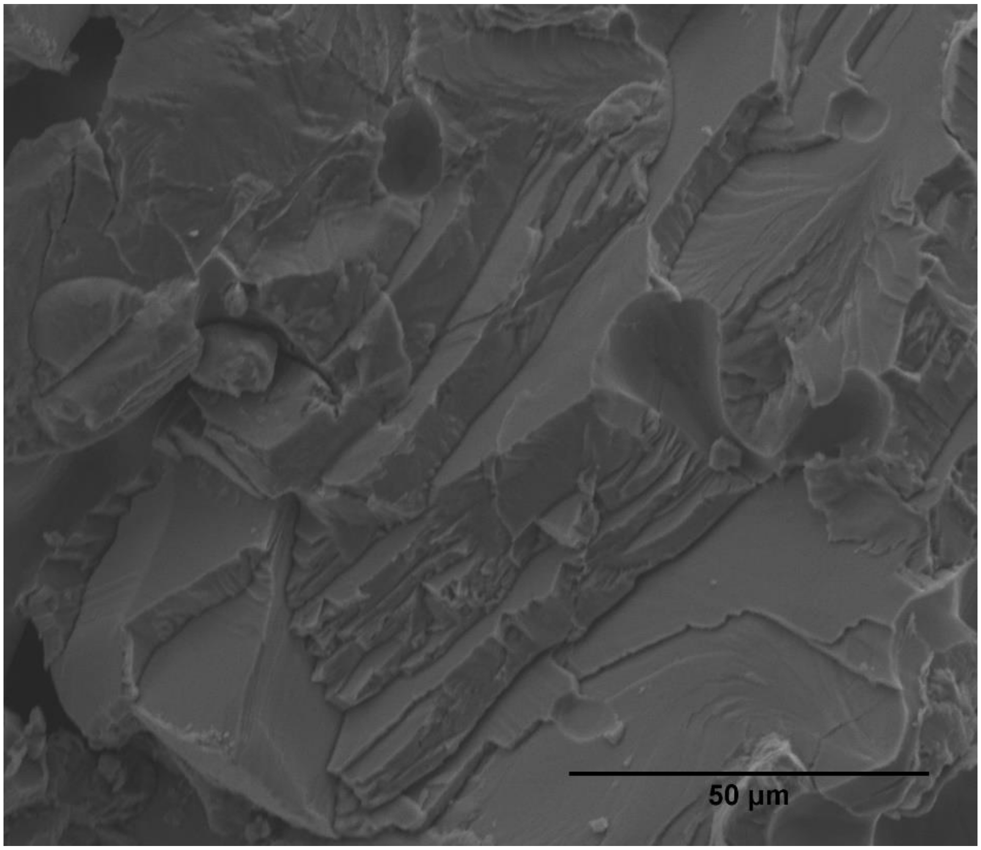

Figure 69 Ti-A fracture surface exhibiting cleavage fracture

The fracture surface of Ti-A displayed in Figure 69 exhibits a fracture surface of complete cleavage fracture with a variation in topography across the surface. Pores are visible and in the fracture plane and seem to have some influence on the crack path, the fracture surface has numerous pores that have been sheared through. There is evidence of smaller ancillary cracks that propagated in separate directions than the main crack.

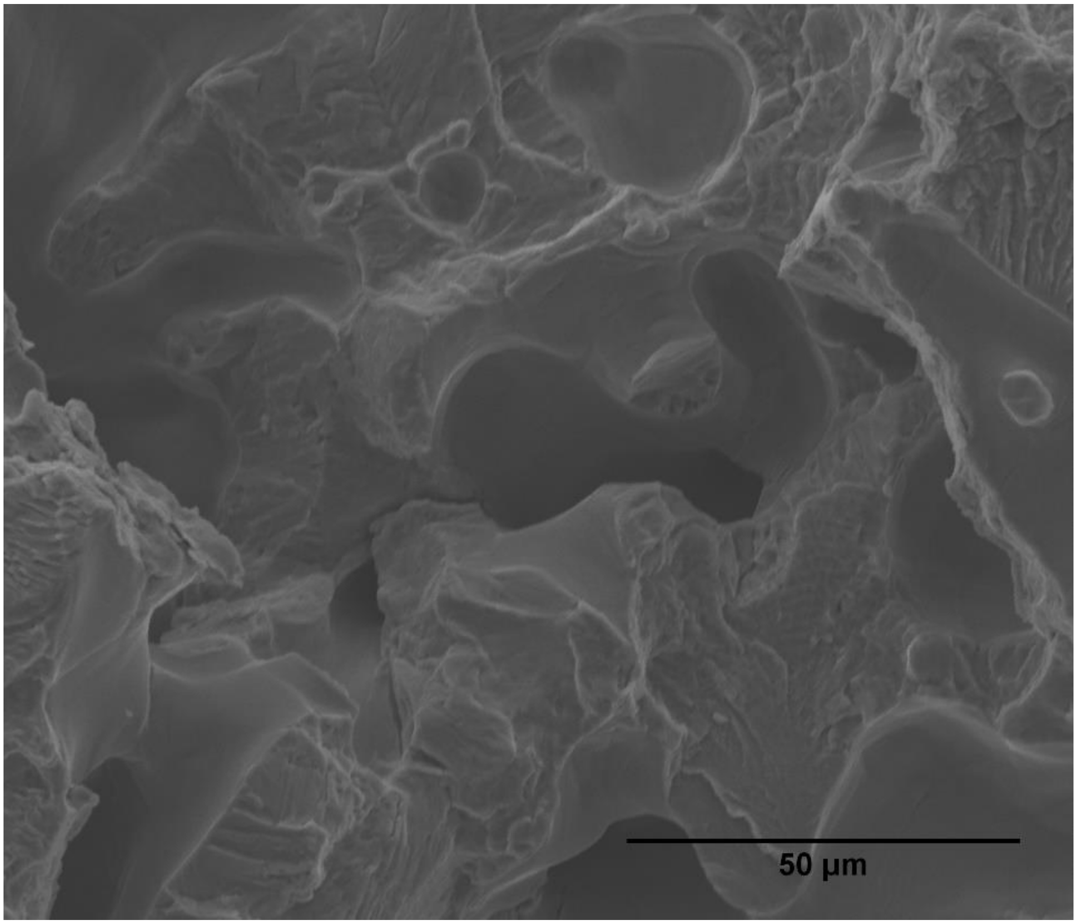

Figure 70 Fracture surface around pore structure with visible striations

Smooth pores are evident in both images, however, this secondary electron image is centered on a pore and the fracture surface shows signs of ductile tearing, strirations from plastic deformation opening and closing a crack surface as well as cleavage fracture in the areas where the pores have intercepted the crack front. Internal secondary cracks are also evident within the structures connecting pores, and would be a possible reason why the fracture surface of Figure 69 shows a variation in elevations if secondary cracks extending outwards into the bulk of the material were activated and allowed for a large section to release as a catastrophic failure.

4.7.5 Titanium B

The fatigue stress of the additive manufactured titanium material was tested with a rotating beam fatigue machine under completely reversed loading. The initial stress was set based on a third of the ultimate tensile stress of the material.

Table 44 Fatigue test results staircase method Ti-B

Calculation of Endurance Limit: Staircase Method																										
Titanium B																										
		Test Results (X=Failure, O=No Failure)																								
Stress [Mpa]	Stress [kpsi]	1	2	3	4	5	6	7	8	9	10	11	12	13	14	15	16	17	18	19	20	21	22	23	24	25
320.61	46.5																						X			
310.26	45																					O		X		O
299.92	43.5																				O				O	
289.58	42																			O						
279.24	40.5																		O							
268.90	39											X		X				O								
258.55	37.5										O		O		X		O									
248.21	36									O						O										
237.87	34.5								O																	
227.53	33							O																		
217.18	31.5						O																			
206.84	30					O																				
196.50	28.5				O																					
186.16	27			O																						
175.82	25.5		O																							
165.47	24	O																								
	Cycles	10115500	11373500	10329600	10660400	11837400	11837400	11274200	10031600	1000000	10400000	704200	10523200	9803200	1139300	10552400	11017200	10281900	10548600	10809200	10912500	11847900	3866900	4439600	1086400	11157400

The fatigue results given in table Table 44 display a different trend than the previous materials tested, the fatigue strength is found to be greater than one third of the UTS of the material of 165 MPa. In comparison between the titanium materials, a tensile load would load all the pores in the cross section at one time and failure would occur at the minimum cross-sectional area that had the largest accumulation of pores on a given plane that was perpendicular to the tensile direction. In a porous material, similar to the previous tested, there would be numerous activation planes. In a low porosity material, as in Ti-B there is a lower probability that of pores will occur along an activation plane leading to a fracture in tensile testing resulting in a higher tensile stress. In contrast to a fatigue stress, the probability of a pore is at the outside edge or near subsurface of a fatigue sample is much lower with less than 1% porosity as seen in Ti-B.

The fatigue stress shows a bimodal behavior with an earlier failure plateau at 268.5 MPa, with a large number of subsequent tests that passed until another failure was reached near 320.61 MPa. This material exhibited a large number of samples that passed when compared to the previous tested materials.

Table 45 Fatigue stress confidence interval Ti-B

Interval	[MPa]
s	**98.3**
σ_A 10%	**503**
σ_A 50%	**373**
σ_A 90%	**244**

Table 45 displays the calculated 90% survival rate at 244 MPa with a large variation in fatigue stress with a deviation of 98.3 MPa due to the plateau in the test results and based on the calculation formula takes the lowest value of passes or fails depending on the number of each. This material has a fatigue strength well above the reference material FC0205 of 141 MPa and with the other superior mechanical properties such as tensile strength and hardness it would be only material from the test subjects that is candidate material substitution based on the objectives of the research.

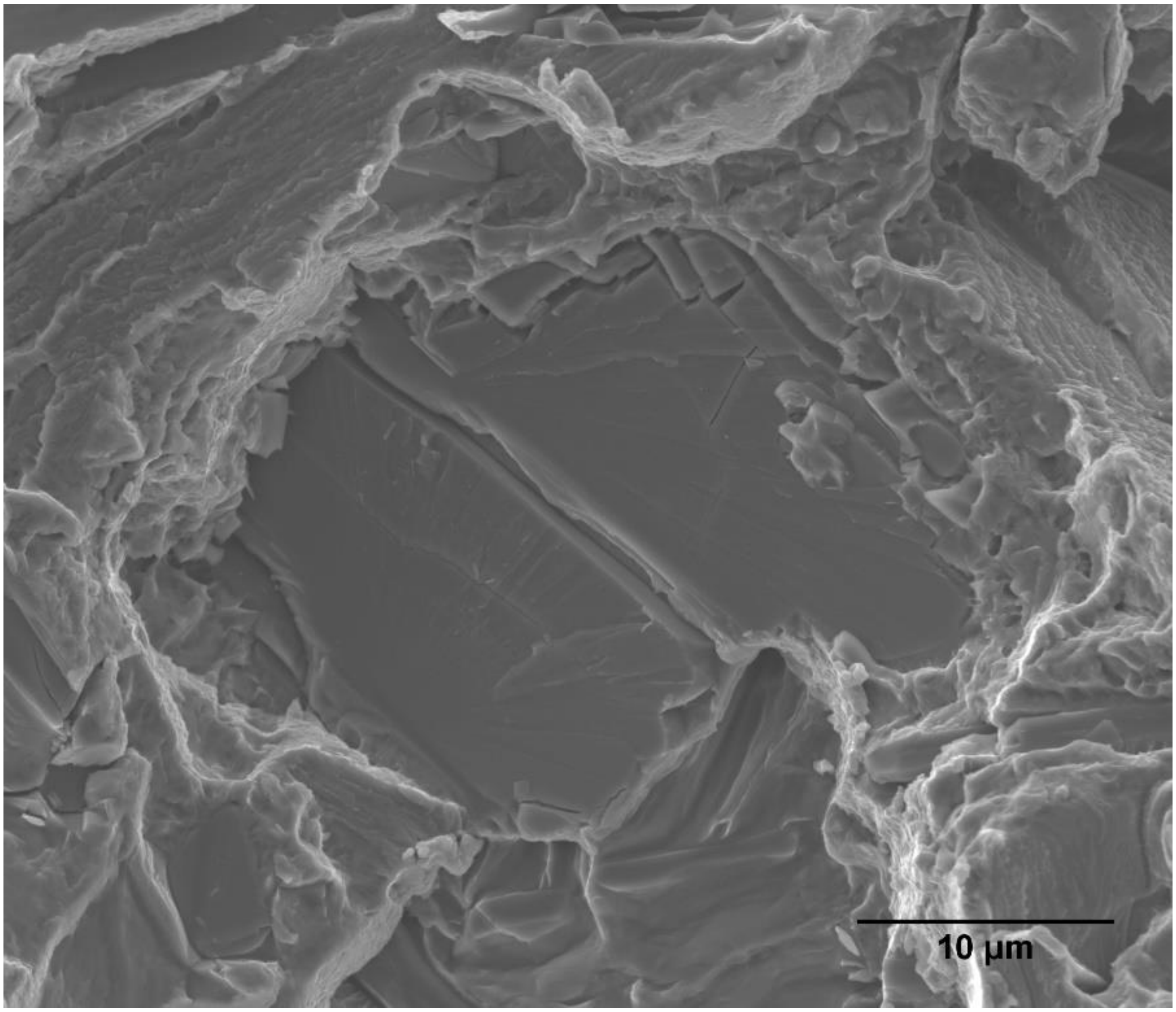

Figure 71 Ti-B fracture surface showing intragranular fracture of an intermetallic

The secondary electron image Figure 71 shows the fracture surface centered on an intermetallic that been fractured by the crack caused by cyclical loading. The intermetallic is fractured by a cleavage fracture where the surrounding areas show signs of serrations. The TiB intermetallic shows signs of a ratcheting behavior, fracture face on a different plane than the surrounding areas.

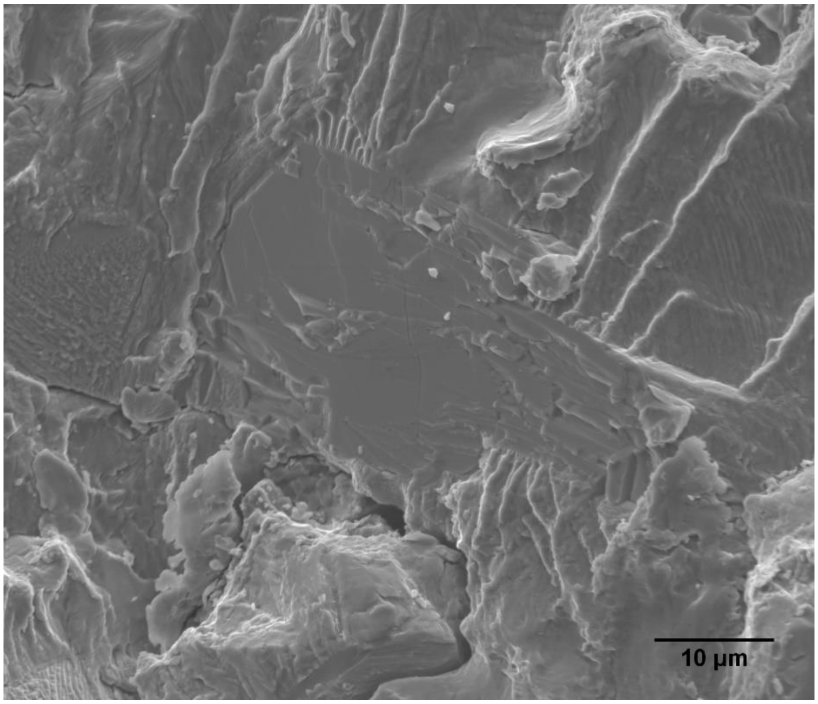

Figure 72 Fracture surface with cleavage fracture and striations

Figure 72 exhibits a relatively smooth fracture plane in comparison to the other materials especially the Ti-A material. The Ti-B inclusion in the center of the image is also experiences cleavage fracture, however, the surrounding area shows evidence of striations from the plastic deformation of a crack front opening and closing from the cyclical stress state. This difference in fracture methods that are typical for ductile and brittle materials shows a difference in hardness and strength of the intermetallic compared to the matrix. This difference in the strengths of the inclusion leads to an increase in mechanical properties of the material that are contributed to these intermetallics.

Chapter 5: Discussion

The following section discusses the results obtained during this research investigation which is divided into three sections.

The first section is focused on the fatigue properties of the test material due to the intended use of the material and the expected limiting factor will be cyclic loading. The relation to fatigue strength and pore morphology, degree of porosity, and inclusions were studied. The second section discussed general mechanical properties as they relate to the test plan. In the third section, the titanium B material is discussed on the basis of the superior properties. The intermetallic phase and its relation to fatigue strength is discussed.

5.1 Fatigue

The purpose of the study was to validate a suitable lightweight material among the ones provided, produced through a near net shape process which facilitates high production volumes and low per part cost. Due to the cyclical loading that the internal combustion engine component will experience in service, fatigue strength becomes a defining factor. The current material used in the application is a cold press and sintered steel produced by powder metallurgy techniques. Referencing Table 37 we identify the rotating beam fatigue stress for FC0205 with a projected 90% survivability rate of 141 MPa this sets a minimum fatigue stress minimum that must be met for the proposed materials considered as a suitable replacement. Figure 73 shows the S-N curves for all materials tested, the aluminum samples were nearly identical in fatigue strengths while being less than that of the Ti-A material. The lightweight cold press and sintered materials occupy similar positions on the S-N curve, with the reference material having a higher fatigue strength with a higher porosity than the other materials. Considering the fatigue strength alone the only material that meets or exceeds the fatigue strength of the reference materials of 141 MPa is Ti-B, the additive manufactured material with a fatigue strength at 90% survivability of 244 MPa. The other proposed materials did not meet this minimum fatigue strength the next closest material would be the Ti-A cold press and sintered material, which was found to have a 90% survivability of fatigue strength at 91.62 MPa.

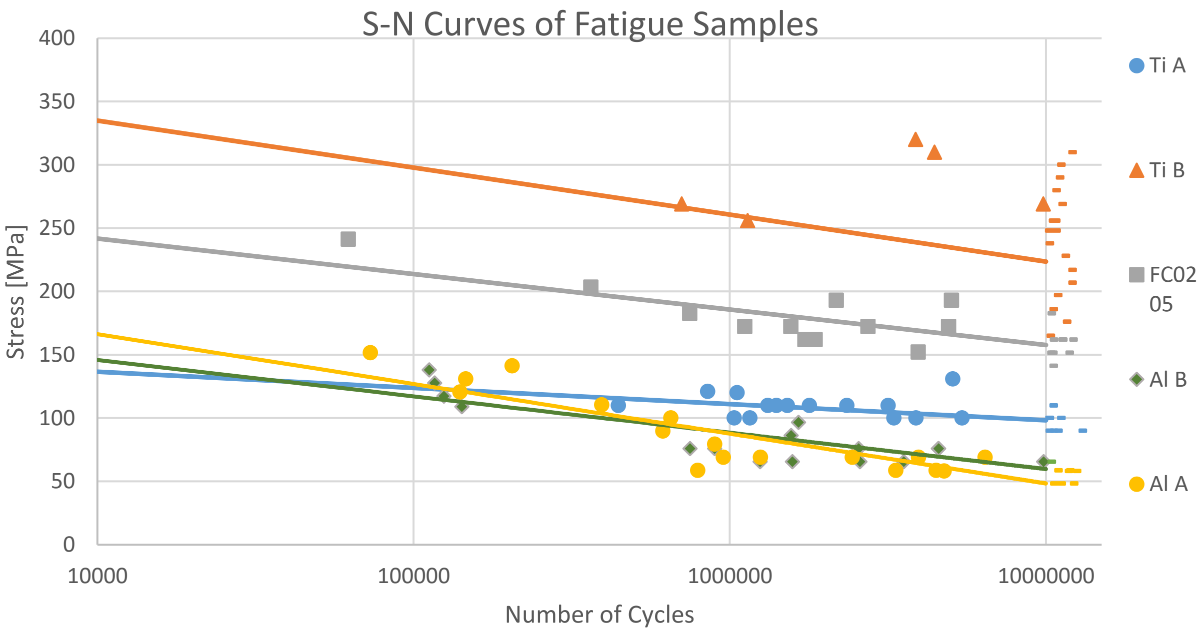

Figure 73 S-N curves for all tested materials

Common fracture mechanisms were observed in all alloys tested, the fracture surfaces of the porous parts were difficult to identify the origin of the fracture initiation due to the lack of indicators. The initial fatigue induced cracks were presumed to initiated at pore structures at the surface or just below it. The fracture images of the aluminum samples indicated a higher degree of plastic deformation in the form ductile tearing and interparticle dimple rupture, fracture surfaces of the Al-B materials had a coarse fracture structure when compared to Al-A. The titanium fracture images displayed further cleavage fracture and serrations than that of the aluminum surfaces. Striations were observed in all fracture images resulting from crack closure and plastic deformation in the fully reversed cycling. The different fracture mechanisms were found to be intermixed within the same regions. Fracture mechanisms that would be expected to be seen in separate regions in a wrought material, such as striations and ductile tearing were found near areas of fast facture indicated by cleavage fracture zones. Due to the pores within the structure intercepting the crack propagation path the cross-sectional area of the test piece would be inconstant flux as the crack would start bridging pore structures together resulting in a sudden overload and fast fracture.

The fracture strength of the FC0205 reference material can be aided by the presence of secondary phases within the structure as seen in Figure 29, that may offset the instability caused by the higher porosity found in the steel structure. Copper is also evident as a second phase in the FC0205 material, and can be seen in the transgranular fracture in Figure 61. Ti-B was also found to contain a secondary phase of TiB and appears to aid in the mechanical properties of the materials. Precipitates were expected within the aluminum alloys based on the composition and identified under EDS mapping, of the polished samples as well as fracture surfaces. The was no indication if they aided or hindered the fatigue life of the aluminum samples. The addition of secondary phases can have a positive or negative effect on the fatigue life of materials depending on the bond strength between the inclusion and the matrix [33], [53]-[54].

Sintered pore shape has an effect of the fatigue strength of the material, smooth circular pores having a lower stress intensity factor than that of irregular shaped pores structures with sharp features. Ti-A and Ti-B microstructures show smooth circular pores within the microstructure shown in Figure 25 and Figure 28, with an average pore size of 0.158% of area and 0.0028% of area for the respective materials. FC0205, Al-A and Al-B had pore morphology ranging from smooth to irregular shape that conformed around the grain structure leading to potential regions of high stress states [55]-[56].

5.2 Mechanical Properties

Comparing the resulting mechanical properties the additive manufactured Ti-B samples shows superior properties in all the categories tested with a density measurement that is close to that of conventionally produced titanium of 4.507 g/cm^3 [58]. The mechanical properties of materials with pore structures show a direct relation degree of porosity and degradation of properties. The intermetallic inclusions also play a role in improved hardness and tensile strength, however, the degree to which the improved would need more testing to quantify. The specific fatigue strengths of the cold press and sintered materials all fall within a range between 20.4 – 22.3 kNm/kg, with the additive manufactured Ti-B has a specific fatigue strength of 57 kNm/kg. The substitution of FC0205 with any of the tested cold press and sintered materials would not result in a weight savings at equivalent stress levels.

5.3 Additive Manufactured Titanium

The additive manufactured titanium was the only material that had the material properties that were superior to the FC0205 reference material in all testing categories. The superior fatigue strength is attributed to the low porosity of the material as well as the presence of intermetallic that appears to strengthen the fatigue properties of the material. The material was further investigated to characterize the inclusions by examining the material through a transmission electron microscope and employing focused ion beam machining to reveal crack propagation through the intermetallic phase. The intermetallic phase was determined to be TiB from the interplanar spacing shown from the SAED imaging Figure 74, the interplanar spacing was found from the image to be an average of 0.37 nm along the (101) plane consistent with the structure of TiB having an spacing of 0.3648 nm [59].

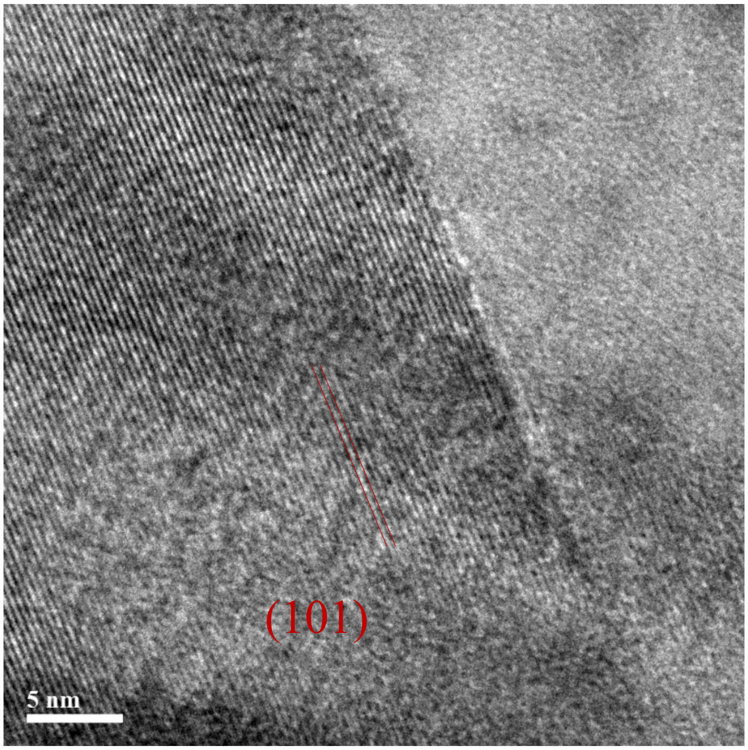

Figure 74 SAED analysis of TiB intermetallic found in Ti-A sample

Figure 75 shows the direction of the fatigue fracture evidenced by the strirations from the cyclical loading of the fatigue sample, the TiB intermettalic displays evidence of transgranular fracture with serrated edges that appears to be a ratcheting fracture motion. The line represents the milling direction to reveal the subsurface structure. Figure 76 exposes the crack that propagates through the intermetallic, the darker region, and then is arrested at the matrix interface. Intermetallic are have been added to aid in crack mitigation and improvement of fatigue properties, it is unclear if the intermetallic in Ti-B were included for this purpose or a by-product of the manufacturing process [58]-[59].

The images show a different fracture mechanic is employed to rupture the Ti-B intermetallic offering some insight into the difference in hardness of the material compared to the matrix. The existence of nanograin structures has been shown to improve the fatigue properties of materials, whether they existed before or during the fatigue process they do have a beneficial influence on the fatigue properties [61]. The larger crack on the left of the image has extended through the top intermetallic and the subsurface intermetallic and then stops at the matrix.

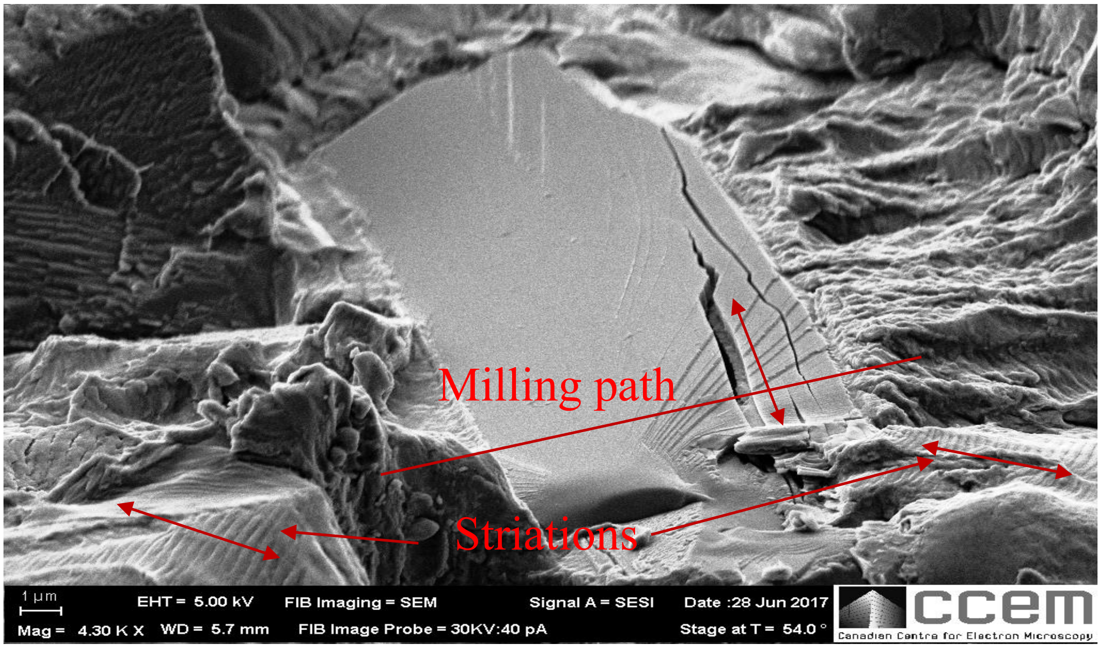

Figure 75 TiB intermetallic fracture with striations visible in the matrix

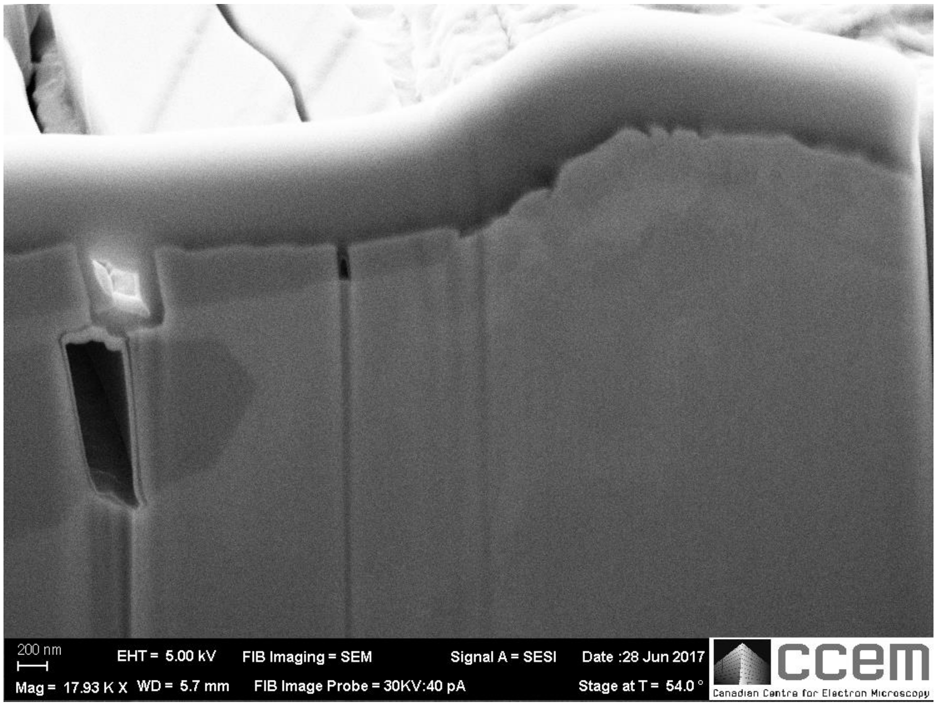

Figure 76 FIB section revealing intermetallic and fatigue crack interface where the crack did not propagate into the matrix

The Ti-B fracture samples were examined to determine if the TiB intermetallic contributed in improving the fatigue properties of the material, Figure 77 shows the difference in fracture mechanisms between the TiB phase (the central region with smooth fracture surface) and the matrix. The matrix shows serrated edges typical of a ductile fracture whereas the secondary phase indicates a intragranular fast fracture of the intermetallic revealing a significant difference in the reaction to the crack path

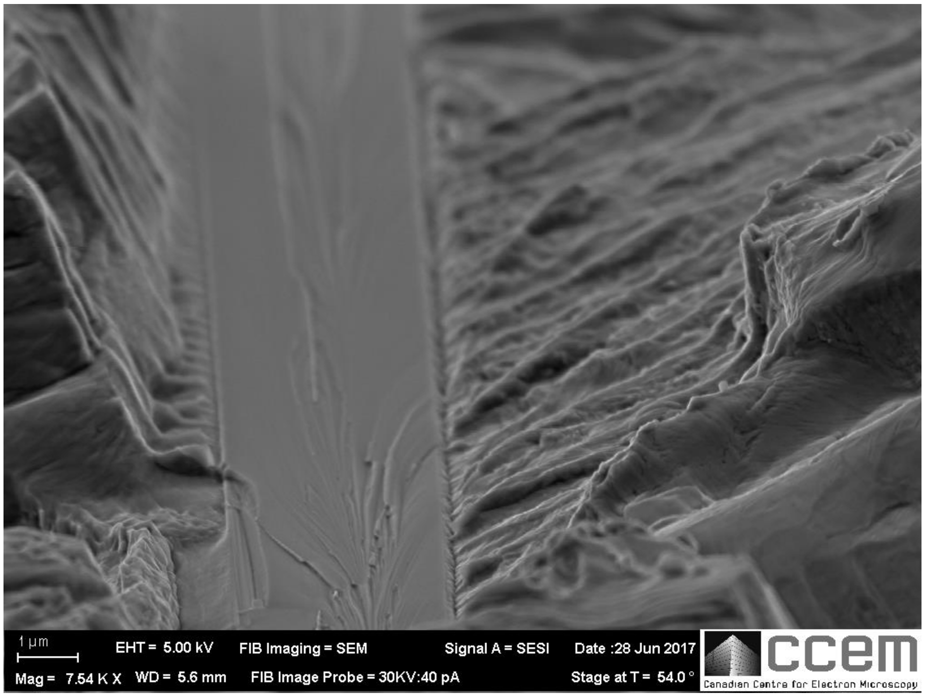

Figure 77 Fracture surface of intermetallic and matrix

The fracture surfaces were further analyzed through high resolution transmission electron microscope as in Figure 78 that reveals areas that have areas that are not fully coherent to the matrix. The areas the area of the matrix that is directly adjacent to the intermetallic reveals a nanograin structure is most likely formed through severe plastic deformation and high strains induced during the fatigue testing, this is shown in more detail in Figure 79. Lewandowska et al. found that large inclusions provided an incoherency in the stress field at the inclusion, resulting in dislocations being ejected from neighboring grains and piling up along the edge of the inclusion forming a nanocrystalline structure. The ability to inhibit the stress flow would indicate a strengthening mechanism attributed to the TiB intermetallic.

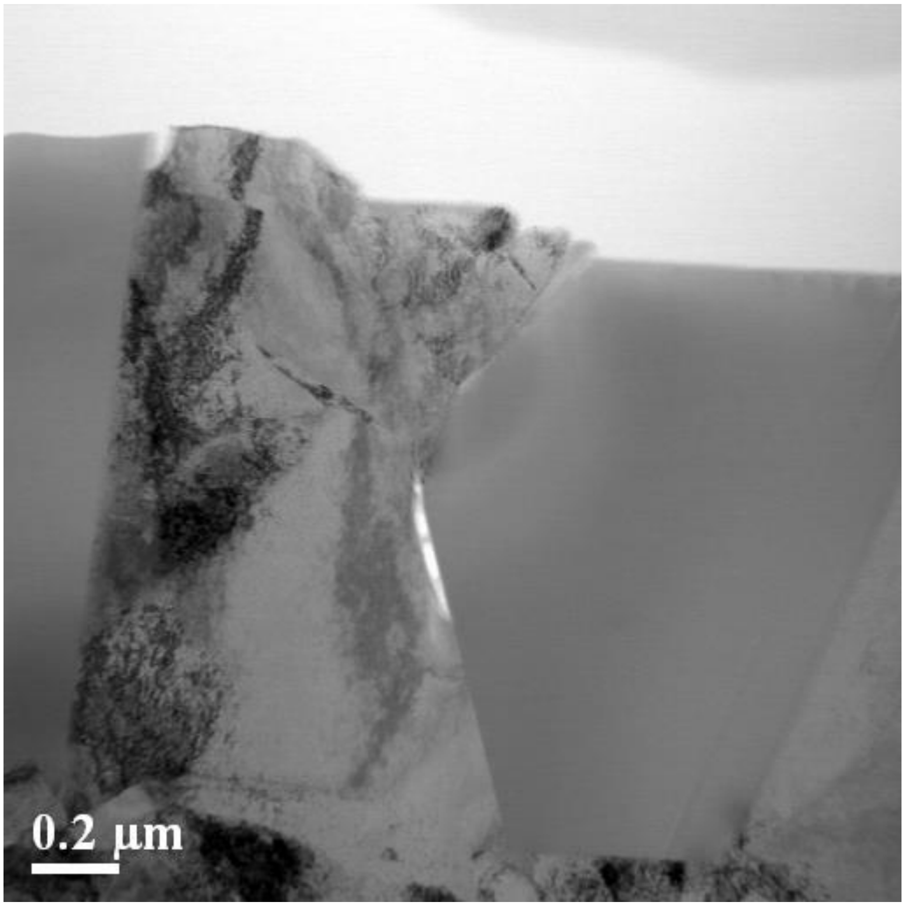

Figure 78 HRTEM image of intermetallic and matrix interface

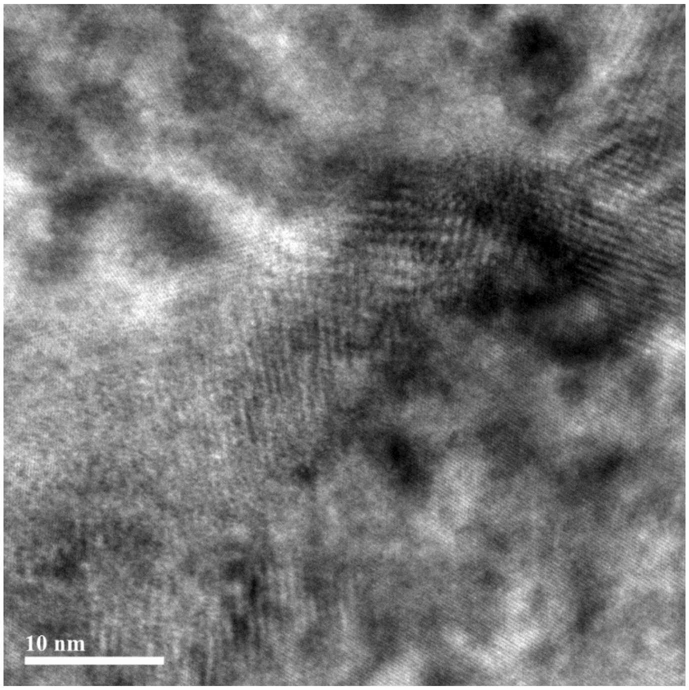

Figure 79 High Resolution image indicating a nanograined structure adjacent to Ti-B inclusion.

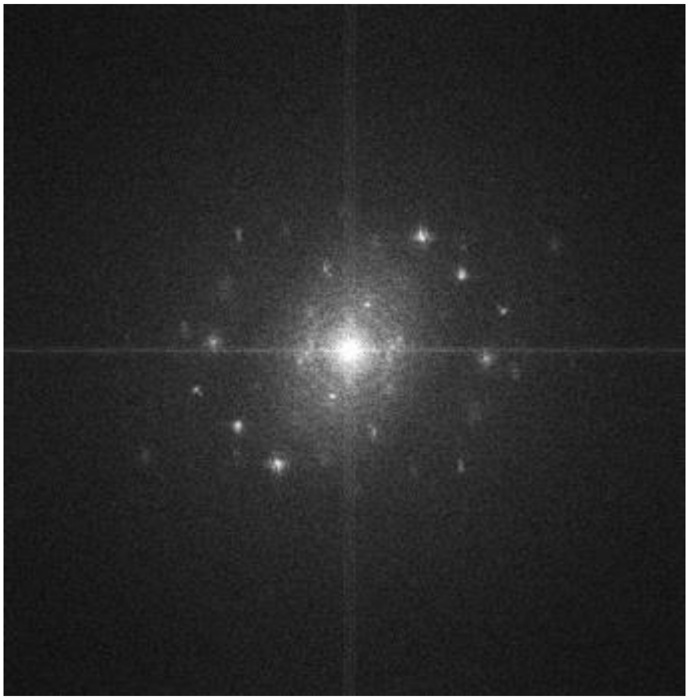

Figure 80 SAED image of nanocrystalline structures in Figure 79

Nanocrystalline grains structures can be formed during high strains that may be prevalent during the manufacturing process, although we only observed these regions next to cracks and intermetallic inclusions [61]-[62]. The TiB phase does not appear to have become dislodged from the fracture event as evident from the line scan in Figure 81 there is no detectable interface at the junction of the matrix and intermetallic. The nanocrystalline features are evident from the SAED imaging of Figure 79 shown in Figure 80, the small rings that appear around the center are indicators for nanocrystalline structures [63]-[64].

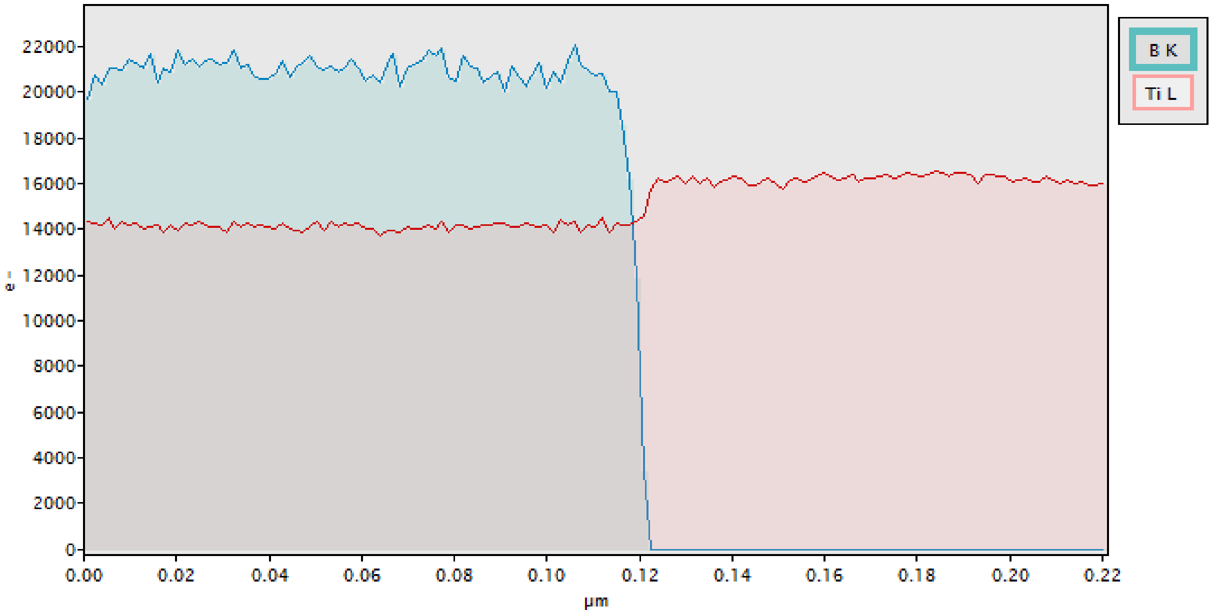

Figure 81 Line scan of the interface between the matrix and TiB intermetallic conducted at interface of intermetallic and matrix showing full cohesion

Chapter 6: Conclusions

The final chapter is a concise restatement of the significant conclusions resulting from this research, as well as recommendations for future work which could further investigate the properties of the research materials.

6.1 Conclusions

- The additive manufactured titanium material exhibits an ultimate tensile strength of 551 MPa and 90% survivability fatigue strength of 255 MPa, that exceed the ultimate tensile strength of 482 MPa and fatigue strength of 141 MPa of the reference material.
- The microstructure of the additive manufacture titanium comprised of low porosity of 0.91% when comparing the density of fully dense pure titanium and TiB intermetallic which contributed to the fatigue and mechanical properties.
- The powder metallurgy aluminum alloys displayed high porosity between 2.3% to 7.7% and low fatigue strength that fall below 60 MPa.
- Porosity within the structure is the primary influence of material properties of the tested materials.
- PM produced materials exhibit a high degree of porosity from the amalgamation of powder particles during the sintering process.
- The utilization of lightweight PM materials produced through cold press and sinter process is not beneficial, the excess material required to meet the stress state nullifies the weight savings. The materials of produced by the cold press and sinter technique had a specific fatigue strength in the range of 20.4 kNm/kg for Al-A to 22.3 kNm/kg for Ti-A with the reference material having a specific fatigue strength of 20.8 kNm/kg.

6.2 Recommendations

To further investigate the influence the TiB intermetallic has on the properties of the Ti-B material a more systematic testing would be needed to identify the properties without the intermetallic phase, compare to see if there is any change in the properties. Investigations into the impact that the additive manufacturing process has on the presence and growth of the intermetallic within the titanium. Defining contribution that the concentration of boron has on the growth rate and size of the intermetallic. Further post-processing of the cold press and sintered materials could improve the fatigue properties by densification of the surface and near-surface pores.

References

[1] R. M. German, *Powder Metallurgy and Particulate Materials Processing*. Princeton, New Jersey: Metal Powder FIndustries Federation, 2005.

[2] G. Dowson and D. Whittaker, “Introduction to Powder Metallurgy, The Process and Its Products,” 2008.

[3] ASTM, “Standard Test Methods for Estimating Average Particle Size of Metal Powders and Related Compounds Using Air Permeability 1,” pp. 1–7, 2015.

[4] H. Wang, Z. Zak Fang, and P. Sun, “A Critical Review of Mechanical Properties of Powder Metallurgy Titanium,” *Int. J. Powder Metall.*, vol. 46, no. 5, pp. 45–57, 2010.

[5] F. F. Lange, “Powder processing science and technology for increased reliability,” *J. Am. Ceram. Soc.*, vol. 72, no. 1, pp. 3–15, 1989.

[6] K. Uematsu, M. Miyashita, j. Kim, and N. Uchida, “Direct Study of the Behaviour of Flaw-Forming Defect in Sintering,” vol. 75, no. 4, pp. 1016–1018, 1992.

[7] D. Manfredi, F. Calignano, M. Krishnan, R. Canali, E. P. Ambrosio, and E. Atzeni, “From powders to dense metal parts: Characterization of a commercial alsimg alloy processed through direct metal laser sintering,” *Materials (Basel).*, vol. 6, no. 3, pp. 856–869, 2013.

[8] E. Klar, *ASM Handbook Volume 7: Powder Metallurgy*. American Society for Metals, 1984.

[9] R. German, *Sintering: From Empirical Observations to Scientific Principles*. 2014.

[10] R. M. German, “Prediction of sintered density for bimodal powder mixtures,” *Metall. Trans. A*, vol. 23, no. 5, pp. 1455–1465, 1992.

[11] MPIF, *Standard Test Methods for Metal Powders and Powder Metallurgy Products*. Princ:

Metal Powder Industries Federation, 2002.

[12] G. N. Grayson, G. B. Schaffer, and J. R. Griffiths, “Fatigue crack propagation in a sintered 2xxx series aluminium alloy,” *Mater. Sci. Eng. A*, vol. 434, no. 1–2, pp. 1–6, 2006.

[13] M. L. Marucci, F. G. Hanejko, F. Bond, and B. Steel, “Effect of Copper Alloy Addition Method,” pp. 1–11, 2010.

[14] M. L. Marucci, M. C. Baran, and K. S. Narasimhan, “Properties of High Density Sinter-Hardening P/M Steels Processed Using Advanced Binder System,” Orlando, Florida, 2002.

[15] T. F. Murphy, B. a. Lindsley, and C. T. Schade, “A metallographic examination into fatigue-crack initiation and growth in ferrous PM materials,” *Int. J. Powder Metall.*, vol. 49, no. 4, pp. 23–34, 2013.

[16] T. F. Murphy, G. B. Fillari, and G. J. Golin, “A Metallographic Investigation Into the Effect of Sintering on an FC-0205 Premix.”

[17] F. H. Froes, “Titanium Powder Metallurgy: A Review - Part 1 - British Library,” *Adv. Mater. Process.*, vol. 170, no. 9, pp. 16–23, 2012.

[18] Y. Liu, L. F. Chen, H. P. Tang, C. T. Liu, B. Liu, and B. Y. Huang, “Design of powder metallurgy titanium alloys and composites,” *Mater. Sci. Eng. A*, vol. 418, no. 1–2, pp. 25–35, 2006.

[19] J. R. Pickens, “Aluminium powder metallurgy technology for high-strength applications,” *J. Mater. Sci.*, vol. 16, no. 6, pp. 1437–1457, 1981.

[20] T. Schubert, “Aluminium PM ’is a Challenge That Industry Can Overcome ’,” no. March, pp. 32–35, 2005.

[21] R. Lumley, *Fundamentals of aluminium metallurgy: Production, processing and applications*. Elsevier, 2010.

[22] R. Haynes, "Fatigue Behaviour of Sintered Metals amd Alloys," vol. 13, no. 26, 1970.

[23] C. Lall, P. Williamson, S. Drive, W. Street, and S. M. Pa, "Wear Resistance and Mechanical Properties of Selected PM Aluminum Alloys and Composites," *Met. Powder Rep.*, vol. 66, no. 2, pp. 4–7, 2015.

[24] R. Lumley, *Fundamentals of Aluminium Metallurgy*, 1st ed. Cambridge: Woodhead Publishing Limited, 2011.

[25] ASTM International, "Standard Specification for Additive Manufacturing Titanium-6 Aluminum-4 Vanadium with Powder Bed Fusion," vol. i, pp. 1–8, 2012.

[26] J. Withers, V. Shapovalov, J. Laughlin, and R. Loutfy, "HIGH RATE LOW COST RAPID ADDITIVE MANUFACTURING," Tucson, Arizona, 2004.

[27] W. E. Frazier, "Metal Additive Manufacturing: A Review," *J. Mater. Eng. Perform.*, vol. 23, no. 6, pp. 1917–1928, 2014.

[28] S. Bland and B. Conner, "Mapping out the additive manufacturing landscape," *Met. Powder Rep.*, vol. 70, no. 3, pp. 115–119, 2015.

[29] S. Bland and N. T. Aboulkhair, "Reducing porosity in additive manufacturing," *Met. Powder Rep.*, vol. 70, no. 2, pp. 79–81, 2015.

[30] J. C. Withers, "Novel Additive Manufacturing Produces Low Cost Large Parts," Tuscon, Arizona, 2004.

[31] M. Meignanamoorthy, S. Sakthivelu, and M. Ravichandran, "A Survey of Aluminium

Metal Matrix Composites Using Powder Metallurgy Technique," *Int. J. Adv. Res. Trends Eng. Technol.*, vol. 2, no. 3, 2015.

[32] ASTM, "ASTM E18 - Standard Test Methods for Rockwell Hardness of Metallic Materials," 2013.

[33] B. Cotterell, S.-Q. He, and Y.-W. Mai, "Fatigue of sintered steel," *Acta Metall. Mater.*, vol. 42, no. 1, pp. 99–104, 1994.

[34] Metal Powder Industries Federation, "MPIF 56," *MPIF Stand. Test Methods*, pp. 108–113, 2012.

[35] H. Mayer, M. Papakyriacou, B. Zettl, and S. E. Stanzl-Tschegg, "Influence of porosity on the fatigue limit of die cast magnesium and aluminium alloys," *Int. J. Fatigue*, vol. 25, no. 3, pp. 245–256, 2003.

[36] H. Drar, "Metallographic and fractographic examination of fatigue loaded PM-steel with and without MnS additive," *Mater. Charact.*, vol. 45, no. 3, pp. 211–220, 2000.

[37] ASME, "E468 -11 Standard Practice for Presentation of Constant Amplitude Fatigue Test Results for Metallic Materials," no. c, pp. 1–6, 2011.

[38] F. Cao, P. Kumar, M. Koopman, C. Lin, Z. Z. Fang, and K. S. R. Chandran, "Understanding competing fatigue mechanisms in powder metallurgy Ti-6Al-4V alloy: Role of crack initiation and duality of fatigue response," *Mater. Sci. Eng. A*, vol. 630, pp. 139–145, 2015.

[39] Metal Powder Industries Federation, *MPIF Standard 35*, 2008th ed. Princeton, New Jersey: Metal Powder Industries Federation, 2007.

[40] ASTM, "E3-11 Standard Guide for Preparation of Metallographic Specimens 1," *ASTM*

Copyright., vol. i, no. Reapproved, pp. 1–12, 2011.

[41] ASTM, “Standard Practice for Microetching Metals and Alloys,” *ASTM Int.*, vol. 7, no. E407, pp. 1–22, 2016.

[42] M. F. Ashby and D. R. H. Jones, *Engineering Materials 2: An Introduction to Microstructures, Processing and Design*. Elsevier Science, 2014.

[43] ASTM International, “Standard Test Methods for Density of Compacted or Sintered Powder Metallurgy (PM) Products Using Archimedes’ Principle,” *Astm B962-15*, pp. 1–7, 2013.

[44] ASM International Handbook Committee, “ASM Handbook Volume 2, Properties and Selection: Nonferrous Alloys and Special Purpose Materials,” in *ASM international*, 1995.

[45] J. A. Slotwinski, E. J. Garboczi, and K. M. Hebenstreit, “Porosity Measurements and Analysis for Metal Additive Manufacturing Process Control,” *J. Res. Natl. Inst. Stand. Technol.*, vol. 119, p. 494, 2014.

[46] ASTM, “Standard Test Methods of Compression Testing of Metallic Materials at Room Temperature,” *Annu. B. ASTM Stand.*, vol. 3.01, no. 1, pp. 92–100, 2012.

[47] ASM International Handbook Committee, “ASM Handbook–Volume 1: Properties and Selection: Irons, Steels, and High Performance Alloys,” in *ASM International, Materials Park*, 1990, pp. 2195–2248.

[48] M. I. McMahon and R. J. Nelmes, “New high-pressure phase of Si,” *Phys. Rev. B*, vol. 47, no. 13, p. 8337, 1993.

[49] K. M. Knowles and W. M. Stobbs, “The structure of {111} age-hardening precipitates in Al{--}Cu{--}Mg{--}Ag alloys,” *Acta Crystallogr. Sect. B*, vol. 44, no. 3, pp. 207–227, Jun.

1988.

[50] J. C. Jamieson, “Crystal Structures of Titanium, Zirconium, and Hafnium at High Pressures,” *Science (80-.).*, vol. 140, no. 3562, pp. 72–73, Apr. 1963.

[51] H. Gruber and E. Krautz, “Magnetoresistance and Conductivity in the Binary System Titanium–Oxygen. I. Titanium Oxides with Metallic Conductivity,” *Phys. status solidi*, vol. 69, no. 1, pp. 287–295, 1982.

[52] E. Zhang, Y. Jin, H. Wang, and S. Zeng, “Microstructure and hardness of as-cast in situ TiB short fibre reinforced Ti-6Al matrix composites,” *J. Mater. Sci.*, vol. 37, no. 9, pp. 1861–1867, 2002.

[53] H. Drar, “Fractographic Aspects of Fatigue of Sintered Ni-Steels,” *Mater. Charact.*, vol. 34, no. 2, pp. 129–141, 1995.

[54] I. C. MAYES and T. J. BAKER, “Understanding of Fatigue Thresholds Through the Influence of Non-Metallic Inclusions in Steel,” *Fatigue Fract. Eng. Mater. Struct.*, vol. 4, no. 1, pp. 79–95, 1981.

[55] K. Farokhzadeh and a Edrisy, “Materials Science & Engineering A Fatigue improvement in low temperature plasma nitrided Ti – 6Al – 4V alloy,” *Mater. Sci. Eng. A*, vol. 620, pp. 435–444, 2015.

[56] T. M. Cimino, H. G. Rutz, A. H. Graham, T. F. Murphy, H. Corporation, and J. July, “The Effect of Microstructure on Fatigue Properties of Ferrous P / M Materials,” in *Internationa*, 1997, pp. 1–11.

[57] H. Rutz, T. Murphy, and T. Cimino, “The effect of microstructure on fatigue properties of

high density ferrous P/M materials," *Adv. Powder Metall. Part. Mater.*, vol. 4, p. 13, 1996.

[58] J. Meija *et al.*, "Atomic weights of the elements 2013 (IUPAC Technical Report)," *Pure Appl. Chem.*, vol. 88, no. 3, pp. 265–291, 2016.

[59] B. F. Decker and J. S. Kasper, "The crystal structure of TiB," *Acta Crystallogr.*, vol. 7, no. 1, pp. 77–80, 1954.

[60] F. Cao, K. S. Ravi Chandran, P. Kumar, P. Sun, Z. Zak Fang, and M. Koopman, "New Powder Metallurgical Approach to Achieve High Fatigue Strength in Ti-6Al-4V Alloy," *Metall. Mater. Trans. A Phys. Metall. Mater. Sci.*, vol. 47, no. 5, pp. 1–11, 2016.

[61] Y. Estrin and A. Vinogradov, "Extreme grain refinement by severe plastic deformation: A wealth of challenging science," *Acta Mater.*, vol. 61, no. 3, pp. 782–817, 2013.

[62] A. Azushima *et al.*, "Severe plastic deformation (SPD) processes for metals," *CIRP Ann. - Manuf. Technol.*, vol. 57, no. 2, pp. 716–735, 2008.

[63] C. C. F. Kwan and Z. Wang, "The Cyclic Deformation Behavior of Severe Plastic Deformation (SPD) Metals and the Influential Factors," *Metals (Basel).*, vol. 2, no. 1, pp. 41–55, 2012.

[64] M. Lewandowska and K. J. Kurzydlowski, "Recent development in grain refinement by hydrostatic extrusion," *J. Mater. Sci.*, vol. 43, no. 23–24, pp. 7299–7306, 2008.

[65] Y. Y. Deryugin, V. E. Panin, S. Schmauder, and E. Soppa, "The effects of macrolocalization of deformation in Al-based composites with Al2O3 inclusions," *Fatigue Fract. Eng. Mater. Struct.*, vol. 26, no. 4, pp. 295–304, 2003.

Vita Auctoris

NAME: Douglas B. Boudreau

PLACE OF BIRTH: Windsor, Ontario

YEAR OF BIRTH: 1978

EDUCATION: Harrow District High School, Harrow, Ontario
1993-1997

University of Windsor, Windsor, Ontario
2011-2015 B.A.Sc.

University of Windsor, Windsor, Ontario
2015-2017 M.A.Sc.